

THE COHERENT OPTICAL SPECTROSCOPY AND CONTROL OF AN ELECTRON SPIN IN A SELF-ASSEMBLED QUANTUM DOT FOR QUANTUM COMPUTING

by

Erik D. Kim

A dissertation submitted in partial fulfillment
of the requirements for the degree of
Doctor of Philosophy
(Applied Physics)
in The University of Michigan
2009

Doctoral Committee:

Professor Duncan G. Steel, Chair
Professor Paul R. Berman
Professor Roberto D. Merlin
Professor Theodore B. Norris
Professor Georg A. Raithel

© Erik D. Kim 2009
All Rights Reserved

우리 할아버님 그리고 부모님께

To my grandfather and my parents

ACKNOWLEDGEMENTS

A few years ago I didn't think this thesis would be written. Having gone through a nearly year and a half span of failed experiments, I was beginning to consider other possible career options. I believe that God, by both ordinary and extraordinary means, provided the inspiration and the guidance I needed to stay the course, bringing me to eventual (and undeserved) success in the laboratory. Such inspiration and guidance has come through family members, colleagues and friends, as well as through moments such as those of Saturday, March 31, 2007 when, at around 3am, I was strangely motivated to repeat a failed set of scans despite being almost out of liquid helium, discouraged by what seemed to be another day of failure, and exhausted from having woken up early for the previous day's 8 am group meeting. That moment would turn out to produce the first significant step of progress in lab, and, thankfully, it wouldn't be the last.

The first people I want to thank are my parents, who have made countless sacrifices and tough decisions throughout the years for the sake of my sisters and me. Their willingness to give of themselves out of love for their children will never cease to amaze me or to spur me on to emulate them. They are why I am where I am. I would also like to thank my sisters, Erica and Erin, as well as my uncles, aunts and grandfather back in Korea for their generous love and support over the years.

From the lab, I must first of course thank my advisor Professor Duncan Steel, who always expressed his confidence that I would succeed in lab no matter how discouraged I was. He mentors as both an erudite scholar and a concerned friend, sincerely advising what is in the best interest of his students both professionally and personally. His

style of leadership not only shaped my individual development as a scientist, but also fostered an invigorating lab environment that was exciting to be a part of. I also must thank my lab mentor, Yanwen Wu (a.k.a. “Bossy”), who let me tinker with her experimental setup despite the fact that I was still “green” in the ways of the lab back in 2005. She was a fun friend and a kindred spirit in the appreciation of delicious food who could amazingly eat almost as much as I can despite being only about half my size. I am also grateful to Jun Cheng for his patience with my many questions when I first joined as well as his willingness to finish machining the baseplate I was supposed to make for the magnetocryostat mount my first summer in lab. Xiaodong Xu (a.k.a. “xiong di”) was an excellent lab champion, friend and brother-in-arms in facing the challenges of single dot studies. Our conversations about physics, sports and “peach blossoms” were good times. Qiong Huang was also a very helpful with his knowledge of electronic devices and his willingness to help with whatever was needed in lab. Katherine Smirl was a great help to me in lab, especially on those overnight runs when she would come in early in the morning to take over experiments so I could go home and sleep. Bo Sun was very instrumental in helping me understand the 899 laser systems in lab and was also a very sharp source of info for frequency domain experiments. I would also like to thank Alberto Amo, who was a visiting student in our lab from late 2006 to early 2007, for his efforts to help us with time-domain studies of single InAs dots. Unfortunately, he had to return to Spain before he could see the fruits of his labors.

At the Naval Research Lab, I would like to thank Dan Gammon, Allan Bracker and Sophia Economou. Dan was like another advisor to me with whom I greatly enjoyed discussing physics. I am also highly grateful for his invitation to visit NRL in early 2009, which was a very enjoyable time. Allan greatly helped my understanding of sample related physics and the growth process. His willingness to discuss sample issues over the phone was much appreciated. I was able to have a number of highly constructive discussions with Sophia, which particularly helped in solidifying my understanding of geometric phases. I would also like to express my appreciation for Lu Sham at the University of California at San Diego. He was also like another advisor

from whom I learned a great deal about quantum dot physics over the years.

I would also like to express my sincere gratitude to my committee members, Professor Paul Berman, Professor Roberto Merlin, Professor Ted Norris and Professor Georg Raithel. Each has significantly contributed to my development during my graduate studies. Professor Berman, who agreed to my last-minute request to join my committee, was very helpful in discussions of quantum optics, and I rely heavily on his lecture notes. Discussions with Professor Merlin over the years were very helpful in sharpening my critical analysis of physics concepts. Professor Norris' courses on classical and ultrafast optics were very useful in the laboratory, particularly with understanding mode-locked laser systems and pulse measurement techniques. Professor Raithel taught the two-semester electrodynamics course my first year of grad school and was always very willing to discuss physics, even outside of his office hours, which was a great help to us pesky first years.

TABLE OF CONTENTS

DEDICATION		ii
ACKNOWLEDGEMENTS		iii
LIST OF TABLES		ix
LIST OF FIGURES		x
LIST OF APPENDICES		xvi
CHAPTER		
1.	Quantum Computing: History, Requirements and Candidate Implementations	1
1.1	A Brief History of Quantum Computing	2
1.2	The Requirements for Quantum Computing	3
1.3	Candidate Physical Systems for Quantum Computing	5
1.3.1	Trapped Ions	5
1.3.2	Nuclear Spins in Molecules	6
1.3.3	Electron and Nuclear Spins in Diamond	7
1.3.4	Phosphorous Donors in Si (Kane Quantum Computer)	8
1.3.5	Superconducting Circuits	9
1.3.6	Quantum Dots	10
1.4	Thesis Outline	12
1.5	Chapter Summary	14
2.	Self-Assembled InAs Quantum Dots: Characteristics and Sample Structure	15
2.1	Sample Structure and Growth Process	15
2.2	QD Charging and Carrier Properties	18
2.3	Energy Level Structure of a Negatively Charged QD	19
2.3.1	Selection Rules for $\mathbf{B}_{ext} = 0$	21
2.3.2	Selection Rules for $\mathbf{B}_{ext} = B\hat{x}$	22
2.4	Chapter Summary	23

3.	Control and Read-Out of a Single InAs QD with Picosecond Optical Pulses: Theory	25
3.1	Pulse-Driven Two-Level System	26
3.2	The Maxwell-Bloch Equations	29
3.3	Phase-Sensitive Detection of QD States	32
3.4	Pump-Probe Studies: $\mathbf{B}_{\text{ext}} = 0$	33
3.5	Pump-Probe Studies: $\mathbf{B}_{\text{ext}} = B\hat{x}$	36
3.6	Chapter Summary	38
4.	Control and Read-Out of a Single InAs QD with Picosecond Optical Pulses: Experimental Setup and Results	40
4.1	Experimental Setup	42
4.1.1	Optical Sources	42
4.1.2	Cryostat	43
4.1.3	PL Spectroscopy Setup	43
4.1.4	Phase Sensitive Detection Setup	44
4.2	QD Characterization with PL Spectroscopy	45
4.3	CW Stark-Shift Modulation Absorption Spectroscopy	46
4.4	Pulsed Stark-Shift Modulation Absorption Spectroscopy	52
4.5	Pump-Probe Studies with $\mathbf{B}_{\text{ext}} = 0$: Trion Decay and Trion Rabi Oscillations	55
4.6	Pump-Probe Studies with $\mathbf{B}_{\text{ext}} = B\hat{x}$: Electron and Heavy-Hole Spin Quantum Beats	58
4.7	Chapter Summary	59
5.	Theoretical Spin Qubit Gates for an Electron Confined in an InAs QD	61
5.1	The Interaction of a Highly-Detuned Optical Pulse with a QD Confined Electron Spin	62
5.1.1	Equations of Motion for the Electron Spin Probability Amplitudes	62
5.1.2	Effective Hamiltonian and Bloch Sphere Representation	65
5.1.3	Unitary Transformation Matrix for a Circularly Polarized Pulse	67
5.2	The Operation of the External Magnetic Field	69
5.3	Geometric Phases Imparted by a CW Field	70
5.4	Hadamard Gate Construction	73
5.5	Chapter Summary	74
6.	Experimental Demonstrations of Spin Qubit Rotations About Two Orthogonal Axes	75
6.1	Spin Initialization by Optical Pumping with a CW Field	76

6.2	Read-Out of Electron Spin Manipulations Via the CW Field . . .	80
6.3	One-Pulse Studies: Polarization and Detuning Dependence	82
6.4	Two-Pulse Studies: Spin Precession about the Magnetic Field . .	85
6.5	Two-Pulse Studies: Geometric Phases and Spin Precession Modu- lation	87
6.6	Chapter Summary	91
7.	Proposed Future Experiments	92
7.1	Density Matrix Tomography (DMT) of a QD Confined Electron Spin	93
7.1.1	DMT Procedure: Theory	93
7.1.2	Experimental Calibration	97
7.1.3	DMT Procedure for the Hadamard Gate	98
7.2	Pulse-Generated Geometric Phases for Spin Rotation	100
7.2.1	Derivation of the Unitary Transformation Matrix	100
7.2.2	Experimental Procedure	103
7.3	Chapter Summary	105
8.	Thesis Summary	107
	APPENDICES	112
	BIBLIOGRAPHY	122

LIST OF TABLES

Table

2.1	Energy level labels and expressions in terms of spin and angular quantum numbers for $\mathbf{B}_{\text{ext}} = 0$. The notation $ \overline{\square}\rangle$ indicates a \hat{z} basis state and is used to distinguish from \hat{x} basis states.	22
2.2	Energy level labels and expressions in terms of \hat{z} basis states for $\mathbf{B}_{\text{ext}} = B\hat{x}$. The notation $ \square\rangle$ (no overline) indicates an \hat{x} basis state.	23
5.1	Different combinations of the three unitary transformations resulting in a Hadamard gate and the global phases for each.	73
B.1	\hat{x} basis density matrix elements in terms of \hat{z} basis density matrix elements.	117

LIST OF FIGURES

Figure

1.1	Energy density of states for structures of different dimensionality (reproduced with permission from Y. Wu).	10
2.1	(a) Basic depiction of the QD growth process including the indium flush technique for InAs grown on GaAs (from bottom to top). (b) R060913G sample structure diagram showing the configuration of layers and the contacts used for voltage control. (c) Al shadow mask aperture pattern. The smaller apertures are on the order of $1\ \mu\text{m}$ in diameter while the larger braille features and slots have dimensions on the order of $10\ \mu\text{m}$. Due to the sample mount, only those apertures lying within the blue circle allow for studies in a transmission geometry. (d) Illustration of the charging effect. The sample voltage determines the energy level difference between QD levels and the Fermi energy of the electron reservoir in the n-doped GaAs layer, allowing for different possible charge states in the dot.	16
2.2	Conduction and valence band configurations before and after optical excitation for an initially neutral dot and a dot initially containing a single electron in the conduction band. We consider specifically the lowest-lying excitations. In the case of the negatively charged dot, the electron pair in the conduction band forms a singlet state.	19
2.3	(a) QD excitation scheme and axis orientation. Optical excitation is along the growth axis \hat{z} . (b) The four levels formed by the electron spin ground states and the two heavy-hole spin states of the trion, quantized along some axis that depends on system parameters. The dashed green lines indicate the transitions of interest. \uparrow (\downarrow) indicates the projection of the total angular momentum m_j of the electron, corresponding to a value of $1/2$ ($-1/2$) while $\uparrow\uparrow$ ($\downarrow\downarrow$) corresponds to a heavy-hole m_j value of $3/2$ ($-3/2$)	21
2.4	Diagrams illustrating the arrangement of levels and transition selection rules for (a) $\mathbf{B}_{\text{ext}} = 0$ and (b) $\mathbf{B}_{\text{ext}} = B\hat{x}$. The dashed red arrows indicate optically forbidden transitions. Δ_e (Δ_h) are the electron and heavy-hole Zeeman splittings. The state labels used for mathematical expressions in this thesis are given by the light blue text.	24

3.1	Two-level system representing one of the optical transitions in a QD. ω_0 is the angular frequency corresponding to the energy difference between the states, Γ is the excited state decay rate, Ω is the laser frequency, which is set equal to ω_0 , and $\hat{\sigma}_+$ indicates the optical polarization that drives the transition.	27
3.2	Relaxation rates between the QD levels (a) with and (b) without an externally applied magnetic field along \hat{x} . For each case, the trion relaxation rates are assumed to be equal for each decay path and the mutual relaxation rates between the spins are taken to be the same.	36
3.3	Spin Bloch spheres in real space showing the time-evolution of the electron and heavy-hole spin vectors for a resonant $\hat{\sigma}_-$ polarized pulse incident at time $t = 0$. Prior to excitation ($t < 0$), the electron and heavy-hole spins are unpolarized. At $t = 0$ the $\hat{\sigma}_-$ polarized pulse generates $ T_z+\rangle$ population, creating electron and heavy-hole spin vectors that are oppositely aligned along \hat{z} . These spin vectors precess about the \hat{x} axis at rates determined by the Zeeman splittings for the two spins.	37
4.1	The experimental setup used in all studies, where components surrounded in dashed boxes are on removable mounts. Optical pulses and CW fields are provided by the Coherent MIRA 900 and the Coherent 899-29, respectively, both pumped by separate Coherent Verdi-V10 solid state lasers (not pictured). A Janis Research Company superconducting magneto cryostat keeps the sample at liquid helium temperatures and is used to provide DC magnetic fields ranging from 0 to 6.6 T in strength. The sample is imaged using a CCD camera on the collection side of the sample. For PL spectroscopy studies, a Horiba Jobin-Yvon HR640 spectrometer is used along with a Princeton Instruments liquid nitrogen cooled CCD. For pulsed and CW absorption studies, measurements are taken using a Hamamatsu S8890-15 Si avalanche photodiode module. The photocurrent output is converted to a voltage with a 10 k Ω resistor and is then read by an EG&G 7265 lock-in amplifier. Both the reference signal and the sample bias signal are provided by a Stanford Research Systems DS345 signal generator.	41
4.2	Intensity autocorrelation trace (left) and optical spectrum (right) of the MIRA 900 pulses produced in picosecond mode for a particular exit slit width. Autocorrelation traces are taken with an Inrad model 5-14A autocorrelator that measures the intensity autocorrelation signal. The pulse spectrum was measured using the HR640 with the liquid nitrogen cooled CCD camera and fit to a squared hyperbolic secant function (red curve).	43
4.3	APD circuit diagram.	44

4.4	PL spectra as a function of emission wavelength for sample R060913G at different sample bias voltages. The PL spectra show emission from different sample layers for CW excitation at 780 nm through the aperture indicated in the upper-left inset. The general range of QD emission wavelengths is also indicated, though QD emission lines are too weak to be observed on these scales.	45
4.5	Emission spectra of aperture Dp2(9) [circled in the inset of (a)] as a function of applied sample bias and emission energy for two different energy/bias ranges. (a) Emission spectrum showing charge transitions for QD #1 and QD #2 in the -0.6 V to -0.4 V range. The lines surrounded by the yellow boxes indicate the states of QD #1, the primary dot studied in this thesis. The emission of QD #1 switches from containing no charges (X^0) to containing a single electron (X^{1-}) when the sample bias is increased above -0.55 V. The slight positive sloping of the emission lines is a result of the DC Stark shift, which blue-shifts each emission line as the bias voltage is increased. (b) The extended spectrum of the trion emission lines for QD #1 and QD #2, showing that trion emission covers a long voltage range with the peaks broadening considerably as the sample voltage is increased.	47
4.6	The CW Stark-shift modulation absorption spectroscopy method. (a) Sample bias voltage $V(t)$ as a function of time for small (green curve) and large (red curve) values of V_{AC} . (b) Theoretical absorption profile of an optical transition in a single QD (black curve), where \mathcal{A} is plotted as a function of V_{DC} without voltage modulation. The vertical dotted lines indicate points on the absorption profile corresponding to the sample bias voltage values. The dashed vertical lines indicate the value of V_{DC} for each particular voltage configuration. (c) The absorption \mathcal{A} as a function of time for the small (orange) and large (light blue) modulations. The modulation of the absorption signal is a result of the modulated sample bias and occurs at the same frequency. (d) The lock-in reference signal as a function of time. The reference signal oscillates at the same frequency as $V(t)$ as the lock-in external reference is provided by the signal generator driving the sample bias. The phase difference between the lock-in and the signal generator, $\phi_{ref} = 2\pi \frac{\Delta t_{ref}}{T_{ref}}$, can be controlled and determines the X and Y channel signals of the lock-in. (e) Simulated X channel signals as a function of V_{DC} for the two different values of V_{AC} at $\phi_{ref} = 0$. The smaller value of V_{AC} (orange curve) leads to a signal that resembles the derivative of the absorption lineshape while the larger value (light blue curve) leads to a positive and negative peak separated by the value of V_{AC} , each reflecting the absorption lineshape of the transition.	50

4.7	Absorption spectrum of the trion of QD #1, where the lock-in phase ϕ_{ref} is set such that the modulated absorption signal is entirely in the X channel. Each absorption trace is obtained by scanning the energy of the Coherent 899-29 through the trion transition energy at different values of V_{DC} (light blue voltage values) for a V_{AC} value of 0.02 V. The upper-left inset shows the spectrum obtained at $V_{\text{DC}} = 0.14$ V. The lower-right inset plots the zero-crossing energy (green circle in the upper-left inset) as a function of V_{DC} , exhibiting the linearity of the Stark shift.	51
4.8	Arrangement of the QD energies (E_{QD}), pulse spectrum and trion absorption range in pulsed optical measurements of the trion state in a singly charged InAs QD.	53
4.9	Time averaged V_{sig} measurements (X channel) as a function of V_{R} for the trion of QD #1 using a single pulse train of 500 μW average power with $V_{\text{L}} = -1$ V. The dip is the result of the detection of the field radiated by the QD and is shaded to indicate the difference between the background signal level (black dashed line) and the QD signal. . .	54
4.10	V_{R} scans of the trion in QD #1 at different average pulse powers for $V_{\text{L}} = -1$ V. The difference between the background signal level and the QD signal level (shaded gray areas) undergoes a complete oscillation as the average pulse power is increased, indicating a complete Rabi oscillation between the electron and trion states in the dot. The dependence of the background signal level on the average pulse power is also shown.	55
4.11	Time-averaged V_{sig} measurements as a function of pulse delay t_d showing the generation and exponential decay of pump-generated trion population, as indicated by the energy level diagrams given above the graph. A fit of the data to Equation 4.4 is given by the red curve, which yields a trion relaxation time of 855 ± 74 ps.	56
4.12	(a) Experimentally measured V_{sig} values as a function of pump pulse area E_{pu} showing two complete pump-driven Rabi oscillations between the electron and trion states in QD #1. An oscillatory fit of the data (red curve) yields a trion dipole moment of ~ 8 Debye. (b) Theoretical plot of the modulated APD photocurrent as a function of pump pulse area taking into account the trion state of QD #2, which is assumed to have a dipole moment approximately twice that of QD #1.	58
4.13	V_{sig} measurements as a function of t_d for circularly cross-polarized excitation at $B = 3.3$ T and $B = 6.6$ T. The red curves are fits obtained with Equation 4.5 taken in the limit of infinitely long electron and heavy-hole spin coherence times.	59
5.1	Energy level diagram showing the state labels and parameter definitions for the pulsed and CW optical fields. Λ_1 and Λ_2 indicate the two two-photon quantum mechanical pathways between the electron spin states.	63

5.2	Bloch sphere representations (real space) and the unitary transformation matrices associated with the three different means of electron spin control considered in this Chapter. The Bloch spheres demonstrate the operation of each spin control mechanism on some initial spin vector (green), resulting in a rotated spin vector (orange).	72
6.1	Illustration of the optical pumping process for a CW field tuned to the $ 1\rangle$ to $ 4\rangle$ transition. The electron spin is assumed to be in a mixed state prior to the operation of the CW field and the trion relaxation rate Γ_t is assumed to be much greater than the electron spin relaxation rate Γ_e	76
6.2	Theoretical plots of the time averaged absorption $\langle \mathcal{A} \rangle$ as a function of laser frequency for $\Gamma_e \gtrsim \Gamma_t$ (black curve) and $\Gamma_e \ll \Gamma_t$ (red curve). Optical pumping, by depleting the $ 1\rangle$ state population, leads to a diminished absorption signal.	77
6.3	Characterization of the trion absorption range of QD #1 showing the optical pumping and non-optical pumping regions at an external magnetic field of 0.66 T.	78
6.4	Electron and heavy-hole Zeeman splittings as a function of magnetic field. The Zeeman splittings are obtained by measuring absorption peak separations in the low-energy non-optical pumping region, yielding electron and heavy-hole g-factor values of 0.42 and 0.24, respectively.	79
6.5	Calculated ρ_{11} values as a function of time for CW excitation of the $ 1\rangle$ to $ 4\rangle$ transition (a) without and (b) with an incident train of optical pulses for a nonzero magnetic field. (c) Calculated $\bar{\rho}_{11}$ values as a function of time for CW excitation of the $ \bar{1}\rangle$ to $ \bar{4}\rangle$ transition in the \hat{z} basis without an external field. The time averaged populations for all cases are indicated by the red curves.	80
6.6	Illustrations of how $ 1\rangle$ population is generated post initialization by (a) a 45° polarized pulse that drives π rotations for both trion transitions and (b) a $\hat{\sigma}_+$ polarized pulse that drives a π rotation between the electron spin states.	82
6.7	Theoretically calculated and experimentally measured modulated absorption signals as a function of pulse amplitude and V_{DC} . The results for both theory and experiment show trion Rabi oscillations for 45° polarized excitation on resonance (upper left panels), no absorption signal for a detuned 45° polarized pulse (upper right panels), trion and electron spin Rabi oscillations for $\hat{\sigma}_+$ polarized excitation on resonance (lower left panels) and approximately one complete spin Rabi oscillation for a detuned $\hat{\sigma}_+$ polarized pulse.	84
6.8	Calculations of the time evolution of the $ 1\rangle$ population in two-pulse studies during each 13.2 ns period at different values of the pulse delay. Results show that for pulse delays as high as a few ns, the value of ρ_{11} returns to zero before the following pump pulse, signifying complete re-initialization of the electron spin between pulses.	85

6.9	Theoretical and experimentally measured modulated absorption signals as a function of pulse delay and magnetic field. The oscillatory behavior of the signal is clearly exhibited, with the oscillation frequency increasing as the magnetic field is increased in strength.	86
6.10	Modulated absorption scan and oscillatory fit (red curve) as a function of pulse delay for an external magnetic field of 5.5 T. The orientation of the electron spin vector immediately before the probe pulse is indicated at selected delay values.	87
6.11	Diagrams illustrating the time evolution of (a) level occupations in the \hat{x} basis, (b) the electron spin vector and (c) the heavy-hole spin vector between the pump pulse and the first CW-driven π rotation of the $ 1\rangle$ to $ 4\rangle$ transition.	89
6.12	(a) Theoretically calculated values of ρ_{11} immediately after the probe pulse for different CW powers and (b) the corresponding modulated absorption scans at those powers. The green dashed lines serve as guides to the eye in comparing the precession signals at different CW powers. The red circles indicate conditions where the CW-driven trion Rabi period is approximately equal to an integer number of electron spin precession periods, enabling the construction of purely optical spin gates.	90
7.1	$ 1\rangle$ population immediately after the operation of a $\theta = \pi/2$ pulse at times corresponding to a $\pi/2$ and a π precession of the electron spin.	96
7.2	Example modulated absorption scans in experiments with one and two two-photon π pulses, with maximum signals α and β , respectively.	98
7.3	Energy level diagram showing the tuning of the \hat{x} polarized pulse used to generate the geometric phases for spin control.	100
7.4	(a) Example modulated absorption scan (large modulation) as a function of CW field frequency showing the frequency corresponding to ω_0 . (b) Re-plot of one of the panels of Figure 6.7 corresponding to the theoretical optical tripwire signal in studies with a resonant linearly polarized pulse. Values of E_p corresponding to the $n = 1$ (red dashed line) and $n = 2$ (brown dashed line) conditions are indicated.	103
7.5	Theoretically calculated population in $ 1\rangle$ immediately after the second $\pi/2$ pulse in two-pulse studies with a CW field that is turned off between initialization and read-out. Scans are shown both (top) without and (bottom) with a 1 mW \hat{x} polarized rotation pulse about 15 ps in width applied at 75 ps. The rotation pulse results in a $\sim \pi$ rotation of the spin about the \hat{x} axis.	105
A.1	Transitions for which the matrix elements of \mathbf{r}/r are calculated, indicated by the dashed green arrows, for the two magnetic field cases.	114
C.1	Relationship between Bloch sphere coordinates in $\{u, v, w\}$ space and $\{x, y, z\}$ space.	120

LIST OF APPENDICES

Appendix

A.	Calculation of the Selection Rules for a Singly Charged QD . . .	113
B.	Transformation Relations Between the \hat{z} and \hat{x} Density Matrix Elements: Derivation	116
C.	Relationship Between the Electron Spin Bloch Sphere Coordinates in $\{u, v, w\}$ Space and $\{x, y, z\}$ Space	118

CHAPTER 1

Quantum Computing: History, Requirements and Candidate Implementations

Quantum computing, simply put, is a form of computing in which the execution of computational operations relies on quantum mechanical phenomena, namely, quantum superposition and entanglement [1–3]. Over the better part of the last three decades, quantum computing has become both an intensely pursued interdisciplinary field of research and a topic of fascination in popular culture. The primary reasons for this interest and fascination are the theoretical demonstrations of the superior performance of a quantum computer over the standard classical computer for a variety of tasks [2, 4–6] such as the determination of the prime factors of a large number [7–9], the searching of an unsorted database [10, 11], the simulation of quantum mechanical systems [1, 12, 13], the estimation of partition functions in thermodynamical systems [14–16] and the solving of linear systems of equations [17].

As a result of these theoretical discoveries, there has been a considerable amount of experimental effort aimed at verifying these theoretical results and developing a scalable physical system for practical quantum computing. Because experimental endeavors are still in their infancy, current research efforts are spread across several different candidate physical systems with a clear-cut “winner” yet to emerge. Semiconductor quantum dots (QDs) containing a single charge are considered as one of the leading candidate systems for quantum computing [18, 19] and are the subject of this thesis. More specifically, the work presented here focuses on the optical spectroscopy and control of the spin states of an electron confined in a single self-assembled InAs

QD for the execution of gate operations that are foundational for quantum computation.

In this Chapter, we first discuss the history behind the field of quantum computing and the reasons for its impact on the fields of computing and cryptography. The basic requirements for a working quantum computer, commonly referred to as the DiVincenzo criteria [20], are then discussed, followed by a rudimentary survey of some of the physical systems that have been proposed for the implementation of a quantum computer. Finally, an outline of the thesis is given that summarizes the topics covered in each Chapter.

1.1 A Brief History of Quantum Computing

The concept of a quantum computer is generally considered to have first been introduced in a lecture given by Richard P. Feynman [1] at the First Conference on the Physics of Computation held at the Massachusetts Institute of Technology in 1981 [21, 22]. In this lecture, Feynman emphasized the inability of a computing machine operating purely on classical principles to efficiently simulate quantum systems, as the number of classical computing resources required increases exponentially with the number of degrees of freedom in the system. In musing on a possible alternative, he then posited as to whether “quantum computers,” i.e. computers whose elements are inherently quantum mechanical in nature, would be able to simulate any given quantum mechanical system accurately. Oddly, this highly insightful conjecture did little to ignite the field of quantum computing at the time, with Feynman himself leaving the question of quantum simulation open and choosing instead to focus following work on the theoretical operation of a quantum computer in the context of thermodynamic reversibility and free energy dissipation [23, 24]. The proof of Feynman’s conjecture would take nearly 15 years to arrive, provided by Seth Lloyd in 1996 [13].

Prior to the arrival of Lloyd’s proof, however, David Deutsch gave the field of quantum computing a critical boost in 1985 [2] by showing that the “quantum par-

allelism” provided by a quantum computer would enable the performance of certain tasks more quickly than with a classical computer. This demonstration was followed by a proof of the existence of a universal quantum gate by Deutsch in 1989 [4] and the discovery by Deutsch and Jozsa in 1992 [5] of an entire class of computational problems that are more efficiently solved by a quantum computer. Progress in finding quantum algorithms that provided superior performance over their classical counterparts began to gain momentum following these achievements and led to a number of key discoveries including Peter Shor’s factoring and discrete logarithm algorithms in 1994 [7] and Lov Grover’s database search algorithm in 1996 [10].

Of all these discoveries, however, it was Shor’s fast factoring and discrete logarithm algorithms that brought quantum computing into the limelight due to the repercussions of these discoveries on public-key cryptosystems [3]. The security of the Rivest-Shamir-Adleman (RSA) encryption protocol [25], a widely used protocol for internet transactions, and the elliptic curve encryption protocol [26, 27] is based, respectively, on the difficulty of determining the prime factors of a large number and of solving the discrete logarithm problem, with either problem requiring an impractical amount of classical computing resources and runtime for sufficiently large numbers. As the implementation of Shor’s algorithms on a quantum computer would render these protocols insecure, his discoveries engendered a paradigm shift in the field of cryptography [28–34] and resulted in an acute increase of interest in (and government funding of) research on quantum computing worldwide.

With the ever-growing list of tasks that would be more efficiently performed on a quantum computer, the current drive is to develop a practical physical system for the implementation of a working quantum computer. To assess the advantages and disadvantages of the various physical systems that have been proposed, it is beneficial to more fundamentally understand the requirements for a working quantum computer in any given physical system. It is these requirements that we now discuss.

1.2 The Requirements for Quantum Computing

For any physical system, there exists a fundamental set of requirements that must be satisfied for the implementation of quantum computing. These requirements describe the necessary properties of the system elements that serve as the quantum bits (qubits), e.g. the spin states of individual charges or the energy levels of an atom, both individually and collectively as well as the means by which these elements are controlled. These criteria are typically referred to as the DiVincenzo criteria, after David P. DiVincenzo of IBM, and are given below [20]:

1. A scalable physical system with well characterized qubits.
2. The ability to initialize the state of the qubits to a simple fiducial state, such as $|000\dots\rangle$.
3. Long relevant decoherence times, much longer than the gate operation time.
4. A “universal” set of quantum gates.
5. A qubit-specific measurement capability.

The first and third criteria concern properties that are inherent to the physical system in question. Scalability refers to the ability to construct an architecture consisting of a sufficiently large number of individual qubits and is one of the primary challenges in developing a practical quantum computer. For instance, nuclear spins of molecules in a liquid as implemented in NMR quantum computing [35] have shown considerable success in implementing quantum algorithms for up to several qubits [36–38], but because the total number of qubits is restricted to the number of nuclei in each molecule, this approach is not sufficiently scalable for a working quantum computer.

In addition to scalability, individual qubits in the system must possess a sufficiently long (de)coherence time, i.e. a characteristic timescale indicating the rate at which coherent superpositions deteriorate. As it is these superposition states that provide the quantum parallelism that is central to the power of quantum computing, their deterioration limits the duration during which quantum gate operations may be

performed. Thus, ideal systems are those in which qubit coherence times are much longer than quantum gate operation times, thereby enabling the execution of entire quantum algorithms well within the qubit coherence time.

The second, fourth and fifth criteria all deal with the ability to interface with the proposed physical system, encapsulating the entire computational process of preparation, manipulation and read-out. Preparation of the qubits to a pure state such as $|000\dots\rangle$ or $|111\dots\rangle$ provides the starting point of the computational process, after which the desired quantum algorithm is executed by the set of universal quantum gates, i.e. a set of single and multi-qubit gates that may be combined to construct any unitary operation on any given number of qubits [39]. Read-out, the final stage of the computational process, returns the result of the computation for a particular qubit, ideally without affecting the other qubits in the system. In any read-out scheme, it is crucial to quantify the efficiency of the read-out method so as to determine how many repeated computations are required to achieve sufficiently accurate measurements.

With an understanding of the DiVincenzo criteria in hand, we now briefly survey the various physical systems that have been proposed for quantum computing, viewing their progress in the context of these criteria.

1.3 Candidate Physical Systems for Quantum Computing

In this section we consider some of the candidate implementations of quantum computing, focusing on those systems that have had some success in demonstrating progress towards executing quantum algorithms. As such, systems heralded for their use in quantum communication schemes, such as cavity QED systems [40–42], are not considered here.

1.3.1 Trapped Ions

Ion trap quantum computing is one of the most mature implementations of quantum computing. This approach employs linear arrays of charged atoms laser cooled to

near the zero-point energy [43] and confined in a quadrupole ion trap [44] to perform quantum computations [45–47]. Qubit states in this scheme are the internal states of each ion, which can be the atomic ground state plus an excited state (optical qubits) or two ground state hyperfine levels (hyperfine qubits). Qubit coherence times in either case are very long, approaching seconds and even minutes in the hyperfine case [48], making such qubits highly attractive for quantum computing. For computations, individual qubits are manipulated optically [49] with qubit coupling achieved via the externally controllable Coulomb interaction between ions in the array [45, 50].

In addition to possessing long coherence times, trapped ion qubits have been shown to satisfy the DiVincenzo criteria for initialization [43, 51, 52], universal gates [52–54] and read-out [52, 55]. As for scalability, the original proposal by Cirac and Zoller [45] for a single linear array was restricted to at most tens of ions in a single linear trap [46, 56], limiting the potential for scalability. To mediate this, recent schemes have employed the use of networks of linear traps [46, 57] or anharmonic ion traps [58] to enable the possibility of large-scale quantum computing with trapped ions.

1.3.2 Nuclear Spins in Molecules

This form of quantum computing is based on the use of nuclear spins in a molecule as the qubit states, which have been shown to possess coherence times on the order of 10^3 s when sufficiently isolated from their environments [59, 60]. Because molecules are generally much more difficult to trap than ions, optical approaches to quantum computing analogous to those employed with trapped ions have proven elusive [3]. Instead, practical schemes employing these nuclear spins rely on nuclear magnetic resonance (NMR) techniques with radio frequency (RF) pulses to manipulate and read-out the nuclear spin states [35]. These techniques, however, require a very high number of nuclear spins to achieve a sufficiently high read-out signal. As a result, experiments are typically performed with a molecular liquid at room temperature containing on the order of 10^{23} identical molecules in thermal equilibrium. The molecules in the liquid are taken to be non-interacting as the inter-molecular interactions gen-

erally average out [60].

For the computational process, the ensemble of nuclear spins is perturbed from the completely mixed case by an externally applied DC magnetic field. This perturbation leads to a deviation from the completely mixed ensemble density matrix ρ that can be used to investigate system dynamics. This “deviation density matrix” [35] serves as the initial state of the computation, setting NMR quantum computing apart from other approaches as the initial state of the computation is not a pure state but some mixture that depends on system parameters. Despite the inability to initialize the system to a pure state, NMR quantum computing has demonstrated a number of quantum algorithms such as the Deutsch-Jozsa algorithm [61,62], Grover’s search algorithm [36] and Shor’s factoring algorithm [38]. Despite these successes, the inability to scale the number of usable qubits remains a major drawback for NMR quantum computing, with no practical solution currently in sight.

1.3.3 Electron and Nuclear Spins in Diamond

Given the limitations of NMR quantum computing with molecular liquids, the desire to utilize isolated nuclear spins for quantum computing has led to considerations of solid state systems for their implementation. One such solid state system is diamond, in which the nuclear spin states of ^{13}C atoms in the vicinity of a nitrogen-vacancy (NV) center can be manipulated via the hyperfine coupling between the ^{13}C nuclear spin and the NV center electron spin. One advantage with this approach is the ability to optically detect NV center fluorescence [63], enabling studies of individual electron and nuclear spin states without having to resort to ensemble measurements as with liquid systems. In addition, this system has been shown to possess electron spin coherence times as long as $350\ \mu\text{s}$ [64] and comparable nuclear spin coherence times [65,66] *at room temperature*.

Studies to date have demonstrated the coherent control of the NV center electron spin [67] and the nuclear spin of a nearby ^{13}C atom [65,66] as well as the coherent coupling between the electron and nuclear spins [68]. Initialization of both electron

[64] and nuclear [65] spins has also been shown by employing various combinations of optical, RF and microwave (MW) fields. Nuclear spin initialization has been used to demonstrate a controlled rotation (CROT) gate, a gate that rotates the target bit depending on the state of the control bit, with the NV center electron spin and a nuclear spin serving as the control and target bits, respectively [65]. In addition, this system has been used to demonstrate the successful entanglement of two ^{13}C nuclear spins as well as the entanglement of the NV center electron spin with two ^{13}C nuclear spins [66]. Scalability appears to pose a substantial hurdle for practical implementation, though proposed schemes utilizing distant NV centers in conjunction with optical cavities [69] may provide a potential solution.

1.3.4 Phosphorous Donors in Si (Kane Quantum Computer)

Another proposed implementation of quantum computing that calls upon the use of nuclear spins in a solid state system is the Kane quantum computer [70]. In this implementation, a silicon substrate consisting of isotopically pure ^{28}Si is implanted with an array of equally-spaced individual ^{31}P atoms, each possessing a nuclear spin and a donor electron spin. As with the diamond system, both nuclear and electron spins are capable of possessing long coherence times on the order of ms, though in this case such coherence times generally require that the structure be kept at liquid helium temperatures [71]. The nuclear spins serve as the qubits, with the donor electrons serving both to mediate the interaction between multiple qubits and to provide a read-out signal. In computation, single qubit operations are performed by controlling the hyperfine interaction between the nuclear spin and the donor electron spin via a metal gate located above each ^{31}P atom (“A gates”), while operations involving two adjacent qubits may be performed by controlling the exchange coupling between the two donor electrons via a metal gate located above the space between the ^{31}P atoms (“J gates”). Read-out of individual qubits is performed by the electron nuclear double resonance (ENDOR) method [71–73], which effectively measures the state of the nuclear spin via the donor electron.

The Kane quantum computer would provide a convenient system for single and multi-qubit manipulations as well as read-out, in addition to being highly scalable. The currently prevailing challenge in developing a Kane quantum computer is fabricating Si structures that are doped with *single*, evenly-spaced ^{31}P atoms [74–76]. Because efforts have predominantly focused on improving fabrication technology, progress towards satisfying the DiVincenzo criteria has been limited, though there have been demonstrations of electron and nuclear spin manipulation [73], successful gate control of the localization of the donor electron wavefunction [77] and the successful coherent transfer of superposition states back and forth between the electron and nuclear spins [78].

1.3.5 Superconducting Circuits

Superconducting circuit quantum computers are based on two effects: the quantization of the magnetic flux in a superconducting loop and the macroscopic quantum tunneling of electrons through the insulating barrier between two superconductors in a Josephson junction [79–81]. These two effects result in the manifestation of quantum phenomena on macroscopic scales and can be used to form three different types of qubits based on the macroscopic flux, charge and phase of superconducting circuits [81–83]. The differences between the different types of qubits are beyond the scope of this rudimentary survey, though an excellent discussion of the different types is provided in Reference [81].

Regardless the type, superconducting qubits offer coherence times on the order of microseconds [84, 85] and straightforward scalability but are highly susceptible to electronic noise and require very low operating temperatures on the order of milliKelvin [81, 84, 85]. Despite these difficulties, superconducting circuits have demonstrated single- [86, 87] and multi-qubit [88, 89] operations as well as single-qubit read-out [83, 90]. Recently [85], a two-qubit quantum processor was demonstrated using two superconducting charge qubits coupled by a transmission line cavity [91]. This processor was able to demonstrate both the Deutsch-Jozsa and Grover search algo-

Density of States as a Function of Dimension

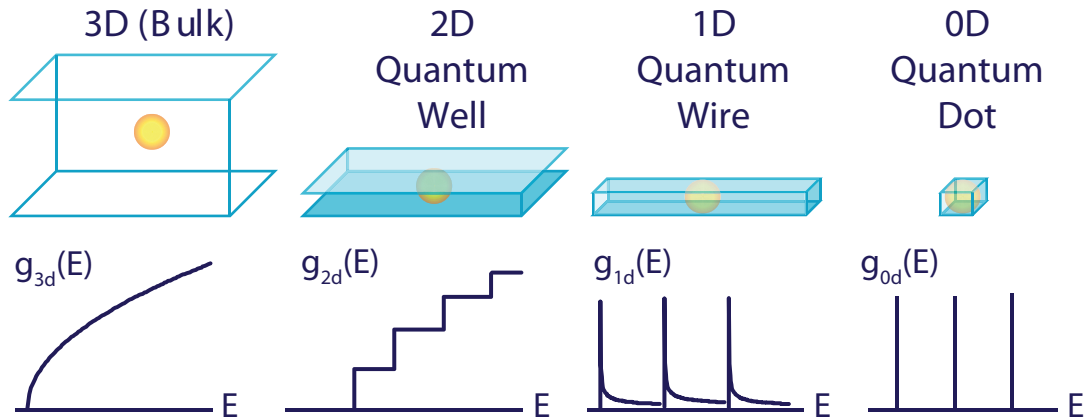


Figure 1.1: Energy density of states for structures of different dimensionality (reproduced with permission from Y. Wu).

rithms, demonstrating progress towards the development of a processor with a higher number of superconducting qubits.

1.3.6 Quantum Dots

Traditionally, the term “quantum dot” has referred to semiconductor nanostructures that are enclosed by a larger-bandgap material and capable of confining carriers such as electron-hole pairs (excitons), electrons and holes to volumes with dimensions are on the order of the Bohr radius or the de Broglie wavelength of the carrier, leading to an atom-like energy density of states (Figure 1.1) [92–95]. This term has since grown to include metallic structures [96–98], carbon nanotubes [99, 100] and gate electrodes that spatially confine a small number of electrons out of a 2D electron gas [101–104]. Both electrostatically defined QDs [18, 104] and semiconductor QDs [19, 105, 106] have been proposed for quantum computing, with each approach offering a unique set of advantages and disadvantages. In both systems, current efforts generally focus on using the spin states of single charges confined in QDs, though previous work in semiconductor QDs has demonstrated optical gates with exciton-based qubits [107, 108].

Electron spins in electrostatically defined QDs have been shown to possess lifetimes on the order of tens of ms [109–111] and coherence times in the range of 100 μs [104, 112] at liquid helium temperatures and are capable of single-shot read-out [110, 111]. Approaches to the coherent control of confined spins generally fall into two categories, electrical [112, 113] and magnetic [114] control, either of which may be straightforwardly implemented “on-chip” in a quantum computing architecture. Single spin manipulations generally require tens of ns to execute [113] while $\sqrt{\text{SWAP}}$ operations that switch the spin states of electrons in two laterally coupled dots [103] require ~ 180 ps [112]. One drawback at present, however, is that neither electric nor magnetic approaches have demonstrated high fidelity initialization of single spins to a fiducial state. In addition, the fabrication of multiply coupled spin qubits remains a significant challenge, presenting a hurdle for scalable architectures [104].

As with electrostatically defined QDs, electron spins confined in semiconductor QDs at liquid helium temperatures have also been shown to possess lifetimes as long as tens of ms [115]. For electrons, intrinsic coherence times on the order of μs [116, 117] have been observed, though the hyperfine interaction between the electron spin and the QD nuclei leads to an inhomogeneously broadened spin coherence time on the order of nanoseconds [112, 118–121]. Unwanted contributions from the nuclear field may potentially be avoided by using the spin states of QD confined holes, as their wavefunctions are “p-like” in nature and interact with a much reduced number of QD nuclei as a result of the smaller wavefunction values in the QD [122–125]. These spins have demonstrated lifetimes on the order of hundreds of μs [123] and have very recently been shown to possess coherence times on the order of several hundred ns [125].

For either type of carrier, spin manipulations in semiconductor QDs are performed *optically*. This approach has demonstrated high-fidelity initialization of a single spin to a pure state [126–129] as well as fast coherent control of an electron spin on picosecond timescales [130, 131], with ultrafast coherent control possible in principle [132, 133]. The potential to perform ultrafast optical manipulations of QD confined spins is a powerful advantage of this approach that would allow a very high number of

gate operations to be performed within the spin coherence time. As of yet, however, a scalable architecture of semiconductor QDs has yet to be realized, though work is being done currently to develop such architectures using either QDs with 2D photonic crystal cavities [134, 135] or planar arrays of QDs in a 1D Bragg cavity [136, 137].

1.4 Thesis Outline

Experiments in this thesis are performed on self-assembled InAs QDs [92, 138]. The general properties of these dots and the process by which they are grown are discussed in Chapter 2. This Chapter also discusses the structural properties of the sample studied and how they influence single QD studies. Basic bandstructure and carrier properties are also discussed, emphasizing the relevant energy levels of a QD charged with a single electron and the selection rules for the lowest lying optical excitations with and without an externally applied DC magnetic field.

Chapter 3 covers the theoretical foundations for the coherent time-resolved optical spectroscopy of a single InAs QD with picosecond pulses based on the density matrix formalism. Theoretical results provide the mathematical form of experimental signals obtained in one- and two-pulse studies using phase-sensitive detection techniques. These results demonstrate the ability to read out the quantum state of a single InAs dot with a single pulse and to measure transient phenomena in two-pulses studies. These transient phenomena include the generation and decay of excited state population in the dot and spin precession in the presence of an externally applied DC magnetic field.

Experimental efforts to verify these theoretical results are presented in Chapter 4, which first discusses the experimental setup employed in all studies covered in this thesis. The basic QD characterization process is also discussed, including the photoluminescence (PL) and Stark shift modulation absorption studies that provide crucial knowledge of the regime in which the QD interacts with incident light. Studies performed with optical pulses indeed verify the theoretical results of Chapter 3, enabling the determination of excited state relaxation times and the g-factors of precessing

spins in the QD.

In Chapter 5, the theory of possible single spin qubit gates in an InAs QD is treated, showing three possible means of controlling the electron spin: detuned circularly polarized optical pulses, spin precession about the externally applied DC magnetic field and geometric phases generated by cyclic evolutions in the QD system. Each method of spin control is expressed in terms of a unitary transformation matrix that is used to show the possible single qubit gates that may be formed by the use of individual or combined spin control mechanisms. Combining the operation of the optical pulses with the magnetic field enables the construction of arbitrary unitary single-qubit operations that may be used with two-qubit gates to operate on an arbitrary number of qubits [39].

Chapter 6 discusses the results of experiments demonstrating the execution of the single qubit gates discussed in Chapter 5. The method of spin initialization by optical pumping [126–129] is first presented, followed by a discussion of the “optical tripwire” read-out method used to observe the various spin control mechanisms. This method of read-out is first applied to one-pulse studies to show the optical control of the electron spin on picosecond timescales via two-photon Raman excitations. Two-pulse studies are then performed to observe spin precession, showing arbitrary rotation of the electron spin about the magnetic field axis. Rotations about the magnetic field axis are also achieved by the use of the geometric phases generated by CW-driven Rabi oscillations in one of the optical transitions in the dot, with each complete oscillation resulting in a π rotation of the spin for a resonant CW field.

Chapter 7 contains proposals for two future experiments in the charged QD system. The first proposed experiment is the density matrix tomography (DMT) [139] of a QD confined spin, a procedure by which the density matrix elements for the electron spin system are determined. The suggested DMT procedure uses a combination of spin precession and an optical pulse to determine these density matrix elements and is important for the evaluation of spin qubit gate fidelities. The second experiment investigates the use of optical pulses rather than a CW field to generate the geometric phases used for spin rotation, as proposed in Reference [133]. Spin rotation via these

pulse-generated geometric phases could be combined with two-photon control of the spin to execute purely optical spin qubit gates. Both proposed experiments would require the development of techniques necessary for quantum computing at the single qubit level and are thus inevitable steps towards the realization of a working quantum computer with QD confined spins.

A summary of the work presented in this thesis is given in Chapter 8.

1.5 Chapter Summary

A brief history of the field of quantum computation was given, discussing some of the theoretical demonstrations that served to ignite interest in the field. The fundamental physical requirements for a working quantum computer, the DiVincenzo criteria, were then presented. A number of candidate physical systems for the implementation of a quantum computer were then presented, with advantages and disadvantages discussed in the context of these criteria. Finally, an outline of the thesis was given, summarizing the topics discussed in each Chapter.

CHAPTER 2

Self-Assembled InAs Quantum Dots: Characteristics and Sample Structure

Self-assembled quantum dots (QDs) are grown either by molecular beam epitaxy or by metalorganic vapor phase epitaxy where growth proceeds in the so-called Stranski-Krastanow mode due to the strain induced by the lattice mismatch between the substrate and the deposited material. During the course of layer-by-layer growth, the deposited material begins to coalesce to form strained “islands” once a critical thickness has been reached, this threshold determined by the materials involved and the growth conditions [Figure 2.1(a)]. Such growth has been demonstrated for film/substrate combinations using III-V semiconductor compounds [92, 138, 140–144], II-VI semiconductor compounds [145–150] and Ge with Si [151–153]. Due to their strong spatial confinement to dimensions on the order of 10^{-8} m and their ability to be organized in 2D and 3D lattices during growth [150, 154, 155], SAQDs are considered highly appealing for a number of device applications. Among these applications are low-threshold QD lasers [142, 156–160], infrared detectors [159, 161–167], quantum repeaters [168–170], single photon sources [171–175], light-emitting diodes [175–178] and, as discussed here, quantum computers [18, 19, 105, 179, 180].

Self-assembled InAs QDs grown on a GaAs substrate, the type studied in this thesis, are arguably the most thoroughly characterized type of self-assembled dot. This Chapter discusses some of the basic properties of the InAs QD sample used, namely, growth, structure, carrier properties and optical selection rules.

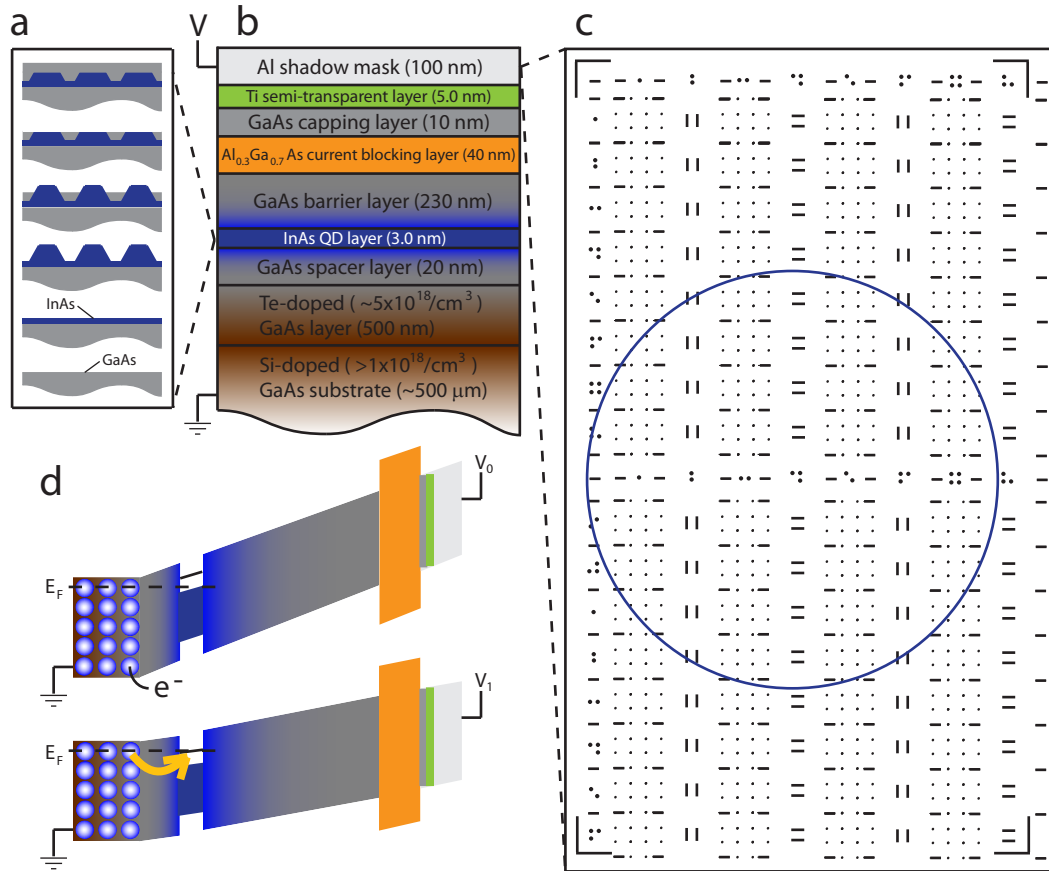


Figure 2.1: (a) Basic depiction of the QD growth process including the indium flush technique for InAs grown on GaAs (from bottom to top). (b) R060913G sample structure diagram showing the configuration of layers and the contacts used for voltage control. (c) Al shadow mask aperture pattern. The smaller apertures are on the order of 1 μm in diameter while the larger braille features and slots have dimensions on the order of 10 μm . Due to the sample mount, only those apertures lying within the blue circle allow for studies in a transmission geometry. (d) Illustration of the charging effect. The sample voltage determines the energy level difference between QD levels and the Fermi energy of the electron reservoir in the n-doped GaAs layer, allowing for different possible charge states in the dot.

2.1 Sample Structure and Growth Process

Experiments in this thesis are performed on a single self-assembled InAs dot contained within a single-layer QD heterostructure sample named “R060913G” with the structure shown in Figure 2.1. Growth begins with the deposition of a 500 nm thick layer of Te-doped GaAs on top of the Si-doped GaAs wafer that serves as the sample substrate and back contact. This layer is grown both to provide potential donor electrons to the QDs through Te dopants and to ensure a high-quality surface for the deposition of subsequent layers. A 20 nm spacer layer of undoped GaAs is then grown atop the Te-doped layer. This layer is speculated to play a role in mitigating the effects of Te diffusion during growth, a phenomenon that has been observed in epitaxy with Te-doped GaSb substrates and is attributed to the high diffusion coefficient of Te [181]. Diffused Te is believed to behave as an ensemble of optically active states whose energies cover the QD transition energy range, thus generally interfering with single dot studies [182]. Of the various InAs QD samples studied in our laboratory, those with thinner spacer layers of ~ 20 nm in thickness show greater suppression of the effects of Te diffusion than thicker spacer layers of ~ 80 nm in thickness, the reasons for which are not well understood at present.

After the deposition of the spacer layer, InAs is then grown layer-by-layer and is highly strained due to the $\sim 7\%$ lattice mismatch between InAs and GaAs. The strained InAs deposition results initially in the formation of a 2D wetting layer (WL). Once the WL reaches a critical thickness of 1-2 monolayers (ML), the Stranski-Krastanow transition occurs and the layer-by-layer growth mode switches to a 3D islanding growth mode where coherently strained QDs are formed. Continued deposition of InAs beyond 2-3 ML leads to the introduction of dislocations in the islands that relax the strain and degrade the electrical and optical properties of the dots [92, 138]. As a result, deposition of InAs is typically terminated shortly after entering the Stranski-Krastanow growth mode to maintain the coherently strained QDs.

After the formation of dots an indium flush technique [183, 184] is applied to truncate the QD heights [Figure 2.1(a)], thereby blue shifting their transition wave-

lengths from around $1\ \mu\text{m}$ to the $920\ \text{nm} - 980\ \text{nm}$ range. This is done to make the QD transition energies accessible to the Ti:Sapph lasers used in our laboratory. In this process, a partial overgrowth layer of GaAs is grown on top of the QD layer, leaving part of the InAs exposed. The strain induced by the overgrowth layer leads to the redistribution of InAs from the exposed portion of the dots to the top of the overgrown GaAs, forming part of an additional WL-like layer. The substrate is heated to eliminate this additional layer and then cooled, after which the rest of the barrier layer is grown. An $40\ \text{nm}\ \text{Al}_{0.3}\text{Ga}_{0.7}\text{As}$ tunnel barrier is then grown to prevent carrier leakage to the top Schottky contact, followed by thin layers of GaAs ($10\ \text{nm}$) and Ti ($5\ \text{nm}$). Finally, a $100\ \text{nm}$ Al shadow mask is grown in which the aperture pattern shown in Figure 2.1(c) is fabricated using electron beam lithography. This pattern contains ordered circular and rectangular apertures that range in size from $\sim 1\ \mu\text{m}$ to tens of μm to generally allow for both single-dot and ensemble studies, though in the case of R060913G the low dot density ($\sim 1/\mu\text{m}^2$) favors single-dot studies.

2.2 QD Charging and Carrier Properties

The structure of R060913G enables selective control of the number of carriers in a given QD via an external voltage applied across the electrodes extending from the Al shadow mask and the back contact [185]. The external voltage effectively tunes the QD energy levels relative to the Fermi energy of the electron gas in the n-doped GaAs substrate and controls the tunneling of electrons to and from the dot. The InAs structures that have been studied in our laboratory generally allow the QD to contain anywhere from one unit of positive charge to two units of negative charge depending on the voltage, though in the case of R060913G only neutral dots and dots containing a single electron have been experimentally observed (as will be shown in Chapter 4).

Figure 2.2 shows simplified depictions of the conduction and valence bands for neutral and negatively charged QDs and their lowest-lying optical excitations. In general, optical excitation of a single QD leads to the generation of an electron hole

pair, resulting in a neutral exciton in the case of an initially neutral dot and a negatively charged exciton, i.e. trion, in the case of a dot initially containing a single electron. As the goal in this work is to demonstrate quantum operations on a qubit defined by the spin states of a QD confined electron, we now focus on the properties of the negatively charged QD and the lowest lying optical excitations.

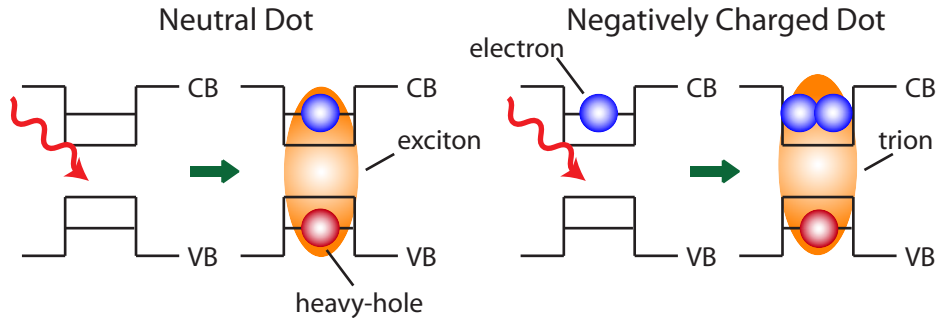


Figure 2.2: Conduction and valence band configurations before and after optical excitation for an initially neutral dot and a dot initially containing a single electron in the conduction band. We consider specifically the lowest-lying excitations. In the case of the negatively charged dot, the electron pair in the conduction band forms a singlet state.

2.3 Energy Level Structure of a Negatively Charged QD

Optical control of the spin of an electron confined in a QD requires a thorough knowledge of the selection rules between the electron spin states and the lowest-lying trion states. Such knowledge necessitates an understanding of the QD band structure that goes beyond the simple depiction of Figure 2.2. Basic theoretical considerations of band structure in direct bandgap bulk semiconductors such as GaAs and InAs based on the tight binding method (TBM) show that the bottom of the conduction band is “s-like” (angular momentum $l \cong 0$) while the top of the valence band is “p-like” ($l \cong 1$) [186]. Although this description of the conduction and valence bands in terms of atomic orbitals breaks down for nonzero wavenumbers k , it provides an adequate description of optical processes in these semiconductors for excitation energies near the direct bandgap energy, due to the fact that the k values of the electrons and holes involved in these excitations are nearly zero. This reasoning also applies to single

QDs, where the reduced number of sites in the QD crystal lattice (compared to the bulk case) leads to an ever greater restriction on the number of k values near $k = 0$ that may be involved in near-bandgap excitations. Thus, despite the lack of spherical symmetry in the QD system, we take the conservation of angular momentum to be *quasi*-satisfied and express the states of the dot in terms of atom-like orbitals.

In addition to orbital angular momentum, the spin angular momentum of carriers in the conduction and valence bands must also be taken into account. Inclusion of spin in TBM calculations yields the heavy-hole (HH), light-hole (LH) and split-off (SO) states of the valence band. For total angular momentum $j = l + s$ and projection m_j , the HH and LH refer to the $\pm 3/2$ and $\pm 1/2$ projections, respectively, for $j = 3/2$ and are degenerate at the top of the valence band while the SO refers to the $\pm 1/2$ projections for $j = 1/2$ and is separated by the spin-orbit interaction energy. It is well known that strain in these systems can break the HH-LH degeneracy, with tensile strain in the growth plane leading to a higher LH and compressive strain leading to a higher HH [186]. For strained InAs dots, the in-plane strain is compressive, leading to a higher HH as well as mixing between the HH and the LH [187–190]. We note that HH-LH mixing effectively rotates the polarization axis of the QD selection rules with respect to the laboratory frame but does not qualitatively change the relative polarizations of the different optical transitions [191]. Thus, for the purpose of determining the selection rules it is sufficient to ignore the mixing and take the HH to be the top-most state of the valence band.

To determine the selection rules for a QD containing a single electron, one must generally calculate the matrix elements of the position operator $\hat{\mathbf{r}}$, i.e. $\langle m | \hat{\mathbf{r}} | n \rangle$ where $\langle m |$ and $| n \rangle$ are QD states, as the form of the optical coupling between QD levels—in the dipole approximation—is determined by the dipole interaction $V = -\boldsymbol{\mu} \cdot \mathbf{E} = e\mathbf{r} \cdot \mathbf{E}$ where \mathbf{E} is the electric field. We seek these matrix elements for the situation depicted in Figure 2.3(a) with optical excitation along \hat{z} , the sample growth axis. The levels of interest are the four shown in Figure 2.3(b) where the ground states are the spin states of the confined electron and the excited states are the trion states for different heavy-hole spin projections (with the conduction band electrons in a singlet state).

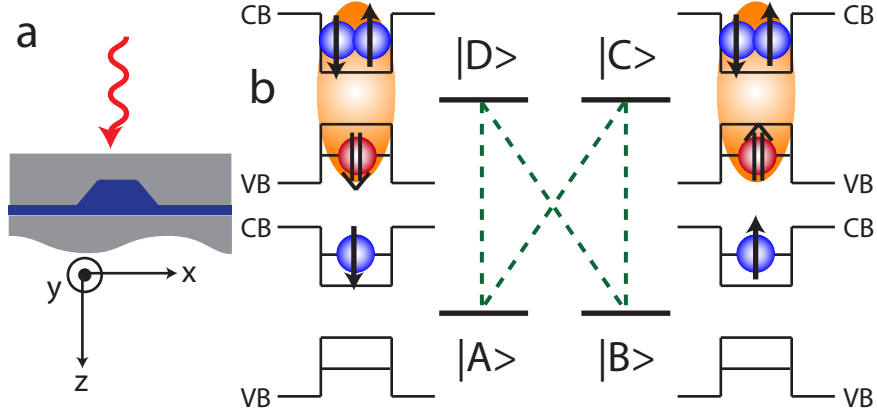


Figure 2.3: (a) QD excitation scheme and axis orientation. Optical excitation is along the growth axis \hat{z} . (b) The four levels formed by the electron spin ground states and the two heavy-hole spin states of the trion, quantized along some axis that depends on system parameters. The dashed green lines indicate the transitions of interest. \uparrow (\downarrow) indicates the projection of the total angular momentum m_j of the electron, corresponding to a value of $1/2$ ($-1/2$) while \uparrow (\downarrow) corresponds to a heavy-hole m_j value of $3/2$ ($-3/2$)

Although the confinement provided by self-assembled QDs allows for a number of additional excited states in the dot, these states are separated in energy by tens of mV [192] and can thus be ignored. Matrix elements for the position operator are calculated between the transitions indicated by the dashed green arrows. As the axis of spin quantization depends on external parameters, viz. magnetic field, we specifically consider two cases: 1) an external DC magnetic field $\mathbf{B}_{\text{ext}} = 0$ and 2) $\mathbf{B}_{\text{ext}} = B\hat{x}$ (Voigt geometry).

2.3.1 Selection Rules for $\mathbf{B}_{\text{ext}} = 0$

In the absence of an externally applied magnetic field, stationary states for the four levels can be expressed in any basis. However, since we are interested in the interaction of light with the QD, it is most convenient to take the optical axis as the quantization axis for the determination of selection rules. The first step, then, is to express the QD states in terms of the quantum numbers l , s , j , and m_j , noting that only these quantum numbers determine the axis of polarization for a given optical transition. Expressions in terms of these quantum numbers are given in Table 2.1,

$ \text{level}\rangle$	$ \text{CB} \text{VB}\rangle$	$ l s j m_j\rangle$
$ A\rangle \rightarrow z+\rangle (\bar{1}\rangle)$	$ \uparrow -\rangle$	$ 0 \frac{1}{2} \frac{1}{2} \frac{1}{2}\rangle$
$ B\rangle \rightarrow z-\rangle (\bar{2}\rangle)$	$ \downarrow -\rangle$	$ 0 \frac{1}{2} \frac{1}{2} \frac{-1}{2}\rangle$
$ C\rangle \rightarrow T_z-\rangle (\bar{3}\rangle)$	$ \downarrow\uparrow \downarrow\rangle$	$ 1 \frac{1}{2} \frac{3}{2} \frac{-3}{2}\rangle$
$ D\rangle \rightarrow T_z+\rangle (\bar{4}\rangle)$	$ \downarrow\uparrow \uparrow\rangle$	$ 1 \frac{1}{2} \frac{3}{2} \frac{3}{2}\rangle$

Table 2.1: Energy level labels and expressions in terms of spin and angular quantum numbers for $\mathbf{B}_{\text{ext}} = 0$. The notation $|\bar{\square}\rangle$ indicates a \hat{z} basis state and is used to distinguish from \hat{x} basis states.

which also shows how the states have been relabeled to reflect the \hat{z} -axis quantization. We then express the position vector \mathbf{r} in irreducible tensor form, i.e.

$$\mathbf{r} = -rC_{-1}^1 \hat{\epsilon}_{+1} + rC_0^1 \hat{\epsilon}_0 - rC_{+1}^1 \hat{\epsilon}_{-1} \quad (2.1)$$

where $\hat{\epsilon}_{\pm 1} = \mp \hat{\sigma}_{\pm} = \mp \frac{1}{2}(\hat{x} \pm i\hat{y})$, $\hat{\epsilon}_0 = \hat{z}$ and C_m^l are the Racah tensors

$$C_m^l = \left(\frac{4\pi}{2l+1} \right)^{\frac{1}{2}} Y_m^l \quad (2.2)$$

for spherical harmonics Y_m^l . Since we are only concerned with the polarization axes of the transitions, we need only consider the matrix elements for the operator corresponding to the quantity \mathbf{r}/r . The details of this calculation are given in Appendix A, the results of which are displayed in Figure 2.4(a). We see that without an external field the four levels form two degenerate two-level systems with circularly cross-polarized selection rules. As the transitions indicated by the dashed red arrows are optically forbidden ($\Delta j = \pm 2$) these two two-level systems are optically independent.

2.3.2 Selection Rules for $\mathbf{B}_{\text{ext}} = \mathbf{B}\hat{x}$

A magnetic field applied along \hat{x} serves to quantize the spins of the QD states along the magnetic field axis and lift the Kramers' degeneracy for the spin states of both the ground state electron and the heavy-hole of the trion, leading to Zeeman splittings between the originally degenerate states. To determine the selection rules in this case, the new basis states must first be expressed in terms of the \hat{z} basis states

$ \text{level}\rangle$	\hat{z} basis expr.
$ A\rangle \rightarrow x+\rangle (1\rangle)$	$\frac{1}{\sqrt{2}} [z-\rangle + z+\rangle]$
$ B\rangle \rightarrow x-\rangle (2\rangle)$	$\frac{1}{\sqrt{2}} [z-\rangle - z+\rangle]$
$ C\rangle \rightarrow T_x-\rangle (3\rangle)$	$\frac{1}{\sqrt{2}} [T_z-\rangle - T_z+\rangle]$
$ D\rangle \rightarrow T_x+\rangle (4\rangle)$	$\frac{1}{\sqrt{2}} [T_z-\rangle + T_z+\rangle]$

Table 2.2: Energy level labels and expressions in terms of \hat{z} basis states for $\mathbf{B}_{\text{ext}} = B\hat{x}$. The notation $|\square\rangle$ (no overline) indicates an \hat{x} basis state.

before the matrix elements of \mathbf{r}/r can be calculated. The transformation relations between the basis states can be determined by diagonalizing the Hamiltonian, the details of which are handled in the Appendix B. The transformation relations are summarized in Table 2.2.

Figure 2.4(b) shows the configuration of energy levels and selection rules for the case of a magnetic field applied in the Voigt profile. In addition to lifting the Kramers' degeneracy, the magnetic field also enables the optical coupling of each electron spin ground state to both trion states by linearly polarized selection rules. These selection rules determine the polarization required to optically control the electron spin and, in conjunction with the electron and heavy-hole Zeeman splittings, play a crucial role in determining the axes about which the spin vector may be optically rotated. The consequences of these selection rules are discussed in more detail in Chapter 5.

2.4 Chapter Summary

An overview of the general properties and applications of self-assembled QDs was given. The structure and growth of the sample used for single-dot studies in this thesis work were then discussed. QD band structure was then discussed for different charge states, with an emphasis on the band structure structure of a dot containing a single electron in the conduction band. Selection rules between the ground states of a negatively charged dot and the lowest lying trion states were then derived with and without an external DC magnetic field applied in the Voigt geometry. The

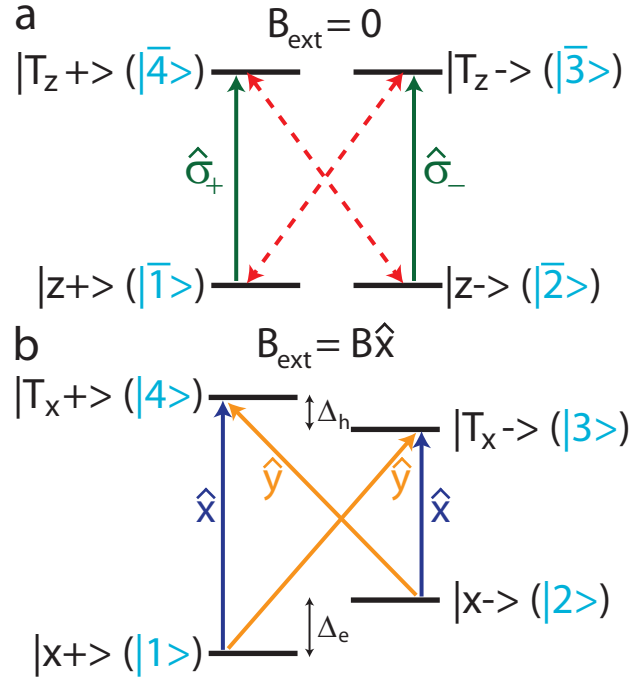


Figure 2.4: Diagrams illustrating the arrangement of levels and transition selection rules for (a) $B_{\text{ext}} = 0$ and (b) $B_{\text{ext}} = B\hat{x}$. The dashed red arrows indicate optically forbidden transitions. $\Delta_e(\Delta_h)$ are the electron and heavy-hole Zeeman splittings. The state labels used for mathematical expressions in this thesis are given by the light blue text.

classification of these selection rules is crucial to the understanding of how optical fields may be used to prepare, manipulate and read-out the electron spin, as will be seen in the following Chapters.

CHAPTER 3

Control and Read-Out of a Single InAs QD with Picosecond Optical Pulses: Theory

QDs containing a single spin have received much attention over the last several years due to demonstrations of their viability for use in quantum computing schemes [18, 19, 104, 106]. A substantial reason for this is the observation of both a long spin lifetime [109, 110, 115] and a long spin coherence time [112, 116, 119, 120] in these systems, an important requirement for quantum computing. A common approach to obtaining values for the spin lifetime and the spin coherence time in QDs is by performing time-resolved studies of a single QD spin, though there have been cases where these values have been extracted from ensemble studies [116]. The majority of these time-resolved single QD spin studies have been performed either with electrostatically defined QDs in a 2D electron gas [101, 102] or with interface fluctuation QDs defined by monolayer fluctuations at the junction of GaAs and AlGaAs quantum wells [119, 193] rather than with self-assembled QDs. This is due mostly to the difficulty of time-resolved studies of a single self-assembled QD spin, which often require optical read-out techniques that are hampered by the small optical dipole moments of self-assembled QDs [194]. As a result, most transient optical studies of a spin confined in a single self-assembled QD have measured the PL from a single dot [131] or the photocurrent of a dot embedded in a photodiode structure [195, 196]. Both of these methods rely upon the relaxation of QD states for measurement, whether it is the decay of excited states for PL measurements or the tunneling of carriers for photocurrent measurements.

The ability to coherently probe a single self-assembled QD with an optical pulse would provide a means of performing time-resolved studies of a single QD spin that does not rely upon state relaxation, potentially enabling spin lifetime and coherence time measurements as well as the characterization of spin qubit gate operations [139]. In this Chapter, we discuss the theoretical foundations for time-resolved optical studies of a single spin confined in an InAs QD using the density matrix formalism. We first discuss how an optical pulse may be used to probe an optical transition in a single self-assembled QD and then show how this can be applied to pump-probe studies to investigate transient QD phenomena such as trion decay and spin precession. We consider studies both with and without an external magnetic field applied in the Voigt geometry, with analytical expressions provided for the measured signals in each case.

3.1 Pulse-Driven Two-Level System

To illustrate how pulsed optical read-out of a single InAs QD is achieved, we first examine the pulsed optical excitation of the two-level system shown in Figure 3.1 that represents one of the optical transitions in the QD. For the optical excitation we specifically consider a hyperbolic secant pulse of the form

$$\mathbf{E}(\mathbf{r}, t) = \frac{1}{2}E(\mathbf{r})\text{sech}\left(\frac{t}{\tau}\right) [\hat{\sigma}_+ e^{i(\mathbf{k}\cdot\mathbf{r}-\Omega t)} + c.c.] \quad (3.1)$$

where $\sigma_{\pm} = \hat{x} \pm i\hat{y}$ and for the time being we leave the spatial profile and propagation direction unspecified. To determine the behavior of the system under such excitation, we utilize the formalism of the density matrix [197]. This is done by first expressing the wavefunction for our two-level system in the standard amplitude picture,

$$|\Psi(t)\rangle = c_1(t)|1\rangle + c_2(t)|2\rangle \quad (3.2)$$

$$|c_1(t)|^2 + |c_2(t)|^2 = 1 \quad (3.3)$$

where c_i is the probability amplitude of state $|i\rangle$. The density matrix is then defined as

$$\rho(t) = \begin{bmatrix} c_1(t)c_1^*(t) & c_1(t)c_2^*(t) \\ c_2(t)c_1^*(t) & c_2(t)c_2^*(t) \end{bmatrix} = \begin{bmatrix} \rho_{11}(t) & \rho_{12}(t) \\ \rho_{21}(t) & \rho_{22}(t) \end{bmatrix} \quad (3.4)$$

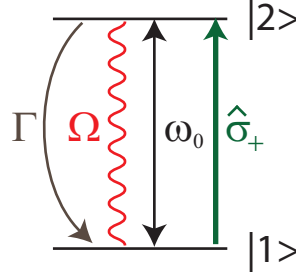


Figure 3.1: Two-level system representing one of the optical transitions in a QD. ω_0 is the angular frequency corresponding to the energy difference between the states, Γ is the excited state decay rate, Ω is the laser frequency, which is set equal to ω_0 , and $\hat{\sigma}_+$ indicates the optical polarization that drives the transition.

where the diagonal and off-diagonal terms are often referred to as “populations” and “coherences,” respectively. This formalism enables the generation of the system equations of motion, or the density matrix equations (DME), using the expression

$$\dot{\rho}_{ij} = \frac{1}{i\hbar} [H, \rho]_{ij} - \text{decay}_{ij} \quad (3.5)$$

where H is the Hamiltonian for the two-level system and “decay” indicates terms accounting for the decay of density matrix elements, e.g. terms containing the coherence decay rate γ or the excited state relaxation rate Γ .

The Hamiltonian for the two level system has the form $H = H_0 + V$ where H_0 is the Hamiltonian in the absence of any optical driving fields and $V = -\boldsymbol{\mu} \cdot \mathbf{E}$ is the dipole interaction potential for a transition dipole $\boldsymbol{\mu}$. To determine the matrix form of H , we must determine the matrix forms of H_0 and V . The matrix representation of H_0 is simply a diagonal matrix consisting of the energy eigenvalues. The matrix form of V can be determined by evaluating the quantities

$$\langle i|V|j\rangle = \frac{1}{2} \text{sech}\left(\frac{t}{\tau}\right) \langle i|E(\mathbf{r})\boldsymbol{\mu} \cdot [\hat{\sigma}_+ e^{i(\mathbf{k}\cdot\mathbf{r}-\Omega t)} + c.c.]|j\rangle \quad (3.6)$$

for each combination of i and j . To enable the determination of these quantities, we take states $|1\rangle$ and $|2\rangle$ to represent, say, the $|z+\rangle$ and $|T_z+\rangle$ states of the dot and utilize the fact that the spatial extent of the QD levels (~ 10 nm) [198] is much smaller than both the wavelength of the optical field (~ 1 μm) and typical beam profile dimensions (~ 10 μm). Thus, we make the substitutions $E(\mathbf{r}) \rightarrow E$ and $e^{i\mathbf{k}\cdot\mathbf{r}} \rightarrow 1$ (dot at the

origin in the lab frame) and then calculate the V matrix elements using the matrix elements of $\boldsymbol{\mu}$ (Appendix A). The total Hamiltonian can then be written as

$$H = \hbar \begin{bmatrix} 0 & R_{12} \\ R_{21} & \omega_0 \end{bmatrix} \quad (3.7)$$

where

$$R_{12} = R_{21}^* = -\chi \operatorname{sech} \left(\frac{t}{\tau} \right) e^{i\Omega t}, \quad \chi = \frac{\mu E}{2\hbar}. \quad (3.8)$$

Use of Equations 3.5 and 3.7 leads to the DME

$$\dot{\rho}_{11} = -i\chi \operatorname{sech} \left(\frac{t}{\tau} \right) [e^{-i\Omega t} \rho_{12} - e^{i\Omega t} \rho_{21}] + \Gamma \rho_{22} \quad (3.9)$$

$$\dot{\rho}_{22} = i\chi \operatorname{sech} \left(\frac{t}{\tau} \right) [e^{-i\Omega t} \rho_{12} - e^{i\Omega t} \rho_{21}] - \Gamma \rho_{11} \quad (3.10)$$

$$\dot{\rho}_{12} = -(\Gamma/2 - i\omega_0) \rho_{12} + i\chi \operatorname{sech} \left(\frac{t}{\tau} \right) e^{i\Omega t} [\rho_{22} - \rho_{11}] \quad (3.11)$$

$$\dot{\rho}_{21} = -(\Gamma/2 + i\omega_0) \rho_{21} - i\chi \operatorname{sech} \left(\frac{t}{\tau} \right) e^{-i\Omega t} [\rho_{22} - \rho_{11}] \quad (3.12)$$

where we have assumed the absence of any pure dephasing mechanisms so that $\gamma = \Gamma/2$. To simplify the solving of these DME, we take $\tau \ll 1/\gamma$, i.e. a pulse width much shorter than the excited state dephasing time. For pulse widths of ~ 2 ps, this is certainly the case in self-assembled QDs where excited state lifetimes have been measured to be on the order of 1 ns [128,199]. In addition, we for now consider system dynamics only on time scales much shorter than the excited state relaxation time. This allows us to ignore the decay terms in the DME to obtain analytic expressions for the density matrix elements.

To solve the DME with these simplifications, we move into the field interaction picture (FIP) using the transformations

$$\rho_{12} = e^{i\Omega t} \tilde{\rho}_{12}, \quad \rho_{21} = e^{-i\Omega t} \tilde{\rho}_{21} \quad (3.13)$$

and make the rotating wave approximation (RWA) ($e^{\pm 2i\Omega t} \sim 0$), thereby eliminating the $e^{\pm i\Omega t}$ terms from the FIP DME. Analytic expressions for the solutions obtained

in the FIP are then transformed back into the standard Schrödinger picture, yielding

$$\rho_{11}(t) = \frac{1}{2} \left[\rho_{tot} - i \left(\rho_{12}^{[0]} - \rho_{21}^{[0]} \right) \sin[\theta(t)] - \left(\rho_{22}^{[0]} - \rho_{11}^{[0]} \right) \cos[\theta(t)] \right] \quad (3.14)$$

$$\rho_{22}(t) = \frac{1}{2} \left[\rho_{tot} + i \left(\rho_{12}^{[0]} - \rho_{21}^{[0]} \right) \sin[\theta(t)] + \left(\rho_{22}^{[0]} - \rho_{11}^{[0]} \right) \cos[\theta(t)] \right] \quad (3.15)$$

$$\rho_{12}(t) = \frac{e^{i\Omega t}}{2} \left[\left(\rho_{12}^{[0]} + \rho_{21}^{[0]} \right) + \left(\rho_{12}^{[0]} - \rho_{21}^{[0]} \right) \cos[\theta(t)] + i \left(\rho_{22}^{[0]} - \rho_{11}^{[0]} \right) \sin[\theta(t)] \right] \quad (3.16)$$

$$\rho_{21}(t) = \frac{e^{-i\Omega t}}{2} \left[\left(\rho_{12}^{[0]} + \rho_{21}^{[0]} \right) - \left(\rho_{12}^{[0]} - \rho_{21}^{[0]} \right) \cos[\theta(t)] - i \left(\rho_{22}^{[0]} - \rho_{11}^{[0]} \right) \sin[\theta(t)] \right] \quad (3.17)$$

where $\rho_{ij}^{[0]} = \rho_{ij}(-\infty)$ is the initial value of the density matrix element prior to excitation, ρ_{tot} is the total population in the two level system at any given time and

$$\theta(t) = \frac{1}{\hbar} \int_{-\infty}^t dt' \boldsymbol{\mu} \cdot \mathbf{E}(t') = \pi\chi\tau + 4\chi\tau \tan^{-1} \left[\tanh \left(\frac{t}{2\tau} \right) \right] \quad (3.18)$$

is the time-dependent pulse area. With the solutions to the DME determined we now consider the form of the electric field \mathbf{E}_s radiated by the dot as a result of the optically induced polarization in the QD

$$\mathbf{P} = \boldsymbol{\mu}_{12}\rho_{21} + \boldsymbol{\mu}_{21}\rho_{12}. \quad (3.19)$$

To obtain the form of \mathbf{E}_s we need to treat the optically induced polarization as a source term in Maxwell's Equations, leading to the Maxwell-Bloch equations. Solutions to the Maxwell-Bloch equations express \mathbf{E}_s in terms of density matrix elements, demonstrating that experimental measurements of the electric field radiated by a single QD provide a means of performing time-resolved studies of the quantum states of the QD.

3.2 Maxwell-Bloch Equations

With the solutions to the DME for the two-level system already in hand, we consider Maxwell's equations in the absence of any free charges ($\rho = 0$) or currents ($\mathbf{J} = 0$) [200]:

$$\begin{aligned} \nabla \cdot \mathbf{D} &= 0 & \nabla \times \mathbf{H} &= \frac{\partial \mathbf{D}}{\partial t} \\ \nabla \cdot \mathbf{B} &= 0 & \nabla \times \mathbf{E}_s + \frac{\partial \mathbf{B}}{\partial t} &= 0 \end{aligned} \quad (3.20)$$

with

$$\mathbf{H} = (1/\mu_M)\mathbf{B}, \quad \mathbf{D} = \epsilon\mathbf{E}_s + \mathbf{P}$$

where ϵ and μ_M are the electric permittivity and magnetic permeability, respectively.

These equations can be used to form the wave equation

$$\nabla(\nabla \cdot \mathbf{E}_s) - \nabla^2 \mathbf{E}_s + \mu_M \epsilon \frac{\partial^2 \mathbf{E}_s}{\partial t^2} = -\mu_M \frac{\partial^2 \mathbf{P}}{\partial t^2} \quad (3.21)$$

which can be solved by applying a series of approximations. First, we take \mathbf{P} to have the form of a wave propagating along \hat{z} and ignore any spatial variation of \mathbf{P} in the plane transverse to the propagation direction. This approximation effectively disregards “transverse” effects such as self-focusing [201] and allows us to set $\nabla \cdot \mathbf{P} \sim 0$. Along with the Gauss’ Law (Equation 3.20), this leads to

$$\nabla \cdot \mathbf{E}_s = \frac{1}{\epsilon} (\nabla \cdot \mathbf{D} - \nabla \cdot \mathbf{P}) = 0$$

where Equation 3.21 can now be written as

$$\frac{\partial^2 \mathbf{E}}{\partial z^2} - \mu_M \epsilon \frac{\partial^2 \mathbf{E}_s}{\partial t^2} = -\mu_M \frac{\partial^2 \mathbf{P}}{\partial t^2}. \quad (3.22)$$

To solve Equation 3.22 we invoke the phase matching condition and write \mathbf{P} and \mathbf{E}_s as

$$\mathbf{P} = \frac{1}{2} (\tilde{\mathbf{P}} + \tilde{\mathbf{P}}^*) \quad (3.23)$$

$$\mathbf{E}_s = \frac{1}{2} (\tilde{\mathbf{E}}_s + \tilde{\mathbf{E}}_s^*) \quad (3.24)$$

where

$$\begin{Bmatrix} \tilde{\mathbf{P}} \\ \tilde{\mathbf{E}}_s \end{Bmatrix} = \begin{Bmatrix} P(z, t) \\ E_s(z, t) \end{Bmatrix} \hat{e}^{i(k_z z - \omega t)}. \quad (3.25)$$

From the linearity of Equation 3.22 and the orthogonality of the time oscillating components of \mathbf{P} and \mathbf{E}_s , it suffices to solve for $\tilde{\mathbf{P}}$ and $\tilde{\mathbf{E}}_s$, as the conjugate terms are obtained in the same fashion. To do this, we make the slowly-varying envelope approximation (SVEA), which applies to pulses whose optical periods are much shorter

than the pulse width in time and whose optical wavelengths are much shorter than the spatial profile full width at half maximum (FWHM), as is the case with the pulses considered here. This permits the elimination of second order and higher derivatives in space and first and higher order derivatives in time, leading to the expression

$$\hat{e}e^{i(k_z z - \omega t)} \left[\left(2ik_z \frac{\partial}{\partial z} - k_z^2 + \mu_M \epsilon \omega^2 \right) E_s(z, t) + \mu \omega^2 P(z, t) \right] = 0$$

which can be further simplified by recognizing that $k_z^2 = \mu_M \epsilon \omega^2$. Considering only the expression in the brackets leaves us with the relation

$$\frac{\partial}{\partial z} E_s(z, t) = \frac{ik_z}{2\epsilon} P(z, t). \quad (3.26)$$

As the spatial extent of the QD along the optical axis is much shorter than the optical wavelength, the z derivative can be replaced in terms of a length a reflecting the sample thickness, leading to the expression

$$E_s(z, t) = \frac{iak_z}{2\epsilon} P(z, t). \quad (3.27)$$

Multiplication of both sides by $\hat{e}e^{i(k_z z - \omega t)}$ and use of Equation 3.19 yields the Maxwell-Bloch equations

$$\tilde{\mathbf{E}}_s = \frac{iak_z}{\epsilon} \boldsymbol{\mu}_{12} \rho_{21} \quad (3.28)$$

$$\tilde{\mathbf{E}}_s^* = -\frac{iak_z}{\epsilon} \boldsymbol{\mu}_{21} \rho_{12} \quad (3.29)$$

where we have elected to express $\tilde{\mathbf{E}}_s(\tilde{\mathbf{E}}_s^*)$ in terms of $\rho_{21}(\rho_{12})$ (Equations 3.16 and 3.17) in order to preserve the association of the $\tilde{\square}(\tilde{\square}^*)$ terms with negative (positive) frequencies (Equation 3.25). The total electric field \mathbf{E}_s can now be expressed as

$$\mathbf{E}_s = \frac{iak_z}{\epsilon} (\boldsymbol{\mu}_{12} \rho_{21} - \boldsymbol{\mu}_{21} \rho_{12}) = -\frac{2ak_z}{\epsilon} \text{Im}[\boldsymbol{\mu}_{12} \rho_{21}] \quad (3.30)$$

and serves as the crux of pulsed optical measurements of single InAs QDs.

It must be noted that the plane wave approximation (i.e. $\nabla \cdot \mathbf{P} \sim 0$) applied in the derivation of the Maxwell-Bloch equations above is generally insufficient to accurately describe the form of the total radiated field \mathbf{E}_s . In reality, determination of the mathematical form of \mathbf{E}_s becomes non-trivial when taking into account the shape of

the dot and is even further complicated by the presence of the nearby apertures on the aluminum shadow mask. Nevertheless, the plane wave description of the QD radiated field at the surface of a photodetector in the far field is an acceptable approximation that enables determination of QD physics. As such, the Maxwell-Bloch equations, as expressed in Equations 3.28 and 3.29, are useful for describing the mathematical form of experimentally measured signals. In the following section, we use these Maxwell-Bloch equations to discuss the theory of the phase-sensitive detection technique that is used to effectively probe the time-dependent density matrix elements of the QD.

3.3 Phase-Sensitive Detection of QD States

To obtain measurements of the QD density matrix elements, we perform homodyne measurements of the interference between the radiated field \mathbf{E}_s and the excitation field \mathbf{E} using a square-law detector that effectively integrates the square of the vector sum of the fields in time over its optically active surface. The detector is oriented in the \hat{x} - \hat{y} plane at a particular point along the \hat{z} axis (in the far field) and is taken to possess an active area much larger than the spatial profile of the excitation pulse. The spatial dependence of the vector sum is then integrated out, allowing us to focus on the integral in time, which yields the photocurrent signal

$$I_{\text{sig}} = K \int_{-\infty}^{\infty} dt (\mathbf{E} + \mathbf{E}_s)^2 \quad (3.31)$$

where K is a proportionality constant reflecting the photosensitivity of the detector. To calculate this integral, we reexpress the excitation field as

$$\mathbf{E} = \frac{1}{2} \left[E \hat{\sigma}_+ \text{sech} \left(\frac{t}{\tau} \right) e^{-i\Omega t} + E \hat{\sigma}_- \text{sech} \left(\frac{t}{\tau} \right) e^{i\Omega t} \right] = \frac{1}{2} (\tilde{\mathbf{E}} + \tilde{\mathbf{E}}^*) \quad (3.32)$$

and expand the square of the vector sum as

$$(\mathbf{E}_s + \mathbf{E})^2 = \mathbf{E}_s^2 + \mathbf{E}^2 + 2(\mathbf{E}_s \cdot \mathbf{E}) \quad (3.33)$$

$$(\mathbf{E}_s + \mathbf{E})^2 = \mathbf{E}_s^2 + \mathbf{E}^2 + \frac{1}{2} (\tilde{\mathbf{E}}_s \cdot \tilde{\mathbf{E}} + \tilde{\mathbf{E}}_s \cdot \tilde{\mathbf{E}}^* + \tilde{\mathbf{E}}_s^* \cdot \tilde{\mathbf{E}} + \tilde{\mathbf{E}}_s^* \cdot \tilde{\mathbf{E}}^*). \quad (3.34)$$

Equation 3.34 can be immediately simplified by recognizing that the terms $\tilde{\mathbf{E}}_s \cdot \tilde{\mathbf{E}}$ and $\tilde{\mathbf{E}}_s^* \cdot \tilde{\mathbf{E}}^*$ oscillate at twice the optical frequency and thus average out to zero on the

square-law detector. Further, we consider the specific case where the radiated field \mathbf{E}_s is modulated at some frequency ω_{ref} , enabling the use of a lock-in amplifier attached to the detector output to detect only those components of the photocurrent signal I_{sig} that are modulated at ω_{ref} . In this case, only the second and third parenthesized terms in Equation 3.34 contribute to the lock-in detected photocurrent, i.e.

$$I_{\text{sig}}^{\text{LI}} = \frac{1}{2}K \int_{-\infty}^{\infty} dt \left(\tilde{\mathbf{E}}_s \cdot \tilde{\mathbf{E}}^* + \tilde{\mathbf{E}}_s^* \cdot \tilde{\mathbf{E}} \right). \quad (3.35)$$

Using the Maxwell-Bloch equations along with Equations 3.13 and 3.32 gives us

$$I_{\text{sig}}^{\text{LI}} = \frac{1}{\epsilon} K a k_z \mu E \int_{-\infty}^{\infty} dt \operatorname{sech} \left(\frac{t}{\tau} \right) \operatorname{Im} [\tilde{\rho}_{12}(t)] \quad (3.36)$$

which, using Equation 3.16, becomes

$$I_{\text{sig}}^{\text{LI}} = \frac{1}{\epsilon} K a k_z \mu E \times \left\{ \operatorname{Im} \left[\rho_{12}^{[0]} \right] \int_{-\infty}^{\infty} dt \operatorname{sech} \left(\frac{t}{\tau} \right) \cos[\theta(t)] + (\rho_{22}^{[0]} - \rho_{11}^{[0]}) \int_{-\infty}^{\infty} dt \operatorname{sech} \left(\frac{t}{\tau} \right) \sin[\theta(t)] \right\}. \quad (3.37)$$

Evaluation of the integrals in Equation 3.37 yields the final expression

$$I_{\text{sig}}^{\text{LI}} = 2 \sqrt{\frac{\mu_M}{\epsilon}} K a (\hbar \omega_0) \left\{ \frac{1}{2} \operatorname{Im} \left[\rho_{12}^{[0]} \right] \sin[\theta(\infty)] + (\rho_{22}^{[0]} - \rho_{11}^{[0]}) \sin^2[\theta(\infty)/2] \right\} \quad (3.38)$$

where $\theta(\infty) = 2\pi\chi\tau$ (from Equation 3.18). Equation 3.38 gives the important result that the lock-in detected interference between the transmitted pulse and the QD radiated field depends on both the density matrix elements of the driven transition prior to excitation and the pulse area. Further, selection of the proper excitation pulse area allows for the isolation of either the coherence ($\rho_{12}^{[0]}$) or the population difference ($\rho_{22}^{[0]} - \rho_{11}^{[0]}$) immediately before the arrival of the pulse. Application of this read-out technique to pump-probe studies enables measurement of pump-induced changes in the QD states via the probe. We now consider the experimentally determined signals for studies with and without an external DC magnetic field, highlighting theoretically observable phenomena such as trion decay, Rabi oscillations between the electron and trion states, and electron and heavy-hole spin precession.

3.4 Pump-Probe Studies: $\mathbf{B}_{\text{ext}} = 0$

Resonant pump-probe studies in the absence of any externally applied magnetic fields enable observation of trion excitation and decay as well as pump-driven Rabi oscillations between the electron and trion states. To see this, we consider the case where both the pump and probe pulses are $\hat{\sigma}_+$ polarized and thus only excite the $|z+\rangle$ to $|T_z+\rangle$ transition. We treat the problem by first obtaining solutions for the case of pump excitation in the absence of decay and then using these solutions to provide the initial conditions for the freely-evolving system. The solutions for the freely-evolving case are then used as the “initial conditions” for the subsequent probe pulse, i.e. for pump incidence at time $t = 0$ and a time delay t_d between the pulses, the free-evolution solutions at $t = t_d$ are taken as the $\bar{\rho}_{ij}^{[0]}$ values ($\bar{\rho}_{ij} = |\bar{i}\rangle\langle\bar{j}|$) for the lock-in detected signal $I_{\text{sig}}^{\text{LI}}$ of Equation 3.38.

The solutions for pump excitation can be obtained in the same manner as in Section 3.1 with $|z+\rangle$ and $|T_z+\rangle$ serving as states $|1\rangle$ and $|2\rangle$, respectively. Here, however, solutions in the FIP are then taken in the limit of $t \rightarrow \infty$ and used as the initial conditions for the free-evolution of the system between pulses. Between pulses, system dynamics are driven by decay and decoherence and thus solutions must in general account for all decay mechanisms, as illustrated in Figure 3.2. The problem can be significantly simplified by utilizing the fact that electron and heavy-hole spin relaxation rates Γ_e and Γ_h are several orders of magnitude slower than the trion relaxation rate Γ_t [115, 124]. As the time delay range covered in experiments is, at most, on the order of the trion relaxation time $T_1^t = 1/\Gamma_t$, the effects of spin relaxation are minuscule. Under these conditions, the two two-level systems can be treated as essentially decoupled, thus we only consider the optically driven transition. Assuming the ability to completely block the pump field after the sample, the lock-in detected signal has the form

$$I_{\text{sig}}^{\text{LI}} = 2\sqrt{\frac{\mu_M}{\epsilon}} Ka(\hbar\omega_0) \left\{ \frac{1}{2} \text{Im} [\bar{\rho}_{14}(t_d)] \sin[\theta_{pr}] + [\bar{\rho}_{44}(t_d) - \bar{\rho}_{11}(t_d)] \sin^2[\theta_{pr}/2] \right\} \quad (3.39)$$

with

$$\begin{aligned} \text{Im}[\bar{\rho}_{14}(t_d)] &= \text{Re}[\bar{\rho}_{14}^{[0]}]\Theta(t_d)e^{-\frac{\Gamma}{2}t_d}\sin(\omega_0 t_d) \\ &+ \left\{ \text{Im}[\bar{\rho}_{14}^{[0]}\cos[\theta_{pu}] + \frac{1}{2}(\bar{\rho}_{44}^{[0]} - \bar{\rho}_{11}^{[0]})\sin[\theta_{pu}]\right\} \Theta(t_d)e^{-\frac{\Gamma}{2}t_d}\cos(\omega_0 t_d) \end{aligned} \quad (3.40)$$

and

$$\begin{aligned} \bar{\rho}_{44}(t_d) - \bar{\rho}_{11}(t_d) &= \\ \Theta(t_d)e^{-\Gamma t_d} &\left\{ \bar{\rho}_{tot} \left(1 - \frac{e^{\Gamma t_d}}{\Theta(t_d)} \right) - 2\text{Im}[\bar{\rho}_{14}^{[0]}\sin[\theta_{pu}] + (\bar{\rho}_{44}^{[0]} - \bar{\rho}_{11}^{[0]})\cos[\theta_{pu}]\right\} \end{aligned} \quad (3.41)$$

where Θ is the Heaviside step function, $\theta_{pu(pr)}$ is the pump (probe) pulse area and we have used the state labeling scheme of Table 2.1. We will in general be considering the case where the QD is in the ground state prior to excitation with the electron spin population equally distributed between the two spin states. The signal then has the form

$$\begin{aligned} I_{\text{sig}}^{\text{LI}} &= 2\sqrt{\frac{\mu M}{\epsilon}}Ka(\hbar\omega_0) \times \\ &\left\{ \sin^2[\theta_{pr}/2] \left[\sin^2[\theta_{pu}/2]\Theta(t_d)e^{-\Gamma t_d} - \frac{1}{2} \right] - \frac{1}{8}\sin[\theta_{pu}]\sin[\theta_{pr}]\Theta(t_d)e^{\frac{\Gamma}{2}t_d}\sin(\omega_0 t_d) \right\} \end{aligned} \quad (3.42)$$

where the first term in the brackets reflects the evolution of the population while the second term reflects the evolution of the coherence.

For a fixed pulse area, the first term in the curly brackets of Equation 3.42 decays exponentially with pulse delay as a result of the decay of pump-generated trion population while for a fixed pulse delay it oscillates as a function of pulse area due to pump-driven Rabi oscillations between $|z+\rangle$ and $|T_z+\rangle$. The second term in the curly brackets also decays as a function of pulse delay (in this case due to trion dephasing) but also oscillates at optical frequencies. Because of this high frequency dependence on the pulse-delay, this term effectively averages out to zero for experiments where the photocurrent signal as a function of pulse delay is averaged for several hours without any active stabilization of the phase between the pump and probe pulse trains, as will be discussed in more detail in the following Chapter. Thus, pump-probe studies

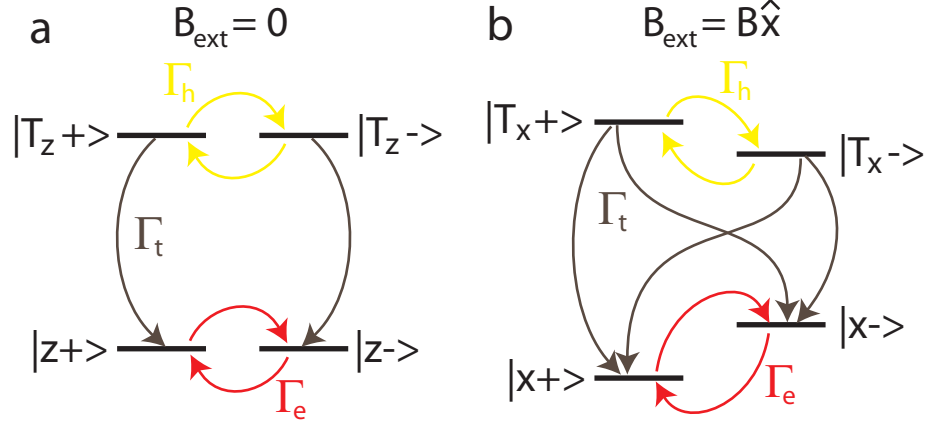


Figure 3.2: Relaxation rates between the QD levels (a) with and (b) without an externally applied magnetic field along \hat{x} . For each case, the trion relaxation rates are assumed to be equal for each decay path and the mutual relaxation rates between the spins are taken to be the same.

are used primarily to investigate the “population” term of Equation 3.42 and, in the case of studies without a magnetic field, are used to observe trion decay and trion Rabi oscillations.

3.5 Pump-Probe Studies: $\mathbf{B}_{\text{ext}} = B\hat{x}$

Pump-probe studies with a magnetic field applied along \hat{x} provide a means of observing the precession of QD spins. In this case, stationary states are defined in the \hat{x} basis and are linear combinations of the states defined in the \hat{z} basis. For electron and heavy-hole spin vectors of the form

$$\mathbf{s}_{e,h} = \hat{x}\langle s_x \rangle_{e,h} + \hat{y}\langle s_y \rangle_{e,h} + \hat{z}\langle s_z \rangle_{e,h} \quad (3.43)$$

with

$$s_x = \frac{\hbar}{2} \begin{bmatrix} 0 & 1 \\ 1 & 0 \end{bmatrix}, \quad s_y = \frac{\hbar}{2} \begin{bmatrix} 0 & -i \\ i & 0 \end{bmatrix}, \quad s_z = \frac{\hbar}{2} \begin{bmatrix} 1 & 0 \\ 0 & -1 \end{bmatrix}, \quad (3.44)$$

excitation of either transition in the dot by a $\hat{\sigma}_{\pm}$ polarized pump pulse generates spin vectors for the electron and heavy-hole that are oppositely oriented along the optical axis \hat{z} . As a result of the magnetic field, these spin vectors then precess about \hat{x} (Figure 3.3). Equivalently, this precession represents the time-evolution of coherence

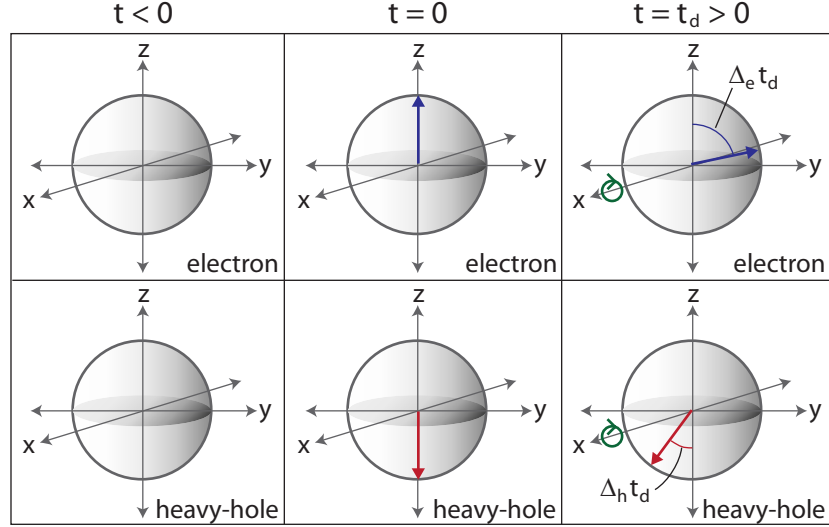


Figure 3.3: Spin Bloch spheres in real space showing the time-evolution of the electron and heavy-hole spin vectors for a resonant $\hat{\sigma}_-$ polarized pulse incident at time $t = 0$. Prior to excitation ($t < 0$), the electron and heavy-hole spins are unpolarized. At $t = 0$ the $\hat{\sigma}_-$ polarized pulse generates $|T_z+\rangle$ population, creating electron and heavy-hole spin vectors that are oppositely aligned along \hat{z} . These spin vectors precess about the \hat{x} axis at rates determined by the Zeeman splittings for the two spins.

generated between the spin states of the electron and the heavy-hole in the \hat{x} basis by the pump pulse via stimulated two-photon Raman processes [202, 203]. It is these same two-photon Raman processes that will be used to coherently control the spin of the resident electron in Chapters 5 and 6.

Spin vectors generated by the pump pulse precess about the magnetic field at frequencies determined by the respective Zeeman splittings of the electron and the heavy-hole spins, which depend on the magnitude of the external magnetic field and the electron and heavy-hole in-plane g-factors. During precession, the spin vectors decay in magnitude due to dephasing and relaxation processes in the dot. For the electron, the timescale for the decay of the spin vector magnitude is determined by the spin coherence time T_2^{e*} , where the asterisk indicates the inhomogeneous broadening of the coherence time due to fluctuations in the hyperfine nuclear field. For the heavy-hole, the timescale for decay is determined by both the heavy-hole spin coherence time T_2^{h*} and the trion relaxation time T_1^t , as trion decay also destroys heavy-hole spin coherence. In pump-probe studies, we then expect that in probing with either a

$\hat{\sigma}_+$ or a $\hat{\sigma}_-$ polarized probe the lock-in detected signal will consist of two oscillating components decaying at different rates.

To determine the mathematical form of the lock-in detected signal we consider the case of circularly cross-polarized pump and probe pulses resonant with the \hat{z} basis transitions. Excitation by the $\hat{\sigma}_+$ pump pulse incident at $t = 0$ is handled the same way as in the previous section. For the free-evolution of the system between pulses, however, all four of the \hat{z} basis density matrix elements immediately after the pump pulse are transformed to the \hat{x} basis using the transformations given in Appendix B. The \hat{x} basis density matrix elements evolve for a time duration t_d and are then transformed back into the \hat{z} basis. Homodyne detection of the $\hat{\sigma}_-$ probe pulse leads to the lock-in detected photocurrent

$$I_{\text{sig}}^{\text{LI}} \approx 2\sqrt{\frac{\mu_M}{\epsilon}} K a(\hbar\omega_0) \sin^2[\theta_{pr}/2] \times \left\{ \frac{1}{4} \sin^2[\theta_{pu}/2] \Theta(t_d) \left[2e^{-2\Gamma t_d} - e^{-t_d/T_2^{e*}} \cos(\Delta_e t_d) - e^{-2\Gamma t_d} e^{-t_d/T_2^{h*}} \cos(\Delta_h t_d) \right] - \frac{1}{2} \right\} \quad (3.45)$$

where we have already made use of the fact that the ‘‘coherence’’ term of the signal averages to zero due to the high number of averages taken in experiments without optical phase stabilization between the pump and probe beams. We see that, indeed, the signal possesses two decaying oscillation components in addition to a DC component (due to the initial population difference between the electron and trion states prior to pump excitation). Thus, lock-in detected photocurrent measurements in principle enable the determination of the g-factors and the coherence times for the electron and the heavy-hole.

3.6 Chapter Summary

The theoretical foundation for pulsed optical measurements of a single InAs QD were presented. Phase sensitive detection of the interference between the excitation pulse and the field radiated by the optically induced polarization in the dot was established as the basis of time-resolved studies of single QDs. This method of detec-

tion was applied to pump-probe studies of a single QD with and without an external magnetic field, showing that phenomena such as trion decay, trion Rabi oscillations, spin precession and spin dephasing can in principle be observed. Experimental results employing this method of detection are presented in the following Chapter.

CHAPTER 4

Control and Read-Out of a Single InAs QD with Picosecond Optical Pulses: Experimental Setup and Results

The ability to perform time-resolved optical studies of a single self-assembled QD with ultrafast optical pulses would provide a powerful tool for studying transient phenomena at the single-dot level. Until recently, such studies had been elusive in self-assembled QDs due to the difficulty imposed by the small optical dipole moments of self-assembled QDs. In the homodyne measurements presented in the previous Chapter, these small dipole moments necessitate the ability to detect the small field radiated by the QD optical polarization on top of a large intensity background. When compared to pulsed optical studies of single interface fluctuation QDs [107, 119, 130, 139, 204, 205], the intensity backgrounds encountered in single self-assembled QD studies are roughly two orders of magnitude larger due to the order of magnitude difference between the dipole moments of the two types of dots [194]. As a result, single self-assembled QD measurements with ultrafast optical pulses require particularly low-noise experimental conditions.

In this Chapter, we present the general experimental setup and procedure employed for single self-assembled QD studies, culminating in the discussion of the experimental results from one- and two-pulse studies of a single InAs QD. The characterization process for single QDs is first presented, starting with a discussion of the PL signal from a single quantum dot by which QD charge states are identified. Absorption studies with a narrow-bandwidth continuous-wave (CW) optical source are then performed to characterize the energy range in which a particular QD charge

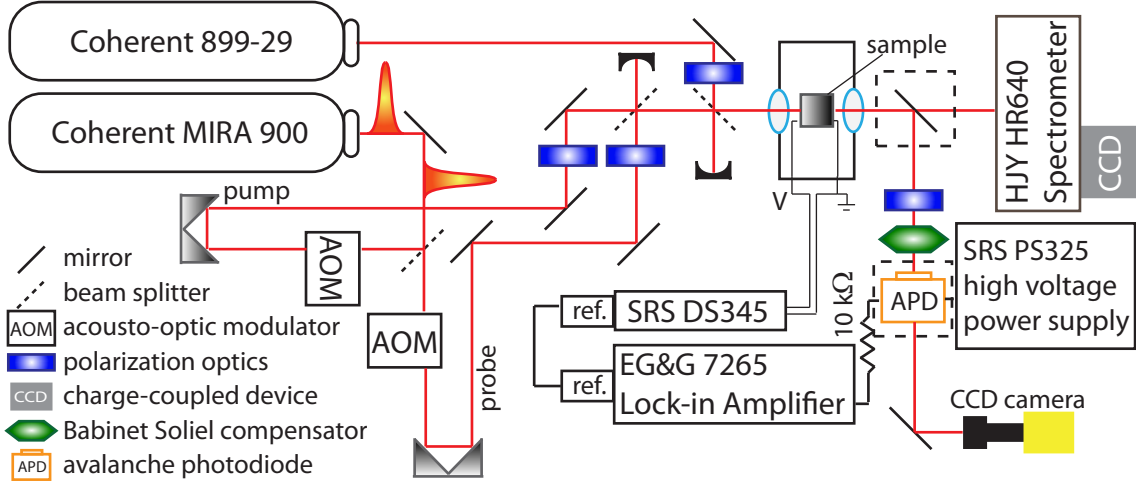


Figure 4.1: The experimental setup used in all studies, where components surrounded in dashed boxes are on removable mounts. Optical pulses and CW fields are provided by the Coherent MIRA 900 and the Coherent 899-29, respectively, both pumped by separate Coherent Verdi-V10 solid state lasers (not pictured). A Janis Research Company superconducting magneto cryostat keeps the sample at liquid helium temperatures and is used to provide DC magnetic fields ranging from 0 to 6.6 T in strength. The sample is imaged using a CCD camera on the collection side of the sample. For PL spectroscopy studies, a Horiba Jobin-Yvon HR640 spectrometer is used along with a Princeton Instruments liquid nitrogen cooled CCD. For pulsed and CW absorption studies, measurements are taken using a Hamamatsu S8890-15 Si avalanche photodiode module. The photocurrent output is converted to a voltage with a 10 k Ω resistor and is then read by an EG&G 7265 lock-in amplifier. Both the reference signal and the sample bias signal are provided by a Stanford Research Systems DS345 signal generator.

state optically absorbs. Absorption studies with a single train of optical pulses are then performed to demonstrate the ability to read-out a single QD with optical pulses. These pulsed optical measurements are then implemented in two-pulse studies both with and without an external magnetic field applied perpendicular to the growth axis. Results from two-pulse studies are used to extract parameters such as the trion dipole moment, the trion lifetime and the g-factors of the electron and the heavy-hole. Two-pulse studies with a magnetic field, though in principle able to determine the T_2^* values for the electron and the heavy-hole, are severely limited by the high number of averages required to achieve sufficient measurement SNR. This limits the range of time-delays that can be considered in experiments and thus prevents reliable

extraction of the spin T_2^* values. These studies are still, however, able to provide an estimation of the lower-bound of the spin coherence times in a single self-assembled QD.

4.1 Experimental Setup

The experimental setup used for all experiments presented in this thesis is given in Fig. 4.1. This is a dynamic setup that enables frequency and time-domain studies of single QDs, as well as studies simultaneously employing both optical pulses and narrow bandwidth optical fields. We now discuss the various components of this setup and their properties.

4.1.1 Optical Sources

A Coherent MIRA 900 Ti:Sapph laser is used as the pulsed optical source and can be switched between picosecond or femtosecond operation depending on whether a GVD compensating prism pair is installed. The MIRA 900 also has the option of operating in CW mode, though the optical output in this mode is not frequency stabilized. In picosecond mode, the MIRA 900 provides mode-locked pulses 1-3 ps in width (depending on the exit slit size) at a rate of 76 MHz (13.2 ns repetition period) that can be tuned between 700 nm and 1 μm . With the prism pair installed the MIRA 900 can operate in femtosecond mode, producing pulses of < 200 fs in pulse width with the same repetition rate and tunability as in picosecond mode. For all experiments performed in this work, the MIRA 900 is operated in picosecond mode. Fig. 4.2 shows the autocorrelation trace and pulse spectrum of the MIRA 900 pulses employed in experiments.

Frequency-locked narrow-bandwidth CW fields are provided by a Coherent 899-29 Ti:Sapph laser. This laser is capable of generating tunable, actively stabilized optical output with a bandwidth of < 500 kHz. The 899-29 employed in experiments can be tuned roughly between 900 nm and 980 nm and is used in CW absorption studies of single QD states.

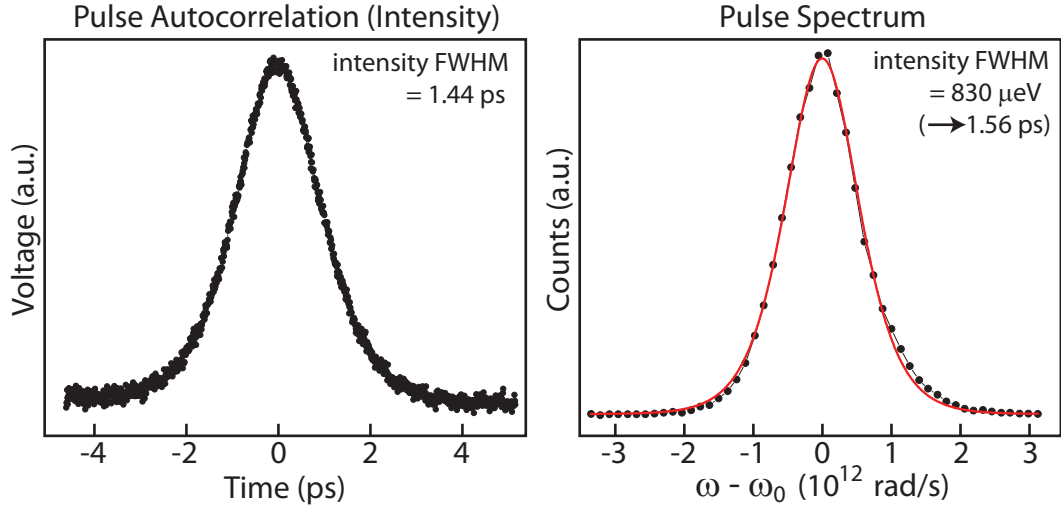


Figure 4.2: Intensity autocorrelation trace (left) and optical spectrum (right) of the MIRA 900 pulses produced in picosecond mode for a particular exit slit width. Autocorrelation traces are taken with an Inrad model 5-14A autocorrelator that measures the intensity autocorrelation signal. The pulse spectrum was measured using the HR640 with the liquid nitrogen cooled CCD camera and fit to a squared hyperbolic secant function (red curve).

4.1.2 Cryostat

In all experiments, the sample is kept at liquid helium temperatures around 5 K both to prevent thermal excitation of excited states in the dot and to reduce the contribution of acoustic phonons to QD state relaxation and dephasing. In addition, some studies require the sample to be placed in a large external DC magnetic field. Both of these functions are performed by a Janis Research Company superconducting magneto cryostat capable of maintaining liquid helium temperatures and sustaining DC magnetic fields of up to ~ 7 T, which can be applied along or perpendicular to the sample growth axis. Sealed windows on the cryostat allow transmission studies for optical excitation along two orthogonal axes. In addition, the cryostat is equipped with interfacing ports that enable the connection of external signal generators with the sample bias terminals.

4.1.3 PL Spectroscopy Setup

For PL spectroscopy we use a Horiba Jobin-Yvon (HJY) HR640 spectrometer

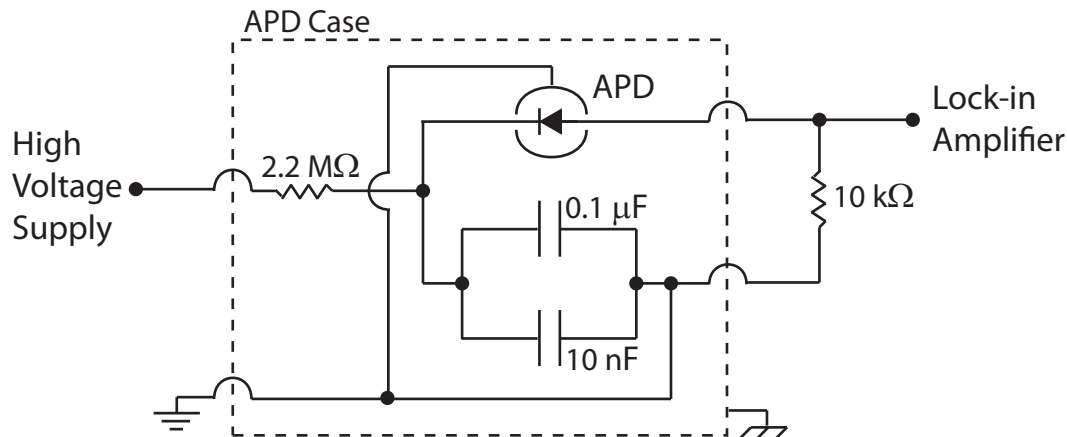


Figure 4.3: APD circuit diagram.

possessing a 11×11 grating blazed at $1 \text{ }\mu\text{m}$ with 600 grooves/mm. At wavelengths around 950 nm the HR640 has the practical resolving power—based on the Rayleigh criterion—to distinguish spectral lines of equal intensity with energy separations as small as $44 \text{ }\mu\text{eV}$. The detector used with the HR640 is a Princeton Instruments liquid nitrogen cooled CCD camera with a CCD chip consisting of a 256×1024 grid of $26 \text{ }\mu\text{m} \times 26 \text{ }\mu\text{m}$ pixels.

4.1.4 Phase Sensitive Detection Setup

For the phase sensitive measurements discussed in the previous Chapter, we use a setup consisting of a Hamamatsu S8890-15 Si avalanche photodiode (APD), a Stanford Research Systems (SRS) PS325 high voltage power supply, a SRS DS345 signal generator and an EG&G 7265 digital lock-in amplifier. The DS345 provides an AC voltage signal at a particular frequency across the voltage terminals of the sample that serves to modulate the properties of the QD under study. This modulation in turn modulates the properties of the optical fields transmitted through the sample at the same frequency. This transmitted light is focused onto the active area of the Si APD, which serves to convert the transmitted field intensities to a current output. A circuit diagram for the APD used in experiments is given in Fig. 4.3. The voltage drop induced by the APD photocurrent across a $10 \text{ k}\Omega$ resistor is measured by the lock-in amplifier, which isolates the component of the measured voltage modulated

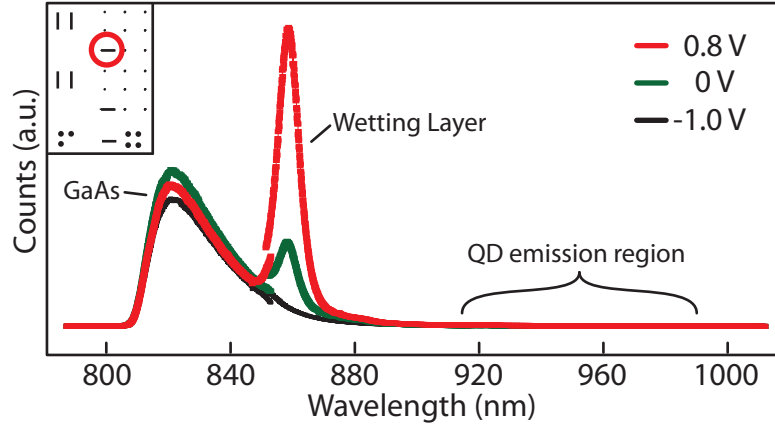


Figure 4.4: PL spectra as a function of emission wavelength for sample R060913G at different sample bias voltages. The PL spectra show emission from different sample layers for CW excitation at 780 nm through the aperture indicated in the upper-left inset. The general range of QD emission wavelengths is also indicated, though QD emission lines are too weak to be observed on these scales.

at the sample modulation frequency.

4.2 QD Characterization with PL Spectroscopy

In PL studies, the MIRA 900 is operated in CW mode and tuned to 780 nm. At this wavelength, the MIRA 900 serves to generate electron-hole pairs in the various layers of the sample that then recombine and emit photons whose energies depend on the layer properties. By measuring this emitted light with the HR 640 we can detect the emission intensity (CCD counts per pixel) as a function of emission wavelength or energy.

In general, the sample is first characterized in PL studies before individual QD states are characterized. Figure 4.4 shows the sample emission spectra for sample R060913G at different external bias voltages. Of key importance is the lack of an ensemble emission signal covering the range of QD state emission energies. This type of ensemble emission signal has been observed in similar samples studied in our lab and is believed to be a result of the migration of Te into the sample layers near the QDs (as discussed previously in Section 2.1). The presence of this ensemble of states covering the QD transition energy range generally interferes with time-domain

optical studies of single dots as these ensemble states also absorb, making it difficult to distinguish the QD signal.

Once the sample emission has been characterized, single QD spectra are obtained. These spectra are obtained in the same manner as the sample spectra, as some of the electron-hole pairs generated by the 780 nm CW field in the GaAs layers and the WL relax into the QDs, where they recombine and emit photons whose energies correspond to QD energy levels. PL “maps” are given in Figures 4.5(a) and (b), showing the emission intensity from individual QD states as a function of energy and sample bias. Charge transitions in two separate dots are shown in Figure 4.5(a) with both dots switching from containing no charges to containing a single electron around a sample bias of -0.5 V. The roughly 5 meV shift in emission energies is characteristic in these samples and indicates the difference in binding energies between the neutral exciton and the trion. The yellow boxes in Figure 4.5(a) indicate the emission lines associated with the dot that is the focus of studies in this thesis, referred to as QD #1. The other dot in this aperture, QD #2, will be shown to play a role in time-domain studies of QD #1 later in this Chapter. Figure 4.5(b) plots the emission of the two trion states from Figure 4.5(a) for an extended range of voltages, showing no additional charge states as the bias is increased.

Once a particular QD has been characterized in PL, the next step in QD state characterization is CW Stark-shift modulation absorption spectroscopy [206], a technique that measures the absorption spectrum of a particular state of interest. The details of this experimental method are discussed in the following section.

4.3 CW Stark-Shift Modulation Absorption Spectroscopy

CW Stark-shift modulation absorption spectroscopy is an experimental method that allows for the measurement of single QD absorption spectra using phase sensitive techniques. This method relies on DC Stark shifting the QD transition energies to modulate the absorption of a narrow-bandwidth CW field tuned in energy near one of the QD transitions. At a particular sample bias voltage V_{DC} the absorption \mathcal{A} of

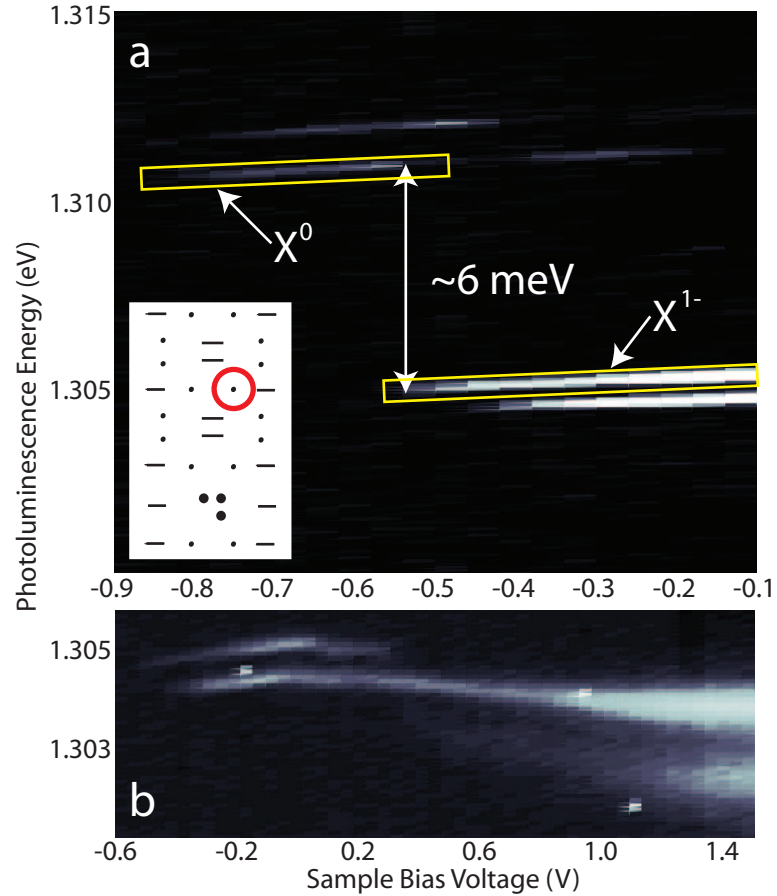


Figure 4.5: Emission spectra of aperture Dp2(9) [circled in the inset of (a)] as a function of applied sample bias and emission energy for two different energy/bias ranges. (a) Emission spectrum showing charge transitions for QD #1 and QD #2 in the -0.6 V to -0.4 V range. The lines surrounded by the yellow boxes indicate the states of QD #1, the primary dot studied in this thesis. The emission of QD #1 switches from containing no charges (X^0) to containing a single electron (X^{1-}) when the sample bias is increased above -0.55 V . The slight positive sloping of the emission lines is a result of the DC Stark shift, which blue-shifts each emission line as the bias voltage is increased. (b) The extended spectrum of the trion emission lines for QD #1 and QD #2, showing that trion emission covers a long voltage range with the peaks broadening considerably as the sample voltage is increased.

the CW field has the form

$$\mathcal{A} = \frac{\alpha_0 \gamma^2}{(V_{\text{DC}} - V_0)^2 + \gamma^2} \quad (4.1)$$

where V_0 is the voltage at which the QD transition is exactly resonant with the CW field, γ is the QD transition dephasing rate and α_0 is the CW field absorption on-resonance, which is taken to be $\ll 1$ [207]. In principle, this absorption can be detected directly by measuring the transmitted CW field on a square-law detector as a function of V_{DC} . However, given the weak scattering of the incident light by individual self-assembled QDs, this direct approach generally requires the use of solid immersion lenses (SILs) and numerical aperture increasing lenses (NAILs) that improve the coupling of the QD to the excitation light and the collection efficiency to attain a sufficiently high signal-to-noise ratio (SNR) [208].

The use of phase sensitive techniques provides a means of achieving the requisite SNR for single self-assembled QD absorption measurements without the use of SILs or NAILs. In this case, a square wave modulation is applied to the sample bias voltage such that the total voltage across the sample $V(t)$ has the form $V(t) = V_{\text{DC}} + V_{\text{AC}} \cdot \text{SW}(t)$ where V_{AC} is the amplitude of the square-wave component, $\text{SW}(t)$, of the total sample voltage. Modulation of the sample bias leads to modulation of the absorption \mathcal{A} of the CW field tuned near the QD transition, where the amplitude of the absorption modulation, \mathcal{A}_{mod} , is

$$\mathcal{A}_{\text{mod}} = \left| \frac{\alpha_0 \gamma^2}{(V_{\text{DC}} + \frac{1}{2}V_{\text{AC}} - V_0)^2 + \gamma^2} - \frac{\alpha_0 \gamma^2}{(V_{\text{DC}} - \frac{1}{2}V_{\text{AC}} - V_0)^2 + \gamma^2} \right|. \quad (4.2)$$

This modulation of the absorption leads to a modulation of the transmitted CW field amplitude and, in turn, a modulation of the photocurrent generated by the transmitted CW field on the APD. The voltage generated by this current across a $10 \text{ k}\Omega$ is measured by the lock-in amplifier, which is synchronized to the signal generator by an external reference signal provided by the signal generator. The lock-in amplifier amplifies the input voltage signal, digitizes it and then multiplies it separately by digital $\sin(\omega_{\text{ref}}t + \phi_{\text{ref}})$ and $\cos(\omega_{\text{ref}}t + \phi_{\text{ref}})$ functions, where ω_{ref} is the sample bias modulation frequency and ϕ_{ref} is the internal phase of the lock-in amplifier. These

two products are then passed through a series of digital low-pass filters, the outputs serving as the “X” and “Y” channel signals. These outputs thus correspond to a narrow portion of the Fourier spectrum of the digitized input voltage signal centered at the reference frequency ω_{ref} , the width and fall-off of this distribution determined by the lock-in time constant and the number of digital low pass filters employed, respectively.

Figure 4.6 provides a detailed depiction of the CW Stark-shift modulation absorption spectroscopy technique, illustrating the form of the lock-in detected X-channel for two different V_{AC} values at $\phi_{\text{ref}} = 0$. For values of V_{AC} much smaller than the absorption linewidth (in voltage), the lock-in X-channel signal as a function of V_{DC} effectively gives the first derivative of the absorption profile [orange curve in Figure 4.6(e)]. Increasing the value of V_{AC} beyond the absorption linewidth separates the signal into identical positive and negative peaks, each giving the absorption profile of the state [light blue curve in Figure 4.6(e)]. We note that CW Stark shift modulation absorption spectroscopy may also be performed by keeping the values of V_{DC} and V_{AC} fixed and scanning the frequency of the CW field, yielding the same types signals for small and large voltage modulation as a function of laser frequency.

An absorption spectrum for the trion of QD #1 is given in Figure 4.7, where the lock-in detected modulated absorption signal is plotted as a function of the Coherent 899-29 laser energy at different values of V_{DC} for a small sample modulation amplitude. Trion absorption occurs for V_{DC} values in the range of 0.6 V to 2.4 V, showing the expected anti-symmetric trace for V_{DC} values away from the extremes of the absorption range. At the extreme points of the absorption range, the shape of the absorption profile deteriorates due to the instability of the QD charge state at those voltage points. In the stable voltage range of the charged QD, the DC Stark effect is linear, as shown in the lower-right inset of Figure 4.7.

Compared to the emission spectrum [Figure 4.5(b)], the absorption spectrum of the trion of QD #1 covers a much more limited voltage range. Discrepancies such as these between the emission and absorption spectra are commonly encountered in QD studies and arise from differences in the physical processes involved in the two

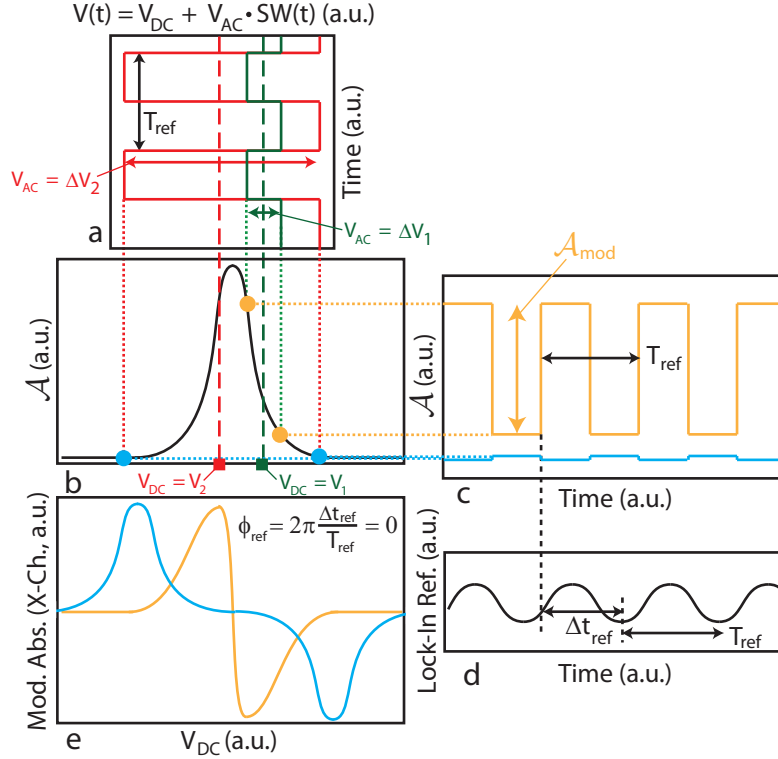


Figure 4.6: The CW Stark-shift modulation absorption spectroscopy method. (a) Sample bias voltage $V(t)$ as a function of time for small (green curve) and large (red curve) values of V_{AC} . (b) Theoretical absorption profile of an optical transition in a single QD (black curve), where \mathcal{A} is plotted as a function of V_{DC} without voltage modulation. The vertical dotted lines indicate points on the absorption profile corresponding to the sample bias voltage values. The dashed vertical lines indicate the value of V_{DC} for each particular voltage configuration. (c) The absorption \mathcal{A} as a function of time for the small (orange) and large (light blue) modulations. The modulation of the absorption signal is a result of the modulated sample bias and occurs at the same frequency. (d) The lock-in reference signal as a function of time. The reference signal oscillates at the same frequency as $V(t)$ as the lock-in external reference is provided by the signal generator driving the sample bias. The phase difference between the lock-in and the signal generator, $\phi_{ref} = 2\pi \frac{\Delta t_{ref}}{T_{ref}}$, can be controlled and determines the X and Y channel signals of the lock-in. (e) Simulated X channel signals as a function of V_{DC} for the two different values of V_{AC} at $\phi_{ref} = 0$. The smaller value of V_{AC} (orange curve) leads to a signal that resembles the derivative of the absorption lineshape while the larger value (light blue curve) leads to a positive and negative peak separated by the value of V_{AC} , each reflecting the absorption lineshape of the transition.

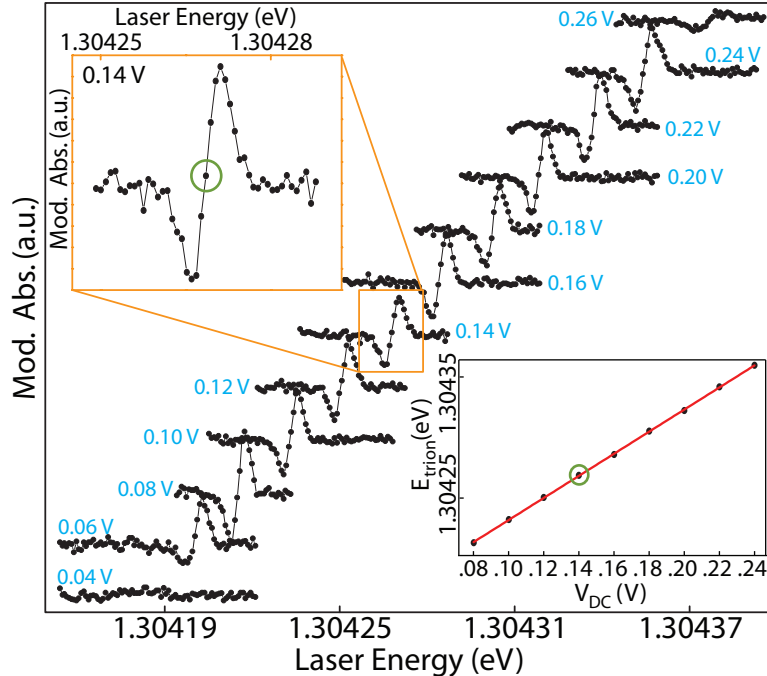


Figure 4.7: Absorption spectrum of the trion of QD #1, where the lock-in phase ϕ_{ref} is set such that the modulated absorption signal is entirely in the X channel. Each absorption trace is obtained by scanning the energy of the Coherent 899-29 through the trion transition energy at different values of V_{DC} (light blue voltage values) for a V_{AC} value of 0.02 V. The upper-left inset shows the spectrum obtained at $V_{\text{DC}} = 0.14$ V. The lower-right inset plots the zero-crossing energy (green circle in the upper-left inset) as a function of V_{DC} , exhibiting the linearity of the Stark shift.

types of spectroscopy. PL spectroscopy generally involves the generation of many electron-hole pairs in the GaAs layers and the WL of the sample that can shift the transition energy of the QD and affect its charging properties. This is in stark contrast to absorption studies, in which electron-hole pairs are generated directly in the dot. The lack of the additional carriers present in PL studies can lead to differences in the measured transition energies and in the observed charging characteristics.

Determination of the absorption range of the trion in voltage and excitation energy is crucial for time-domain studies of a singly charged self-assembled QD. In the following section, we discuss how knowledge of the trion absorption range obtained in CW studies is used to successfully demonstrate pulsed optical read-out of a single InAs QD.

4.4 Pulsed Stark-Shift Modulation Absorption Spectroscopy

The ability to perform pulsed optical read-out of single InAs QDs using a single train of optical pulses is crucial for time-resolved studies of transient QD phenomena. As mentioned previously, homodyne measurements of single self-assembled QDs with optical pulses are non-trivial due to the relatively small signal strengths compared to the large backgrounds from which these signals must be extracted. Pulsed optical measurements of single interface fluctuation QDs previously performed in this laboratory [107, 139, 204, 205] have typically relied on amplitude modulation of the pump and probe beams (the so-called “double-chopping” scheme), resulting in a lock-in detected signal proportional to third and higher order terms of the QD optical response. Lack of sensitivity to the first order response poses a significant challenge in applying this method successfully to studies of single self-assembled QDs.

Due to these challenges, we have developed a new approach to performing pulsed optical measurements of single QDs that is sensitive to the first order optical response of the dot. This approach is the pulsed analogue of the CW Stark-shift modulation absorption technique presented in the previous section. In this approach, the optical pulses are centered in energy on the trion absorption range determined in the CW modulated absorption studies of Figure 4.7. In addition, the sample bias is modulated between two values, V_L and V_R , where V_L sets the QD to a state that does not interact with the incident light and V_R lies within the absorption range of the trion. Modulation of the sample bias voltage between these two values serves to effectively switch off and on the optical interaction of the dot with the incident pulses. Figure 4.8 illustrates the basic scheme of the pulsed Stark-shift modulation absorption spectroscopy technique.

As discussed in Section 3.3, an optical pulse resonantly tuned to a single transition in the QD generates an optical polarization within the dot that radiates a field. Modulation of the sample bias voltage between V_L and V_R effectively modulates the optically generated polarization in the dot and, thus, the amplitude of the radiated field. It is this modulation that leads to the lock-in detected photocurrent terms of Equation 3.38.

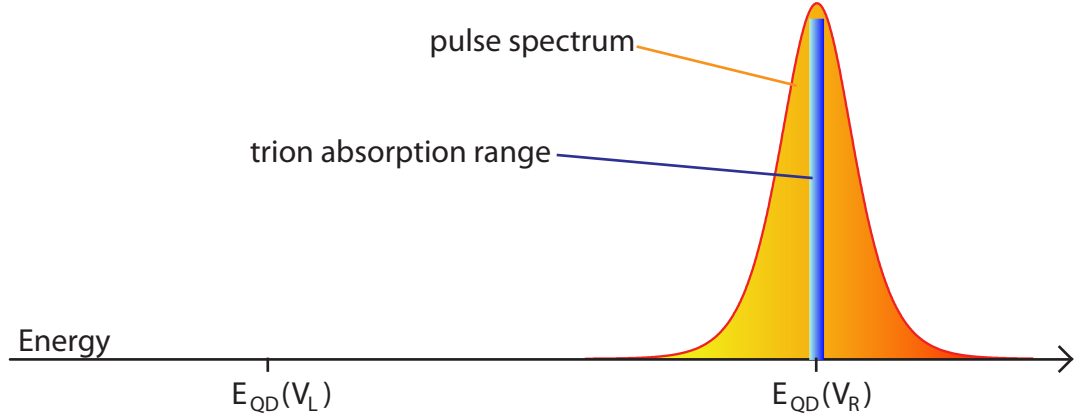


Figure 4.8: Arrangement of the QD energies (E_{QD}), pulse spectrum and trion absorption range in pulsed optical measurements of the trion state in a singly charged InAs QD.

In experiments, we consider the operation of an incident train of \hat{x} or \hat{y} polarized pulses. In this case, both two-level systems in the dot are excited equally, resulting in a total QD polarization consisting of contributions from each two-level system. These contributions generate a total radiated field that is linearly polarized and whose amplitude is proportional to the amplitude of the field radiated by one of the two-level systems. As the electron spin in the dot at zero magnetic field is taken to be in a completely mixed state prior to excitation, the component of the photocurrent detected by the lock-in amplifier has the form

$$I_{\text{sig}}^{\text{LI}} = -\sqrt{\frac{2\mu_M}{\epsilon}} K a(\hbar\omega_0) \sin^2[\theta(\infty)/2], \quad (4.3)$$

where we see that the signal oscillates as a function of the pulse area $\theta(\infty)$. These oscillations are the so-called Rabi oscillations that are driven between the electron spin state and the trion state by the optical pulses and can be observed by performing power dependent studies. We note that because of the low maximum input current limit imposed by the EG&G in current mode operation, we instead detect the modulated components of the voltage generated by the APD photocurrent across a 10 k Ω shunting resistor, V_{sig} , which is proportional to $I_{\text{sig}}^{\text{LI}}$.

Figure 4.9 shows time-averaged measurements of V_{sig} (X channel) for a single incident pulse train as a function of V_{R} at an average power of 500 μW with $V_{\text{L}} = -1$ V. A pronounced dip in the V_{R} scan occurs in the 0.1 V to 0.35 V range of V_{R} due to

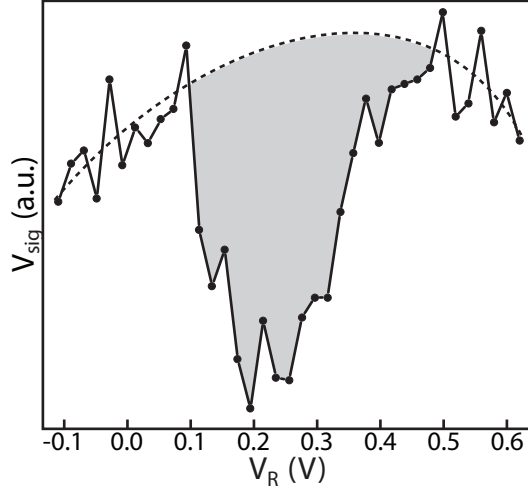


Figure 4.9: Time averaged V_{sig} measurements (X channel) as a function of V_{R} for the trion of QD #1 using a single pulse train of $500 \mu\text{W}$ average power with $V_{\text{L}} = -1 \text{ V}$. The dip is the result of the detection of the field radiated by the QD and is shaded to indicate the difference between the background signal level (black dashed line) and the QD signal.

the detection of the field radiated by the QD. This voltage range is consistent with the voltage range in CW absorption studies of the trion, albeit slightly longer. In addition to the dip in V_{sig} , an overall background signal is apparent in the data of Figure 4.9, the level of which is estimated by the black dashed line. This background signal is attributed to the ensemble of states provided by migrated Te, as it is much larger in other samples characterized in our laboratory that show a more pronounced ensemble emission spectrum in the QD energy range (data not shown). The difference between this background level and the QD signal is given roughly by the grey shaded area of the figure.

V_{sig} measurements as a function of V_{R} at several different average pulse powers are plotted in Figure 4.10, showing an oscillation in the difference between the background signal and the QD signal as the average pulse power is increased. This oscillation reflects a complete Rabi oscillation between the electron spin state and the trion state in each two-level system in the dot. This result demonstrates the ability not only to perform pulsed optical read-out of a single self-assembled QD but also to coherently control the electron-trion transition with optical pulses, a crucial step towards coherent optical control of the electron spin in the dot. In the following

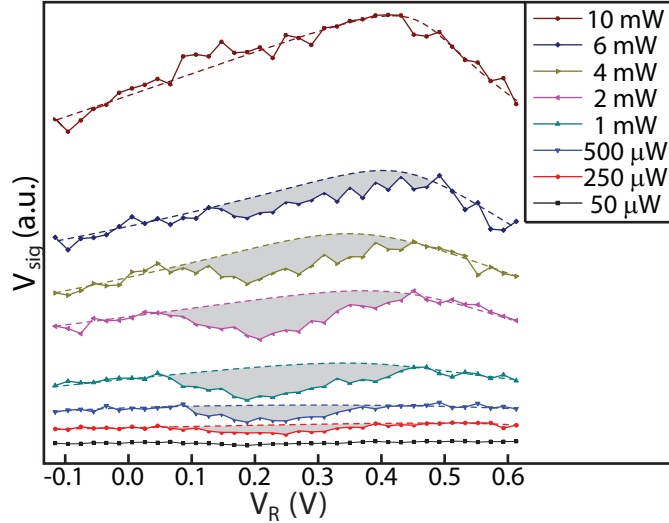


Figure 4.10: V_R scans of the trion in QD #1 at different average pulse powers for $V_L = -1$ V. The difference between the background signal level and the QD signal level (shaded gray areas) undergoes a complete oscillation as the average pulse power is increased, indicating a complete Rabi oscillation between the electron and trion states in the dot. The dependence of the background signal level on the average pulse power is also shown.

sections, these results are built upon in pump-probe studies employing two time-delayed pulse trains and are used to demonstrate time-resolved measurements of transient QD phenomena.

4.5 Pump-Probe Studies with $B_{\text{ext}} = 0$: Trion Decay and Trion Rabi Oscillations

By introducing an additional time-delayed pulse train in the experimental setup, V_{sig} measurements may also be used to monitor the time-evolution of QD phenomena. For pump-probe studies at zero magnetic field, the probe-generated V_{sig} signal can be used to observe the excitation and decay of trion population generated by the preceding pump pulse, as well as Rabi oscillations between the electron spin states and the trion states in the QD.

In these studies, V_L is set to -1 V and V_R is set to the center of the dip in Figure 4.9. The pump and probe fields are linearly cross polarized to enable post sample filtering of the pump using a Babinet-Soliel compensator with a polarizer so

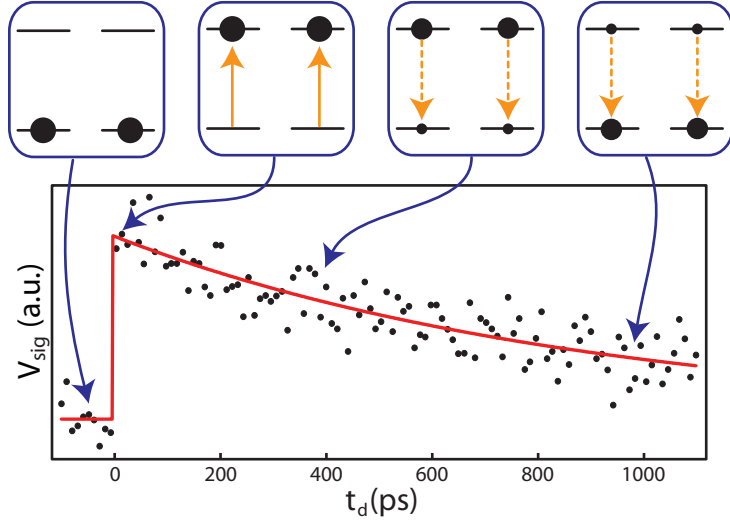


Figure 4.11: Time-averaged V_{sig} measurements as a function of pulse delay t_d showing the generation and exponential decay of pump-generated trion population, as indicated by the energy level diagrams given above the graph. A fit of the data to Equation 4.4 is given by the red curve, which yields a trion relaxation time of 855 ± 74 ps.

that only the probe is detected by the APD. The time delay t_d between the pump and probe pulse trains is scanned over a specified range and V_{sig} measurements are averaged over the course of several hours to obtain sufficiently high SNR. Since the pump and probe pulse trains traverse separate paths of approximately 5 m before reaching the sample, the lack of active phase stabilization between the two pulse trains results in the averaging out of the second term of Equation 3.42 in these studies. This is due primarily to air currents and laboratory temperature instabilities that can result in fluctuations in the path difference between the pump and probe beams of up to a few optical wavelengths. In order to compensate for these fluctuations in the path difference, feedback-stabilized Michelson interferometer setups are generally implemented, where one of the legs is mounted on an actively controlled piezoelectric translation stage (see, for instance, Reference [139]). Without such a setup, the lock-in detected voltage is proportional to the “population” term in Equation 3.42 and thus has the form

$$V_{\text{sig}} = M \sin^2[\theta_{pr}/2] \left[\sin^2[\theta_{pu}/2] \Theta(t_d) e^{-\Gamma t_d} - \frac{1}{2} \right] \quad (4.4)$$

where M is the proportionality constant relating $I_{\text{sig}}^{\text{LI}}$ to V_{sig} . V_{sig} measurements as

a function of pulse delay are plotted in Figure 4.11 for pump and probe powers corresponding roughly to a π -pulse and a $\pi/3$ -pulse, respectively, for each transition in the dot, clearly showing the generation of trion population at $t_d = 0$ and its subsequent decay. By fitting the data of Figure 4.11 to Equation 4.4, a trion relaxation time T_1^t of 855 ± 74 ps is extracted, consistent with values reported in separate trion linewidth measurements of similar dots [128].

As the amplitude of the exponentially decaying term in Equation 4.4 depends on both pump and probe pulse areas, measurements of V_{sig} at a fixed positive delay as a function of either pulse area will show oscillations due to optically driven Rabi oscillations between the electron and trion states. Though such oscillations were already observed as a function of pulse area in the one-pulse studies of the previous section, two-pulse studies allow for a more straightforward analysis of the Rabi oscillations. Here, we consider pump-driven Rabi oscillations and note the need to account for a pump pulse area dependent offset in delay scan measurements of V_{sig} arising from pump leakage through the post-sample filtering setup. To account for the pump-dependent background, we take the difference between V_{sig} measurements at a positive pulse delay and a negative pulse delay, i.e. $V_{\text{sig}}(t_d = t_-) - V_{\text{sig}}(t_d = t_+)$ where $t_{+(-)}$ is a positive (negative) value of the pulse delay, as a function of pump pulse amplitude. Figure 4.12(a) plots these difference measurements as a function of the pump amplitude E_{pu} for $t_- = -t_+ = -50$ ps. Two complete oscillations are shown with an oscillatory fit (red curve) yielding a trion dipole moment of approximately 8 Debye, consistent with one-pulse studies.

In addition to the two complete Rabi oscillations observed in Figure 4.12, a higher frequency oscillation is apparent in the data that is most pronounced at the peaks of the primary oscillations, showing up as slight “dimples.” This feature in the data is repeatable and is believed to be the result of the optical pulses off-resonantly exciting the trion of QD #2 in this aperture. To strengthen this claim, numerical calculations of the modulated photocurrent were performed that include the energy levels of QD #2. In these calculations, a trion dipole moment of ~ 16 D is assumed. Theoretical calculations under these conditions are plotted in Figure 4.12(b), exhibiting the same

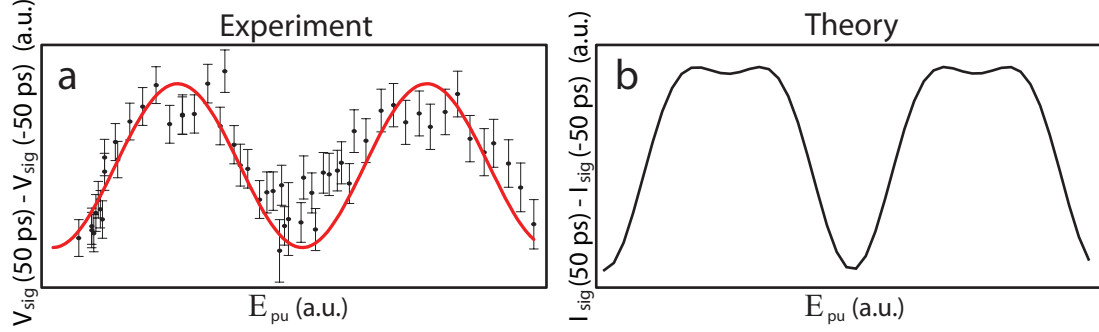


Figure 4.12: (a) Experimentally measured V_{sig} values as a function of pump pulse area E_{pu} showing two complete pump-driven Rabi oscillations between the electron and trion states in QD #1. An oscillatory fit of the data (red curve) yields a trion dipole moment of ~ 8 Debye. (b) Theoretical plot of the modulated APD photocurrent as a function of pump pulse area taking into account the trion state of QD #2, which is assumed to have a dipole moment approximately twice that of QD #1.

behavior as the experimentally measured V_{sig} values, supporting the hypothesis that the dimpling phenomenon is due to the presence of QD #2.

4.6 Pump-Probe Studies with $\mathbf{B}_{\text{ext}} = B\hat{x}$: Electron and Heavy-Hole Spin Quantum Beats

Application of an external DC magnetic field in the Voigt geometry enables the observation of electron and heavy-hole spin precession with the use of circularly polarized pump and probe beams, as discussed in Section 3.5. For the case of circularly cross-polarized beams, V_{sig} measurements as a function of pulse delay have the form

$$V_{\text{sig}} = M \sin^2[\theta_{pr}/2] \times \left\{ \frac{1}{4} \sin^2[\theta_{pu}/2] \Theta(t_d) \left[2e^{-2\Gamma t_d} - e^{-t_d/T_2^e} \cos(\Delta_e t_d) - e^{-2\Gamma t_d} e^{-t_d/T_2^h} \cos(\Delta_h t_d) \right] - \frac{1}{2} \right\} \quad (4.5)$$

where we see that the signal consists of two damped oscillations, each reflecting the precession (and dephasing) of a particular spin in the dot. Experimental measurements of V_{sig} are plotted in Figure 4.13 as a function of t_d for two external magnetic field strengths. The data show a two-frequency oscillation as a function of pulse delay at each magnetic field value due to the precession of both electron and heavy-hole

spins, as expected from the theory.

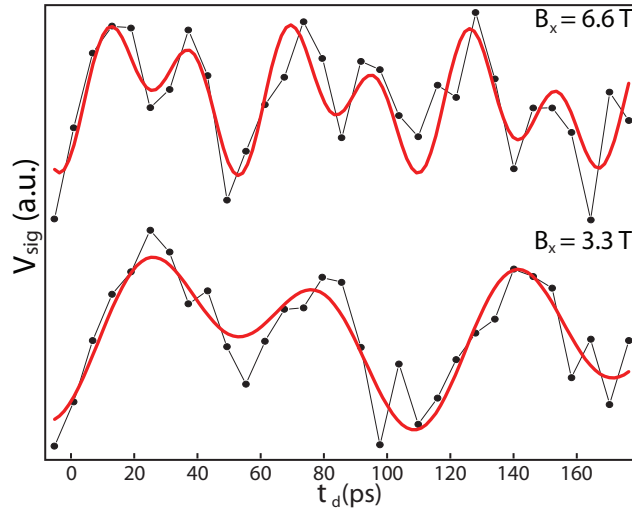


Figure 4.13: V_{sig} measurements as a function of t_d for circularly cross-polarized excitation at $B = 3.3$ T and $B = 6.6$ T. The red curves are fits obtained with Equation 4.5 taken in the limit of infinitely long electron and heavy-hole spin coherence times.

As the range of pump-probe delays considered in Figure 4.13 is much shorter than anticipated electron and heavy-hole spin coherence times [120,124], we are unable to extract reliable values of the electron and heavy-hole spin coherence times. To obtain reliable values of the electron and heavy-hole spin coherence times, considerably longer delays would need to be considered in order to clearly observe the damping associated with each oscillating term. Due to the amount of averaging required to achieve sufficiently high SNR, these extended pulse delay range studies would require the averaging of data sets obtained over the course of multiple days and have not been pursued in this thesis. Instead, the data of Figure 4.13 are fit to Equation 4.5 taken in the limit of infinitely long electron and heavy-hole dephasing times, resulting in the solid red curves of Figure 4.13. The agreement between the data and the fitting indeed suggest spin coherence times that are much longer than the pump-probe delay values considered here. From the fittings we obtain electron and heavy-hole in-plane g-factor magnitudes $|g_e|$ and $|g_h|$ of $.378 \pm .007$ and $.202 \pm .006$, respectively.

4.7 Chapter Summary

The experimental setup and QD characterization process were discussed in detail. PL spectroscopy was presented as the first characterization procedure, used to identify individual QD charge states and their sample bias voltage dependent transition energies. CW Stark shift modulation absorption spectroscopy was presented as the next characterization step, which enables the determination of the voltage and energy ranges within which a particular QD state absorbs. For the trion of QD #1, knowledge of this absorption range was applied to pulsed Stark shift modulation absorption spectroscopy. These studies demonstrated the ability to read out the states of a single InAs QD as well as the ability to coherently control the electron-trion transitions in a single QD, as evidenced in the observation of pulse-driven Rabi oscillations. This read-out method was then applied to pump-probe studies both with and without an externally applied magnetic field, where phenomena such as trion excitation and decay, trion Rabi oscillations and spin precession were experimentally observed. These observations demonstrate that optical pulses may be used to coherently control the transitions in a QD and to generate spin coherence via two-photon Raman transitions. Such capabilities will be utilized in the following Chapters to demonstrate optical manipulation of a spin qubit in a single InAs QD.

CHAPTER 5

Theoretical Spin Qubit Gates for an Electron Confined in an InAs QD

In the previous two Chapters we investigated pulsed optical studies of a single self-assembled InAs QD, demonstrating read-out of QD states, coherent control of optical transitions in the QD and optically generated two-photon Raman coherence between spin states in the QD. Building upon these results, we now pursue demonstrations of qubit gates for an electron spin confined in a single InAs QD, first discussing the theory of possible spin control mechanisms in the singly charged QD system. These theoretical considerations allow for the description of the various spin control mechanisms in terms of unitary transformation matrices that can then be used to construct a number of critical single qubit gates.

Here, we consider three primary means of spin control: optical pulses highly detuned from the electron-trion transition, an external DC magnetic field and a narrow-bandwidth CW field tuned to one of the electron-trion transitions in the QD. Unitary transformation matrices describing each type of spin manipulation are obtained by solving for the probability amplitudes of the four-level system. As will be seen, spin control mechanisms enable the rotation of the spin vector about two orthogonal axes, thus providing a means of constructing arbitrary unitary single qubit operations [39]. Possible spin qubit gates for each spin control mechanism are then presented, with particular attention given to the phase gate S , the $\pi/8$ gate T and the Hadamard gate H , as these single qubit gates can be used with either two-bit controlled-NOT gates [3] or two-bit exclusive OR gates [39] to construct an arbitrary unitary operation on n qubits [209]. Finally, as the Hadamard gate requires a series of rotations

about orthogonal axes, a number of different methods of constructing this gate are presented.

5.1 The Interaction of a Highly-Detuned Optical Pulse with a QD Confined Electron Spin

We first investigate the operation of a pulse that is highly detuned from the electron-trion transition. Highly detuned pulses are chosen since they leave a minimal amount of population in the trion states after excitation. Such population is undesirable as it reduces the fidelity of spin qubit operations. In addition, we consider the case where an external DC magnetic field is applied in the Voigt geometry. This particular geometry is chosen as it enables the use of spin precession to rotate the spin (discussed later in this Chapter) and has been demonstrated to permit fast spin initialization times on the order of 10^{-9} s [128], while spin preparation schemes in other geometries such as the Faraday geometry (magnetic field along growth axis) require times on the order of 10^{-6} s [126]. Implementation of the Voigt profile spin preparation scheme will be discussed in the following Chapter, as it will serve as the crucial first step in experimental demonstrations of coherent control of the electron spin.

5.1.1 Equations of Motion for the Electron Spin Probability Amplitudes

Figure 5.1 shows the energy level diagram of the system along with the labeling scheme used to simplify mathematical expressions. Energy scales are also indicated, as well as the quantities associated with the optical pulse (ω_p , δ_p) and the narrow-bandwidth CW field (ω_{cw} , δ_{cw}) considered later in this Chapter. The excitation pulse is taken to have the form

$$\mathbf{E}_p(t) = \frac{1}{2}E_p \operatorname{sech}\left(\frac{t}{\tau}\right) [\hat{\epsilon}e^{-i\omega_p t} + c.c.] \quad (5.1)$$

where $\hat{\epsilon} = (1/\sqrt{2})(\hat{x} + e^{i\phi}\hat{y})$ is the pulse polarization and is left in terms of a phase

we seek to describe the operation of the highly detuned pulse in terms of a unitary transformation matrix $U_p(t', t)$ where

$$\begin{bmatrix} C_1(t') \\ C_2(t') \end{bmatrix} = \begin{bmatrix} U_p(t', t) \end{bmatrix} \begin{bmatrix} C_1(t) \\ C_2(t) \end{bmatrix}. \quad (5.6)$$

To do this, we need to solve the Schödinger equation for the entire four level system of Figure 5.1 in the amplitude picture, i.e. for the total system wavefunction

$$|\Psi_{tot}\rangle = C_1(t)|1\rangle + C_2(t)|2\rangle + C_3(t)|3\rangle + C_4(t)|4\rangle \quad (5.7)$$

we seek solutions to the set of first order differential equations generated by the relation

$$\dot{C}_i(t) = \frac{1}{i\hbar} \sum_j H_{ij} C_j(t). \quad (5.8)$$

We note that although the amplitude picture does not take into account decay processes such as trion and spin relaxation that generally detract from the unitary description of the pulse operation, the errors introduced by these processes are small enough to be ignored as the timescale of the pulse operation (< 2 ps) is orders of magnitude shorter than the timescales of all relaxation processes in the dot.

To solve the differential equations generated by Equation 5.8, we first move into the FIP using the transformations

$$C_{1,2}(t) = \tilde{C}_{1,2}(t) \quad (5.9)$$

$$C_{3,4}(t) = \tilde{C}_{3,4}(t)e^{-i\omega_p t} \quad (5.10)$$

and then apply the RWA to obtain the following equations of motion:

$$\dot{\tilde{C}}_1(t) = \frac{i\Delta_e}{2}\tilde{C}_1(t) + \frac{i\chi_p}{\sqrt{2}}\text{sech}\left(\frac{t}{\tau}\right) \left[ie^{-i\phi}\tilde{C}_3(t) + \tilde{C}_4(t) \right] \quad (5.11)$$

$$\dot{\tilde{C}}_2(t) = -\frac{i\Delta_e}{2}\tilde{C}_2(t) + \frac{i\chi_p}{\sqrt{2}}\text{sech}\left(\frac{t}{\tau}\right) \left[\tilde{C}_3(t) + ie^{-i\phi}\tilde{C}_4(t) \right] \quad (5.12)$$

$$\dot{\tilde{C}}_3(t) = -i\left(\delta_p - \frac{\Delta_h}{2}\right)\tilde{C}_3(t) + \frac{i\chi_p}{\sqrt{2}}\text{sech}\left(\frac{t}{\tau}\right) \left[-ie^{i\phi}\tilde{C}_1(t) + \tilde{C}_2(t) \right] \quad (5.13)$$

$$\dot{\tilde{C}}_4(t) = -i\left(\delta_p + \frac{\Delta_h}{2}\right)\tilde{C}_4(t) + \frac{i\chi_p}{\sqrt{2}}\text{sech}\left(\frac{t}{\tau}\right) \left[\tilde{C}_1(t) - ie^{i\phi}\tilde{C}_2(t) \right]. \quad (5.14)$$

We now make use of the fact that the pulses are highly detuned from the electron-trion transition, specifically considering the pulses to be *red*-detuned ($\delta_p > 0$), and take the following conditions [210] to be satisfied:

$$\delta_p \gg \Delta_e, \Delta_h \quad (5.15)$$

$$|\chi_p C_1(t)| \gg \left| \frac{d}{dt} \left(\frac{\chi_p C_1(t)}{\delta_p} \right) \right| \quad (5.16)$$

$$|\chi_p C_2(t)| \gg \left| \frac{d}{dt} \left(\frac{\chi_p C_2(t)}{\delta_p} \right) \right|. \quad (5.17)$$

These conditions allow us to solve for the probability amplitudes of the trion states by integrating Equations 5.13 and 5.14 by parts, yielding

$$\tilde{C}_3(t) \approx \frac{\chi_p}{\sqrt{2}\delta_p} \operatorname{sech} \left(\frac{t}{\tau} \right) \left[-ie^{i\phi} \tilde{C}_1(t) + \tilde{C}_2(t) \right] \quad (5.18)$$

$$\tilde{C}_4(t) \approx \frac{\chi_p}{\sqrt{2}\delta_p} \operatorname{sech} \left(\frac{t}{\tau} \right) \left[\tilde{C}_1(t) - ie^{i\phi} \tilde{C}_2(t) \right] \quad (5.19)$$

where the trion states have been “adiabatically eliminated” by expressing their probability amplitudes in terms of electron spin probability amplitudes. These approximations leave us only with the equations of motion governing the electron spin probability amplitudes, i.e.

$$\dot{\tilde{C}}_1(t) = \left[\frac{i\Delta_e}{2} + \frac{i\chi_p^2}{\delta_p} \operatorname{sech}^2 \left(\frac{t}{\tau} \right) \right] \tilde{C}_1(t) + \operatorname{Re} [ie^{-i\phi}] \frac{i\chi_p^2}{\delta_p} \operatorname{sech}^2 \left(\frac{t}{\tau} \right) \tilde{C}_2(t) \quad (5.20)$$

$$\dot{\tilde{C}}_2(t) = \operatorname{Re} [ie^{-i\phi}] \frac{i\chi_p^2}{\delta_p} \operatorname{sech}^2 \left(\frac{t}{\tau} \right) \tilde{C}_1(t) + \left[-\frac{i\Delta_e}{2} + \frac{i\chi_p^2}{\delta_p} \operatorname{sech}^2 \left(\frac{t}{\tau} \right) \right] \tilde{C}_2(t). \quad (5.21)$$

By solving these equations under certain conditions we may obtain the unitary transformation associated with the operation of the pulse, but before doing so it is worthwhile to take a closer look at the physics behind them.

5.1.2 Effective Hamiltonian and Bloch Sphere Representation

From Equations 5.20 and 5.21 we can express an effective electron spin Hamiltonian H_{spin} as

$$H_{spin} = \hbar \begin{bmatrix} -\frac{\Delta_e}{2} - \frac{\chi_p^2}{\delta_p} \operatorname{sech}^2 \left(\frac{t}{\tau} \right) & -\operatorname{Re} [ie^{-i\phi}] \frac{\chi_p^2}{\delta_p} \operatorname{sech}^2 \left(\frac{t}{\tau} \right) \\ -\operatorname{Re} [ie^{-i\phi}] \frac{\chi_p^2}{\delta_p} \operatorname{sech}^2 \left(\frac{t}{\tau} \right) & \frac{\Delta_e}{2} - \frac{\chi_p^2}{\delta_p} \operatorname{sech}^2 \left(\frac{t}{\tau} \right) \end{bmatrix} \quad (5.22)$$

where we see from the diagonal terms that, in addition to the Zeeman splitting, there is a pulse induced AC Stark shift of both electron spin states to lower energies. Of particular interest is the dependence of the off-diagonal matrix elements of H_{spin} on the phase between the \hat{x} and \hat{y} components of the pulse polarization $\hat{\epsilon}$. For linear polarization, ($\phi = \pi n$ where n is an integer) these matrix elements are zero, while for circular polarization ($\phi = \pi/2 + \pi n$ where n is an integer) the magnitude of each of these elements is maximized.

To more clearly see the physical consequences of this polarization dependence, we disregard the AC Stark shifts of the electron spin states and compare the form of H_{spin} with the standard two-level FIP Hamiltonian

$$\tilde{H} = \hbar \begin{bmatrix} -\frac{\tilde{\delta}}{2} & \tilde{\chi}^* \\ \tilde{\chi} & \frac{\tilde{\delta}}{2} \end{bmatrix} \quad (5.23)$$

finding that

$$\tilde{\delta} = \Delta_e \quad (5.24)$$

$$\tilde{\chi} = -\text{Re} [ie^{-i\phi}] \frac{\chi_p^2}{\delta_p} \text{sech}^2 \left(\frac{t}{\tau} \right). \quad (5.25)$$

We then employ the machinery of the Bloch sphere representation in $\{u, v, w\}$ space [211] with the definitions

$$\mathbf{B} = \begin{bmatrix} B_u \\ B_v \\ B_w \end{bmatrix} = \begin{bmatrix} 2\text{Re}[\tilde{\rho}_{12}(t)] \\ -2\text{Im}[\tilde{\rho}_{12}(t)] \\ \tilde{\rho}_{22}(t) - \tilde{\rho}_{11}(t) \end{bmatrix} = \begin{bmatrix} 2\text{Re}[\tilde{C}_1(t)\tilde{C}_2^*(t)] \\ -2\text{Im}[\tilde{C}_1(t)\tilde{C}_2^*(t)] \\ \tilde{C}_2(t)\tilde{C}_2^*(t) - \tilde{C}_1(t)\tilde{C}_1^*(t) \end{bmatrix} \quad (5.26)$$

$$\mathbf{\Omega} = \begin{bmatrix} \Omega_u \\ \Omega_v \\ \Omega_w \end{bmatrix} = \begin{bmatrix} 2\text{Re}[\tilde{\chi}] \\ -2\text{Im}[\tilde{\chi}] \\ \tilde{\delta} \end{bmatrix} = \begin{bmatrix} -2\text{Re} [ie^{-i\phi}] \frac{\chi_p^2}{\delta_p} \text{sech}^2 \left(\frac{t}{\tau} \right) \\ 0 \\ \Delta_e \end{bmatrix} \quad (5.27)$$

$$d\mathbf{B}/dt = \mathbf{\Omega} \times \mathbf{B} \quad (5.28)$$

where Equation 5.28 signifies that the spin Bloch vector \mathbf{B} precesses about the pseudofield vector $\mathbf{\Omega}$ at the angular frequency $|\mathbf{\Omega}|$. We make use of the fact that the spin Bloch sphere in $\{u, v, w\}$ space bears a direct relationship to the Bloch sphere in

real space, allowing us to describe the time-evolution of the spin vector in terms of real-space coordinates (Appendix C), i.e.

$$\hat{u} \rightarrow \hat{z} \quad (5.29)$$

$$\hat{v} \rightarrow \hat{y} \quad (5.30)$$

$$\hat{w} \rightarrow -\hat{x}, \quad (5.31)$$

leading to a real space psuedofield vector of the form

$$\mathbf{\Omega} = \begin{bmatrix} \Omega_x \\ \Omega_y \\ \Omega_z \end{bmatrix} = \begin{bmatrix} -\Delta_e \\ 0 \\ -2\text{Re} [ie^{-i\phi}] \frac{\chi_p^2}{\delta_p} \text{sech}^2 \left(\frac{t}{\tau} \right) \end{bmatrix}. \quad (5.32)$$

The dynamics of the spin vector in real space then lends itself to a straightforward description: before and after the pulse the psuedofield vector lies along $-\hat{x}$, resulting in a clock-wise rotation of the spin vector about the \hat{x} axis at an angular frequency of Δ_e . This behavior corresponds to spin precession about the external magnetic field and will be discussed in more detail in the following section. During the pulse, the psuedofield vector has an additional component lying along the \hat{z} axis only if the pulse is elliptically or circularly polarized. In addition, the pulse dependent component of the psuedofield vector rotates the spin vector only about the \hat{z} axis; rotations about other axes are not possible with highly detuned pulses. This limitation is the result of interference between the two two-photon quantum mechanical pathways (Λ_1 and Λ_2 of Figure 5.1) between the two spin states.

To obtain rotations of the spin about an axis orthogonal to the \hat{z} axis requires the use of either spin precession about the external magnetic field or geometric phases imparted by optically driven 2π rotations of the trion transitions in the dot, as will be shown later in this Chapter. For now, we consider solutions to Equations 5.20 and 5.21 for a circularly polarized pulse.

5.1.3 Unitary Transformation Matrix for a Circularly Polarized Pulse

The unitary transformation associated with the operation of a $\hat{\sigma}_+$ polarized pulse ($\phi = 0$) may be obtained by ignoring the AC Stark shifts—since they are equal for

both spin states—and making use of the fact that the operation time of the pulse (i.e. the pulse width) is much shorter than the spin precession period for magnetic fields of a few T or more, allowing us to disregard the effect of spin precession during the pulse. These simplifications result in equations of the form

$$\dot{\tilde{C}}_1(t) = \frac{i\chi_p^2}{\delta_p} \operatorname{sech}^2\left(\frac{t}{\tau}\right) \tilde{C}_2(t) \quad (5.33)$$

$$\dot{\tilde{C}}_2(t) = \frac{i\chi_p^2}{\delta_p} \operatorname{sech}^2\left(\frac{t}{\tau}\right) \tilde{C}_1(t), \quad (5.34)$$

yielding the unitary transformation matrix

$$U_p(t', t) = \begin{bmatrix} \cos\left\{\frac{\chi_p^2\tau}{\delta_p} [\tanh(\frac{t'}{\tau}) - \tanh(\frac{t}{\tau})]\right\} & i \sin\left\{\frac{\chi_p^2\tau}{\delta_p} [\tanh(\frac{t'}{\tau}) - \tanh(\frac{t}{\tau})]\right\} \\ i \sin\left\{\frac{\chi_p^2\tau}{\delta_p} [\tanh(\frac{t'}{\tau}) - \tanh(\frac{t}{\tau})]\right\} & \cos\left\{\frac{\chi_p^2\tau}{\delta_p} [\tanh(\frac{t'}{\tau}) - \tanh(\frac{t}{\tau})]\right\} \end{bmatrix}. \quad (5.35)$$

For a general set of initial conditions before the pulse, the state of the system after the pulse can be described by the approximate unitary transformation

$$U_p(\theta) = \begin{bmatrix} \cos(\theta/2) & i \sin(\theta/2) \\ i \sin(\theta/2) & \cos(\theta/2) \end{bmatrix}, \quad \theta = \frac{\Omega_p^2\tau}{\delta_p} \quad (5.36)$$

where $\Omega_p = \frac{\mu E_p}{\hbar}$. This approximate unitary transformation matrix is more than 99% accurate as long as the magnitudes of t' and t are greater than 3τ .

The unitary transformation matrix of Equation 5.36 has the form of a clockwise rotation about the \hat{z} axis by an angle θ . Notable spin qubit gates [3] that may be constructed by the operation of a detuned circularly polarized pulse (to within an arbitrary global phase) are the X gate,

$$U_p(\theta = \pi) = e^{i\pi/2} \begin{bmatrix} 0 & 1 \\ 1 & 0 \end{bmatrix} = e^{i\pi/2} X, \quad (5.37)$$

a prevalent gate in stabilizer codes for quantum error correction [3], and the gate

$$U_p(\theta = \pi/2) = \frac{1}{\sqrt{2}} \begin{bmatrix} 1 & i \\ i & 1 \end{bmatrix}, \quad (5.38)$$

which will play a crucial role in the construction of a Hadamard gate later in this Chapter.

5.2 The Operation of the External Magnetic Field

As discussed in the previous section, the Zeeman splitting between the electron spin states generated by the magnetic field leads to a constant component of the pseudofield vector along the \hat{x} axis, resulting in spin precession. The unitary transformation matrix associated with the operation of the magnetic field can be determined by solving Equations 5.20 and 5.21 in the absence of the pulse, i.e.

$$\dot{\tilde{C}}_1(t) = \frac{i\Delta_e}{2}\tilde{C}_1(t) \quad (5.39)$$

$$\dot{\tilde{C}}_2(t) = -\frac{i\Delta_e}{2}\tilde{C}_2(t). \quad (5.40)$$

Solutions to these equations are trivial and yield

$$U_B(t', t) = U_B(\vartheta) = \begin{bmatrix} e^{i\vartheta/2} & 0 \\ 0 & e^{-i\vartheta/2} \end{bmatrix}, \quad \vartheta = \Delta_e(t' - t) \quad (5.41)$$

which is a clock-wise rotation about the \hat{x} axis. This unitary transformation matrix may be used to form the important S and T gates,

$$U_B(\vartheta = 3\pi/2) = e^{3i\pi/4} \begin{bmatrix} 1 & 0 \\ 0 & i \end{bmatrix} = e^{3i\pi/4} S \quad (5.42)$$

$$U_B(\vartheta = 7\pi/4) = e^{7i\pi/8} \begin{bmatrix} 1 & 0 \\ 0 & e^{i\pi/4} \end{bmatrix} = e^{7i\pi/8} T, \quad (5.43)$$

as well as the Z gate

$$U_B(\vartheta = \pi) = e^{i\pi/2} \begin{bmatrix} 1 & 0 \\ 0 & -1 \end{bmatrix} = e^{i\pi/2} Z, \quad (5.44)$$

which, as with the X gate, plays a crucial role in stabilizer codes.

As spin precession rotates the electron spin about the \hat{x} axis, combinations of pulse-driven spin rotations about the \hat{z} axis and spin precession may be used to form

a universal set of single spin qubit gates [39], a crucial requirement for executing quantum algorithms with QD spins. There are, however, a number of drawbacks to using spin precession to achieve universal qubit gates. For one, spin precession about \hat{x} occurs continuously unless the spin is rotated by some other means to lie long \hat{x} or the magnetic field is turned off. In other words, as long as the magnetic field is on the spin vector orientation does not “stay put” unless it lies along the magnetic field axis. Another drawback is that fast spin precession periods on the order of a few tens of ps require large magnetic fields on the order of several Tesla.

An alternative approach to achieving spin rotations about an axis orthogonal to the optical axis is by the use of optically imparted geometric phases, which we now discuss.

5.3 Geometric Phases Imparted by a CW Field

The final means of spin control we consider is a CW field of the form

$$\mathbf{E}_{cw} = \hat{x}E_{cw} \cos(\omega_{cw}t) \quad (5.45)$$

that serves to drive Rabi oscillations between states $|1\rangle$ and $|4\rangle$ in the dot. As any cyclic evolution in a quantum system leads to the accrual of a geometric phase [212], the optically driven trion Rabi oscillations impart a geometric phase to the probability amplitude of the $|1\rangle$ state for each complete 2π Rabi oscillation. This optically imparted geometric phase depends on the CW field detuning and amplitude and results in an effective rotation of the electron spin about the quantization axis, which in this case is \hat{x} due to the external magnetic field.

This effective rotation can also be represented in terms of a unitary transformation matrix, the form of which may be determined by solving for the probability amplitudes of the system. To simplify the problem we take the detuning δ_{cw} to be much smaller than the sum of the electron and heavy-hole Zeeman splittings so that the CW field does not drive the $|2\rangle$ to $|3\rangle$ transition, allowing us to simply consider the $|1\rangle$ to $|4\rangle$ transition. Assuming no initial population in the trion states, this simplification leads

to the following expressions for the $|1\rangle$ and $|4\rangle$ probability amplitudes:

$$C_1(t') = C_1(t)e^{-i\delta_{cw}(t'-t)/2} \times \left\{ \frac{i\delta_{cw}}{\sqrt{\delta_{cw}^2 + \Omega_{cw}^2}} \sin \left[\frac{1}{2} \sqrt{\delta_{cw}^2 + \Omega_{cw}^2} (t' - t) \right] + \cos \left[\frac{1}{2} \sqrt{\delta_{cw}^2 + \Omega_{cw}^2} (t' - t) \right] \right\} \quad (5.46)$$

$$C_4(t') = -C_1(t)e^{-i\omega_{cw}t} e^{-i\delta_{cw}(t'-t)/2} \frac{i\Omega_{cw}}{\sqrt{\delta_{cw}^2 + \Omega_{cw}^2}} \sin \left[\frac{1}{2} \sqrt{\delta_{cw}^2 + \Omega_{cw}^2} (t' - t) \right] \quad (5.47)$$

where $\Omega_{cw} = \frac{\mu E_{cw}}{\hbar}$.

By inspecting Equations 5.46 and 5.47 we find that complete cycles in the trion Rabi oscillation occur for $t' - t = \Delta t_n = \frac{2n\pi}{\sqrt{\delta_{cw}^2 + \Omega_{cw}^2}}$, where n is an integer indicating the number complete trion Rabi oscillations that have occurred during the particular time interval Δt_n . At these particular points in time, the unitary transformation matrix associated with the optically imparted geometric phase has the form

$$U_{cw}(t', t) = U_{cw}(\Delta t_n) = \begin{bmatrix} (-1)^n e^{-i\delta_{cw}\Delta t_n/2} & 0 \\ 0 & 1 \end{bmatrix} \quad (5.48)$$

which can be rewritten as

$$U_{cw}(\varphi) = e^{-i\varphi/2} \begin{bmatrix} (-1)^n e^{-i\varphi/2} & 0 \\ 0 & e^{i\varphi/2} \end{bmatrix}, \quad \varphi = \delta_{cw}\Delta t_n/2. \quad (5.49)$$

Equation 5.49 has the standard form of a counter-clockwise rotation about the \hat{x} axis for n even, the timescale of operation depending on the generalized Rabi period $T_{cw} = \frac{\Delta t_n}{n}$.

As in the case of precession, S and T gates can be formed with proper selection of parameters. For n odd,

$$U_{cw}(\varphi = -\pi/2) = -e^{i\pi/2} \begin{bmatrix} 1 & 0 \\ 0 & i \end{bmatrix} = -e^{i\pi/2} S \quad (5.50)$$

$$U_{cw}(\varphi = -3\pi/4) = -e^{3i\pi/4} \begin{bmatrix} 1 & 0 \\ 0 & e^{i\pi/4} \end{bmatrix} = -e^{3i\pi/4} T \quad (5.51)$$

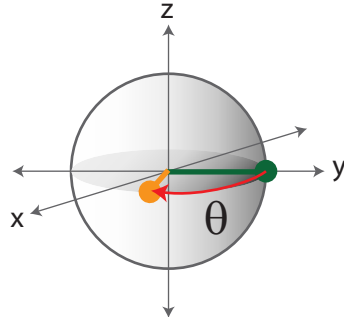
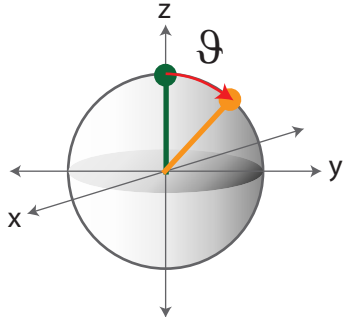
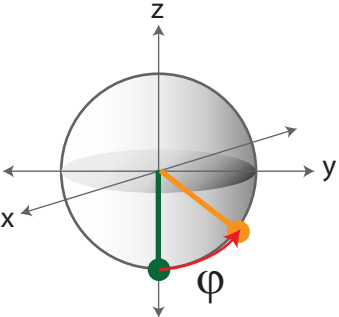
detuned σ_+ pulse	B field	CW field (n even)
		
$U_p(\theta) =$ $\begin{bmatrix} \cos(\theta/2) & i \sin(\theta/2) \\ i \sin(\theta/2) & \cos(\theta/2) \end{bmatrix}$	$U_B(\vartheta) =$ $\begin{bmatrix} \exp(i\vartheta/2) & 0 \\ 0 & \exp(-i\vartheta/2) \end{bmatrix}$	$U_{cw}(\varphi) = \exp(-i\varphi/2) x$ $\begin{bmatrix} \exp(-i\varphi/2) & 0 \\ 0 & \exp(i\varphi/2) \end{bmatrix}$

Figure 5.2: Bloch sphere representations (real space) and the unitary transformation matrices associated with the three different means of electron spin control considered in this Chapter. The Bloch spheres demonstrate the operation of each spin control mechanism on some initial spin vector (green), resulting in a rotated spin vector (orange).

while for n even

$$U_{cw}(\varphi = \pi/2) = e^{-i\pi/2} \begin{bmatrix} (-1)^n & 0 \\ 0 & i \end{bmatrix} = e^{-i\pi/2} S \quad (5.52)$$

$$U_{cw}(\varphi = \pi/4) = e^{-i\pi/4} \begin{bmatrix} (-1)^n & 0 \\ 0 & e^{i\pi/4} \end{bmatrix} = e^{-i\pi/4} T. \quad (5.53)$$

In addition, for a resonant CW field ($\delta_{cw} = 0$), the unitary transformation matrix has the form

$$U_{cw} = \begin{bmatrix} (-1)^n & 0 \\ 0 & 1 \end{bmatrix} \quad (5.54)$$

which is either the identity matrix I or a Z gate, depending on n .

A potential key advantage to utilizing the effect of geometric phases to perform spin rotation is that these phases may be imparted by optical pulses, theoretically enabling operation times as fast as several tens of ps in QD systems [133]. Even faster operation times may be possible for systems possessing isolated excited states

or an optical cycling transition [43, 213]. In potential QD-based quantum computing architectures, a combination of spatial selectivity and voltage control of the QD charge state may be used to tailor the operation of optical pulses to particular QDs, enabling dot-selective universal spin qubit operations.

Figure 5.2 provides a summary illustration of the three different spin control mechanisms considered in this Chapter, giving the Bloch sphere pictures of each type of operation as well as the unitary transformation matrices associated with each. With the three spin control mechanisms characterized, we now finally turn to methods of constructing the Hadamard gate.

5.4 Hadamard Gate Construction

Operation Sequence	Global Phase (Φ)
$U_B(\vartheta = \pi/2)U_p(\theta = \pi/2)U_B(\vartheta = \pi/2)$	$\pi/2$
$U_{cw}(\varphi = \pi/2)U_p(\theta = \pi/2)U_{cw}(\varphi = \pi/2)$	π (n odd)
$U_{cw}(\varphi = \pi/2)U_p(\theta = \pi/2)U_B(\vartheta = \pi/2)$	$3\pi/4$ (n odd)
$U_p(\theta = \pi/2)U_B(\vartheta = \pi/2)U_p(\theta = \pi/2)$	$\pi/2$
$U_p(\theta = \pi/2)U_{cw}(\varphi = \pi/2)U_p(\theta = \pi/2)$	$3\pi/4$ (n odd)

Table 5.1: Different combinations of the three unitary transformations resulting in a Hadamard gate and the global phases for each.

Here, we consider different means of constructing the Hadamard gate

$$H = \frac{1}{\sqrt{2}} \begin{bmatrix} 1 & 1 \\ 1 & -1 \end{bmatrix} \quad (5.55)$$

by forming different combinations of the three unitary transformations treated in this Chapter. The basic procedure for Hadamard gate construction is to execute a $\pi/2$ rotation about some axis, execute a $\pi/2$ rotation about an orthogonal axis, and then execute another $\pi/2$ rotation about the first axis. Table 5.1 gives a number of the possible unitary transformation sequences that correspond to a Hadamard gate

operation, as well as the global phase Φ associated with each sequence (i.e. $e^{i\Phi}H$). Though there are a number of different ways to construct a Hadamard gate operation, we will consider the sequence given in the fourth row of Table 5.1 in the following Chapter for experimental demonstrations.

5.5 Chapter Summary

Three different means of spin control were presented: circularly polarized pulses red-detuned from the trion transition energies, an externally applied DC magnetic field and a narrow-bandwidth CW field tuned near one of the trion transitions. Unitary transformation matrices for each type of spin control method were determined by solving for the probability amplitudes of the four level system. These matrices revealed that detuned circularly polarized pulses execute spin rotations about the optical axis \hat{z} , while the magnetic and CW fields rotate the spin about the magnetic field axis \hat{x} . Possible single qubit gates were given for each method of spin control, and example sequences using multiple unitary transformation matrices were given for the construction of a Hadamard gate. A number of the qubit gates presented will play crucial roles in experimental demonstrations of spin control in the following Chapter.

CHAPTER 6

Experimental Demonstrations of Spin Qubit Rotations About Two Orthogonal Axes

Ultimately, the development of a practical quantum computer consisting of qubits based on the spin states of QD confined charges requires the ability to coherently control these spins. As mentioned in Chapter 1, the use of optical techniques offers a number of advantages for quantum computing, viz the ability to initialize, manipulate and read-out spin qubit states. In particular, optical approaches offer the highly attractive prospect of *ultrafast* spin qubit control, a capability that is unobtainable with the electrically or magnetically based approaches to qubit control employed in other quantum computing implementations. Further, optical control of a QD confined spin in an externally applied DC magnetic field in the Voigt profile enables the construction of arbitrary unitary operations on the spin qubit using a combination of two-photon spin control and either spin precession or optically imparted geometric phases.

In this Chapter, we experimentally demonstrate the coherent optical control of an electron spin confined in a self-assembled InAs QD that is initialized to a pure state. Initialization is achieved by tuning a narrow-bandwidth CW field to one of the trion transitions in the QD, optically pumping the electron spin to a particular pure state depending on which trion transition is driven [127, 128]. This same CW field is also used to perform read-out by effectively measuring the amount of population that re-enters the $|1\rangle$ state after initialization, a method that is referred to as optical tripwire read-out. With this read-out technique the operation of a single pulse is then

investigated for different pulse detunings and polarizations, showing the complete two-photon rotation of the electron spin about the optical axis \hat{z} for a detuned circularly polarized pulse. Two-pulse studies are then performed to demonstrate spin rotation by precession about the external magnetic field and are used to show a number of spin qubit gates for different values of the pulse delay. Finally, two-pulse studies covering an extended pulse delay range are then used to demonstrate net rotations of the electron spin about the magnetic field axis as a result of the geometric phases imparted to one of the electron spin states by the driving of trion Rabi oscillations by the CW field after the first pulse.

6.1 Spin Initialization by Optical Pumping with a CW Field

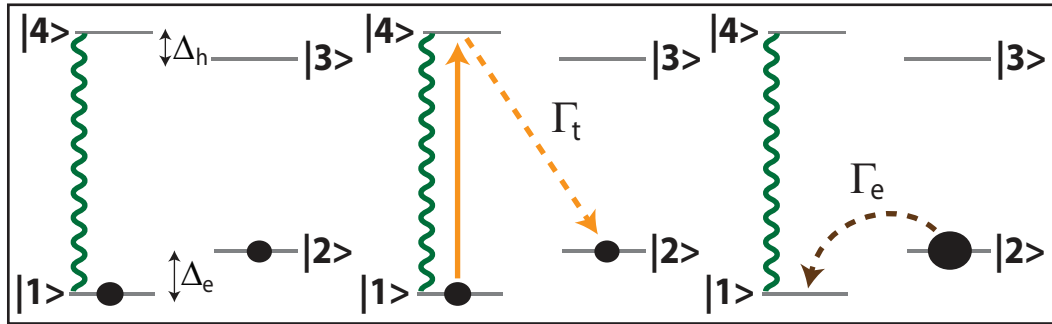


Figure 6.1: Illustration of the optical pumping process for a CW field tuned to the $|1\rangle$ to $|4\rangle$ transition. The electron spin is assumed to be in a mixed state prior to the operation of the CW field and the trion relaxation rate Γ_t is assumed to be much greater than the electron spin relaxation rate Γ_e .

To demonstrate complete coherent control of the electron spin, the spin is first prepared in a pure state. In the Voigt configuration, this is done by tuning a narrow-bandwidth CW field to one of the trion transitions in the dot. We choose the $|1\rangle$ to $|4\rangle$ transition. In this case, the CW field drives population to the $|4\rangle$ state that subsequently relaxes with equal rates Γ_t to both of the electron spin ground states. Population that relaxes to the $|2\rangle$ state begins to decay to $|1\rangle$ at the spin relaxation rate Γ_e , while population that relaxes back to $|1\rangle$ is then re-excited by the CW field. For a spin relaxation rate much slower than the trion relaxation rate, this process

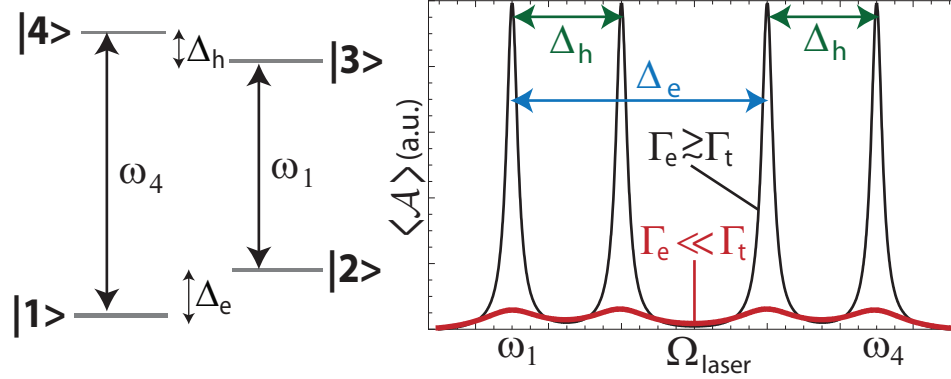


Figure 6.2: Theoretical plots of the time averaged absorption $\langle \mathcal{A} \rangle$ as a function of laser frequency for $\Gamma_e \gtrsim \Gamma_t$ (black curve) and $\Gamma_e \ll \Gamma_t$ (red curve). Optical pumping, by depleting the $|1\rangle$ state population, leads to a diminished absorption signal.

repeats until the CW field optically pumps all $|1\rangle$ population to $|2\rangle$, as illustrated in Figure 6.1. For CW trion Rabi frequencies greater than Γ_t , the optical pumping timescale is limited by the trion relaxation rate and is defined in terms of the characteristic timescale $T_0 = 1/\Gamma_t$ [127]. Based on absorption linewidth comparisons with and without an externally applied magnetic field (data not shown), we take the trion relaxation rate Γ_t to be independent of the magnetic field. From the trion decay measurements of Section 4.5, this yields a T_0 value of approximately 0.9 ns.

Crucial to the ability to optically pump the electron spin is an electron spin relaxation rate that is much slower than the trion relaxation rate, i.e. $\Gamma_e \ll \Gamma_t$. For $\Gamma_e \gtrsim \Gamma_t$, it is not possible to prepare the electron spin in a pure state as $|2\rangle$ population relaxes back to $|1\rangle$ too quickly to deplete $|1\rangle$ of its population. This dependence of the initialization process on the relative values of Γ_t and Γ_e has consequences for absorption studies performed with an external magnetic field. Figure 6.2 plots the theoretical time-averaged absorption $\langle \mathcal{A} \rangle$ as a function of laser frequency for fast (black curve) and slow (red curve) spin relaxation rates compared to the trion relaxation rates. For the case where electron spin relaxation is slow, complete depletion of the $|1\rangle$ state occurs, resulting in the $|1\rangle$ to $|4\rangle$ transition becoming transparent. This leads to a much weaker absorption signal compared to the fast spin relaxation case, where depletion of the $|1\rangle$ state does not occur.

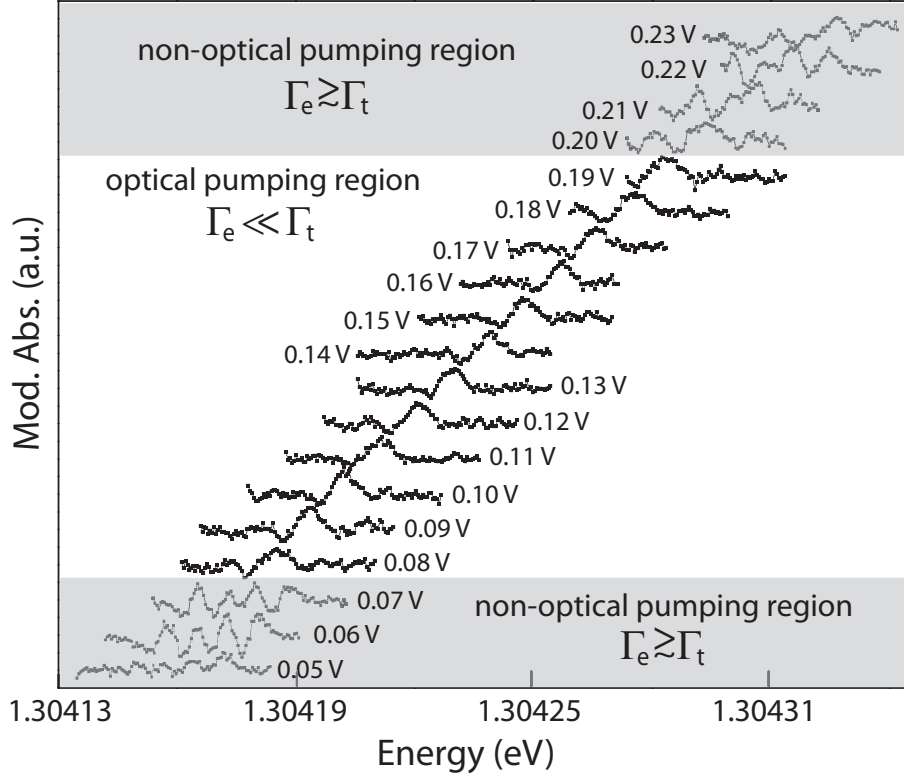


Figure 6.3: Characterization of the trion absorption range of QD #1 showing the optical pumping and non-optical pumping regions at an external magnetic field of 0.66 T.

The two cases illustrated in Figure 6.2 may be observed experimentally by characterizing the CW absorption range of the trion states of QD #1 in the presence of an externally applied magnetic field. These scans are plotted in Figure 6.3 for small voltage modulation at an external field of 0.66 T, showing both optical pumping and non-optical pumping regions. Non-optical pumping regions occur towards both ends of the absorption range due to the instability of the QD charge state that arises from the increased tunneling of unpolarized electrons back and forth between the QD and the n-doped GaAs layer at these voltages. This increased tunneling makes the spin relaxation rate comparable to the trion relaxation rate, enabling the observation of the “quartet pattern” in the trion absorption signal (Figure 6.2). To verify this, modulated absorption studies were performed in this region as a function of magnetic field strength to measure the separation between absorption peaks. These peak separations correspond to the electron and heavy-hole Zeeman splittings and are plotted

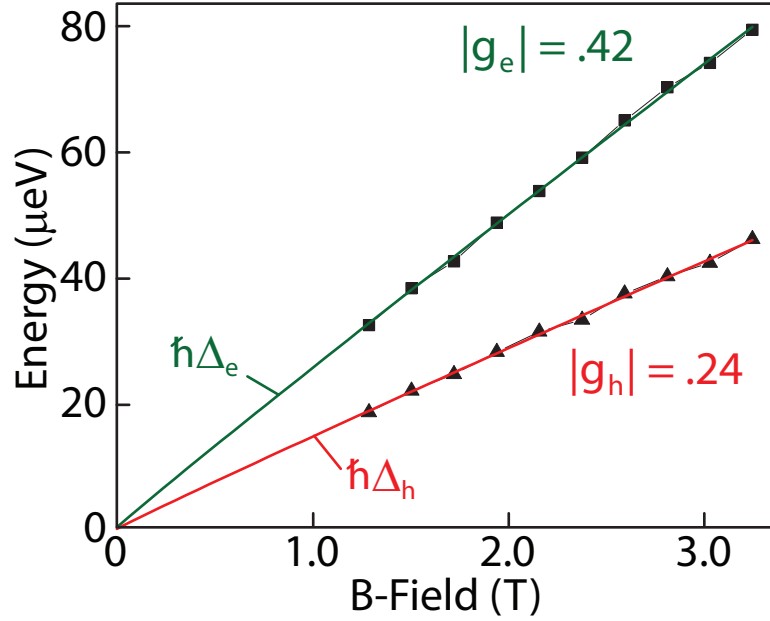


Figure 6.4: Electron and heavy-hole Zeeman splittings as a function of magnetic field. The Zeeman splittings are obtained by measuring absorption peak separations in the low-energy non-optical pumping region, yielding electron and heavy-hole g-factor values of 0.42 and 0.24, respectively.

in Figure 6.4. Electron and heavy-hole g-factor magnitudes of 0.42 and 0.24, respectively, are obtained from linear fits of the data, consistent with the values obtained from pump-probe studies performed with an external magnetic field in Section 4.6.

Towards the center of the absorption range of Figure 6.3 the QD charge state is stable, leading to a much slower spin relaxation rate. In this region, only one feature is observed due to the near degeneracy of the two “cross” transitions in the dot, leading to a bi-direction pumping that prevents complete depletion of either spin state. This observed feature also indicates the dependence of the electron and heavy-hole g-factors on the sample bias voltage, as these two transitions may be distinguished in the non-optical pumping regions. The absorption signals associated with the “vertical” transitions in the dot disappear in this region as their energies are sufficiently separated to allow optical pumping. Increasing the magnetic field beyond approximately 3 T leads to the complete disappearance of all absorption peaks in the optical pumping region, demonstrating the ability to initialize the spin by pumping any one of the trion transitions in the dot.

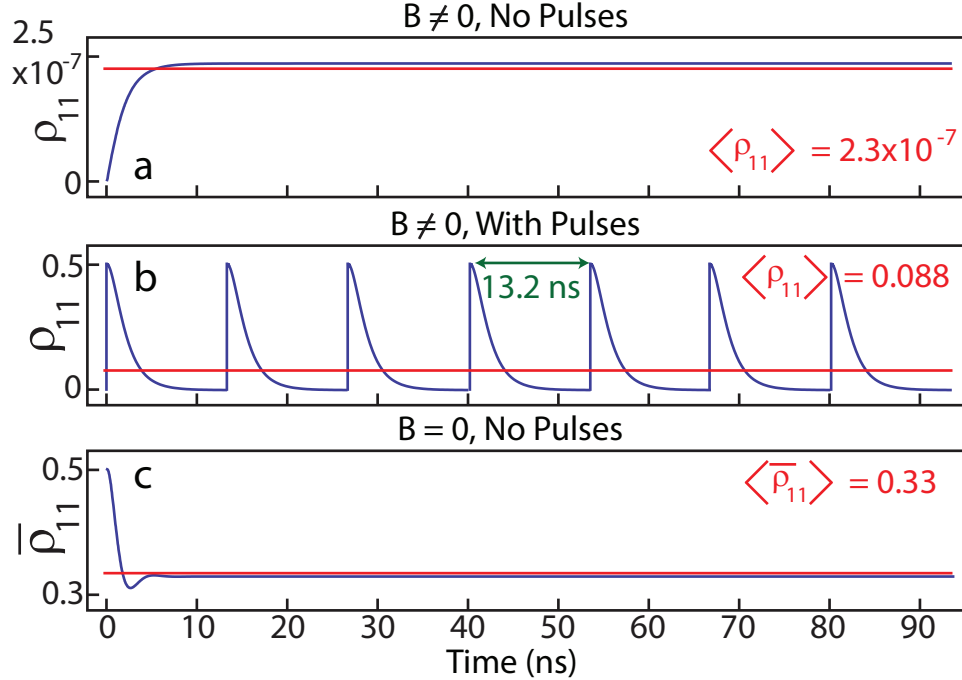


Figure 6.5: Calculated ρ_{11} values as a function of time for CW excitation of the $|1\rangle$ to $|4\rangle$ transition (a) without and (b) with an incident train of optical pulses for a nonzero magnetic field. (c) Calculated $\bar{\rho}_{11}$ values as a function of time for CW excitation of the $|\bar{1}\rangle$ to $|\bar{4}\rangle$ transition in the \hat{z} basis without an external field. The time averaged populations for all cases are indicated by the red curves.

6.2 Read-Out of Electron Spin Manipulations Via the CW Field

In the previous section, modulated absorption measurements with an externally applied magnetic field were able to distinguish between the case where the spin relaxation rate is comparable to or faster than the trion relaxation rate and the case where the spin relaxation rate is much slower than the trion relaxation rate. This is a consequence of the fact that modulated absorption signals provide a measure of the time-averaged absorption of the CW field or, more specifically, the time-averaged population in the $|1\rangle$ state, $\langle \rho_{11} \rangle$. We utilize this function of the CW field to evaluate the operation of external manipulations of the electron spin in the optical pumping region of the trion absorption.

To understand how the CW field can be used to detect the effect electron spin manipulations, we theoretically consider the time averaged $|1\rangle$ population in the op-

tical pumping region with and without an incident train of optical pulses exciting the dot. We take the repetition period of the pulses to be that of the laser (13.2 ns) and take each pulse to drive half the population in the $|2\rangle$ state back to the $|1\rangle$ state. As the laser repetition period is much longer than the characteristic timescale for optical pumping, the electron spin is completely re-initialized between pulses.

Theoretical calculations of ρ_{11} as a function of time are plotted for the two cases in Figures 6.5(a) and (b) for a CW trion Rabi frequency slightly less than the trion relaxation rate. Without the pulses, ρ_{11} approaches a steady-state value of 2.5×10^{-7} within a few nanoseconds due to the interplay between trion relaxation and spin relaxation, the latter assumed to occur on the order of 10 ms based on the observations of M. Kroutvar *et al* [115], yielding a time averaged population $\langle \rho_{11} \rangle = 2.3 \times 10^{-7}$. With the pulses, ρ_{11} population undergoes periodic excitation and decay cycles, dramatically increasing the time-averaged ρ_{11} value by several orders of magnitude to 0.088. This increase in the value of $\langle \rho_{11} \rangle$ is a direct consequence of the action of the pulses and reflects the amount of $|1\rangle$ population generated by each pulse. In this capacity, the CW field functions as an “optical tripwire” as it provides a measure of the population that reenters the $|1\rangle$ state post initialization.

To determine whether the pulse-induced increase in $\langle \rho_{11} \rangle$ is detectable, we compare the results of Figure 6.5(b) with simulations of zero-field studies without any pulses. Specifically, we calculate the time-averaged population $\bar{\rho}_{11}$ in the z-basis for the case where the $|\bar{1}\rangle$ to $|\bar{4}\rangle$ transition is driven by a CW field of the same power. The time-evolution of $\bar{\rho}_{11}$ is plotted in Figure 6.5(c), showing the system approaching the steady state value of approximately 0.32 after the trion decoherence time, yielding a time-averaged value of 0.33.

Based on these theoretical considerations and the signal strength of modulated absorption studies at zero-field, we expect that absorption studies with a magnetic field and an optical pulse train should yield detectable signals roughly an order of magnitude weaker than those at zero-field. Using this method of read-out we first pursue one-pulse studies comparing the operations of pulses of different polarizations and detunings to verify the ability to coherently control the electron spin with detuned

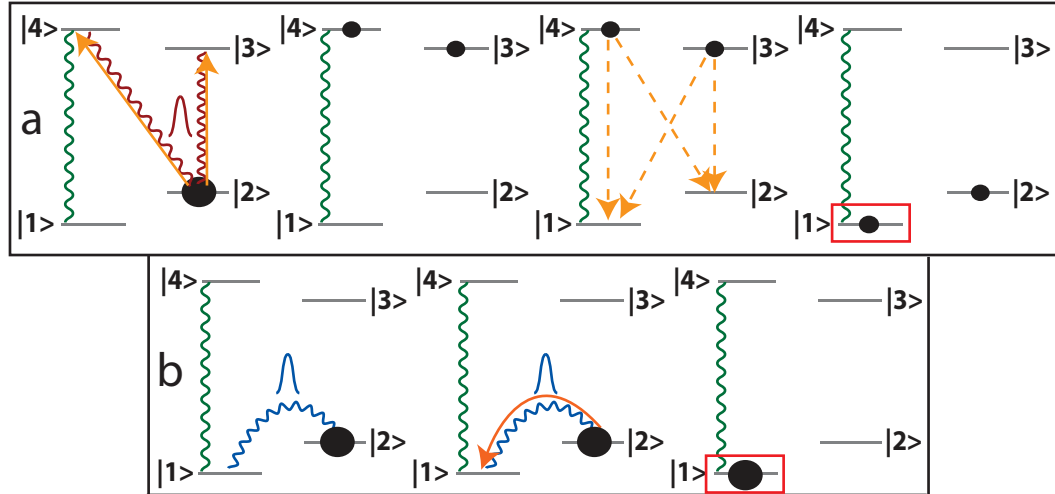


Figure 6.6: Illustrations of how $|1\rangle$ population is generated post initialization by (a) a 45° polarized pulse that drives π rotations for both trion transitions and (b) a $\hat{\sigma}_+$ polarized pulse that drives a π rotation between the electron spin states.

circularly polarized pulses.

6.3 One-Pulse Studies: Polarization and Detuning Dependence

In one-pulse studies we investigate the operation of 45° polarized $[1/\sqrt{2}(\hat{x} + \hat{y})]$ and circularly polarized $[\hat{\sigma}_+ = 1/\sqrt{2}(\hat{x} + i\hat{y})]$ pulses both on-resonance with the trion transitions and red-detuned from the trion transitions by 1 meV (roughly one pulse width). As the CW read-out method is sensitive to the amount of population generated in the $|1\rangle$ state after each pulse, there are two optically driven processes that will be detected by this method: the generation and decay of trion population and the driving of two-photon Raman transitions. Both of these processes are illustrated in Figures 6.6(a) and (b) and show how $|1\rangle$ population is generated in each case.

Both the 45° and circularly polarized pulses are capable of generating trion population that subsequently decays to both spin ground states. Assuming equal decay rates for all trion transitions, the amount of population generated in the $|1\rangle$ state after decay is the average of the populations generated in both trion states. For equal trion excitation, this is simply the population generated in one of the trion states. As a result, the detected modulated absorption signal in one pulse studies will show

an oscillatory dependence on the amplitude of each pulse due to pulse-driven Rabi oscillations between the initialized spin state and both trion states. As the amount of trion population generated by the pulses can be reduced by detuning them from the trion transitions, sufficient detuning leads to a negligible absorption signal.

As discussed in the previous Chapter, the two-photon Raman transitions that rotate the spin about the optical axis can only be driven by circularly polarized pulses; the destructive interference of the two two-photon quantum mechanical pathways prevents the use of linearly polarized pulses to rotate the spin about the optical axis. These two-photon spin rotations depend on the pulse amplitude but are not suppressed by detuning the pulses from the trion transitions. Thus, for studies with a single train of resonant linearly polarized pulses we expect to see an oscillation in the absorption signal as a function of pulse amplitude due to trion Rabi oscillations, while for the detuned case we expect to see a diminished absorption signal due to the suppression of trion generation. For studies with circularly polarized pulses, we expect the absorption signal to show a combination of trion and electron spin Rabi oscillations on resonance due to the fact that each pulse can drive both processes, while for the detuned case we expect an absorption signal due primarily to driven two-photon spin rotations.

Figure 6.7 shows both the theoretically calculated and experimental measured modulated absorption signals for one-pulse studies as a function of pulse amplitude and V_{DC} . Though not explicitly labeled, the highest values of the experimentally measured modulated absorption signals are an order of magnitude weaker than signals obtained in zero-field studies, as anticipated. Theoretical calculations are based on numerical solutions of the density matrix equations for the four level system and include a pulse amplitude dependent red-shift of the $|1\rangle$ to $|4\rangle$ transition energy as a result of pulse-generated carriers in the sample WL. Both theory and experiment show trion Rabi oscillations for linearly polarized excitation on resonance (upper left panels), though the experimentally observed trion Rabi oscillations are strongly damped. The cause of this damping is not well understood at present but may be the result of off-resonant coupling of the electron to continuum states in the WL [214].

Off-resonance (upper right panels), the trion population generated by the linearly polarized pulses is suppressed, leading to a negligible modulated absorption signal both in theory and experiment.

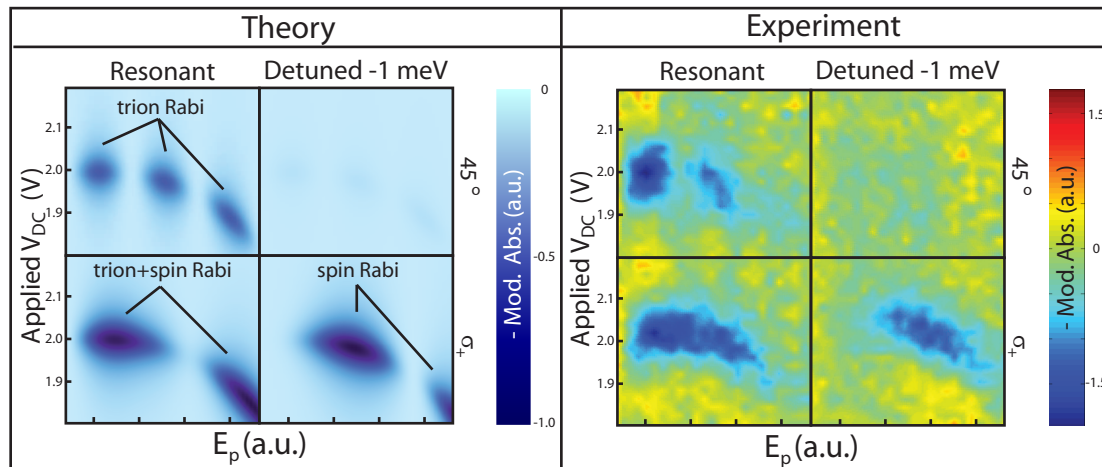


Figure 6.7: Theoretically calculated and experimentally measured modulated absorption signals as a function of pulse amplitude and V_{DC} . The results for both theory and experiment show trion Rabi oscillations for 45° polarized excitation on resonance (upper left panels), no absorption signal for a detuned 45° polarized pulse (upper right panels), trion and electron spin Rabi oscillations for $\hat{\sigma}_+$ polarized excitation on resonance (lower left panels) and approximately one complete spin Rabi oscillation for a detuned $\hat{\sigma}_+$ polarized pulse.

The modulated absorption signal in both theory and experiment for resonant circularly polarized pulses (lower left panels) shows a combination of trion and electron spin Rabi oscillations, as expected, with maximum spin rotations occurring when trion generation is minimized. As with linearly polarized excitation, detuning suppresses the amount of trion population generated, resulting in a modulated absorption signal due primarily to pulse driven spin Rabi oscillations (lower right panels), confirming the theoretical results of the Section 5.1.3. The slight discrepancy in the oscillation frequencies of the modulated absorption signals on and off resonance, though not well understood at present, may be the result of birefringence in the layers of the sample above the QDs. Such birefringence would lead to elliptically polarized pulses at the QD, reducing the effective two-photon pulse area and thus decreasing the spin Rabi oscillation frequency.

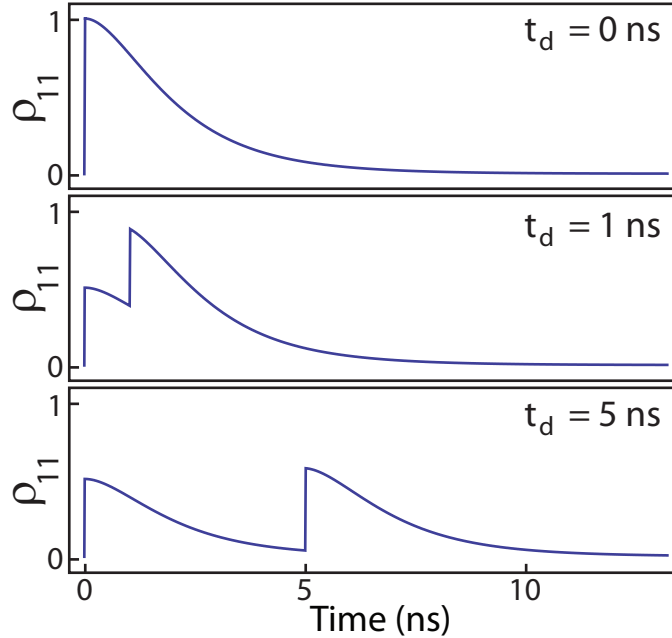


Figure 6.8: Calculations of the time evolution of the $|1\rangle$ population in two-pulse studies during each 13.2 ns period at different values of the pulse delay. Results show that for pulse delays as high as a few ns, the value of ρ_{11} returns to zero before the following pump pulse, signifying complete re-initialization of the electron spin between pulses.

Having confirmed the operation of detuned circularly polarized pulses on the electron spin, we now turn to two-pulse studies that enable the observation of the other spin control mechanisms in the system.

6.4 Two-Pulse Studies: Spin Precession about the Magnetic Field

We consider the operation of two time-delayed circularly polarized pulses that are detuned $500 \mu\text{eV}$ to the red of the trion transitions. For both pump and probe pulse trains, the two-photon pulse area for each pulse is set to correspond to a $\pi/2$ rotation of the spin about the \hat{z} axis. The pump pulse serves to rotate the initialized spin vector to lie along $+\hat{y}$. Completely perpendicular to the external magnetic field, the spin vector then precesses clock-wise about the \hat{x} axis at a rate determined by the Zeeman splitting between the electron spin states. As a result of the precession, the component of the electron spin vector along $+\hat{x}$ —which reflects the $|1\rangle$ population—immediately after the probe pulse will depend on the orientation of the spin vector

immediately before its arrival.

In addition, while the electron spin precesses about the magnetic field the CW field drives Rabi oscillations between the $|1\rangle$ and $|4\rangle$ states at a rate determined by the CW trion Rabi frequency, imparting a geometric phase to the $|1\rangle$ state for each complete trion Rabi oscillation as discussed in Section 5.3. Thus, to isolate the effect of spin precession, we first limit the pulse delay range to values much shorter than the CW trion Rabi period. This also ensures that the CW field completely re-initializes the electron spin between pulse pairs (Figure 6.8), permitting the standard modulated absorption approach.

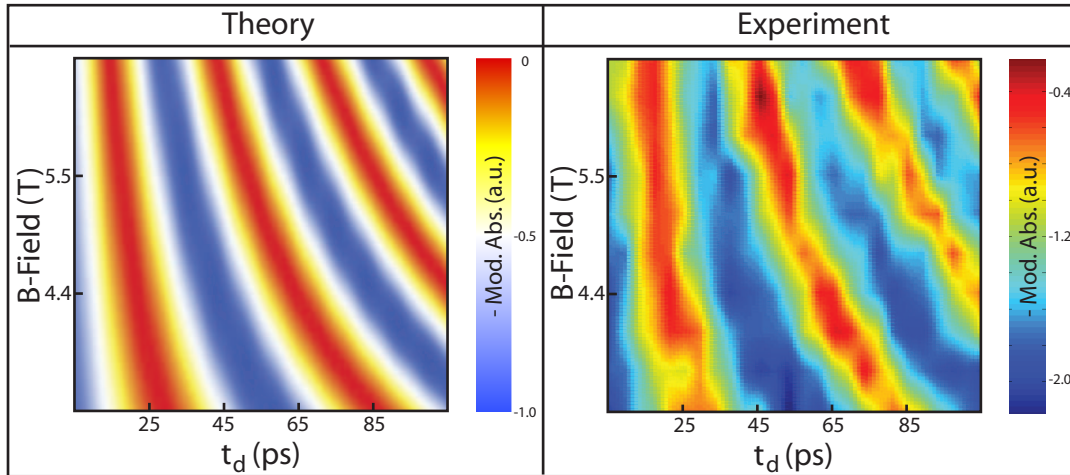


Figure 6.9: Theoretical and experimentally measured modulated absorption signals as a function of pulse delay and magnetic field. The oscillatory behavior of the signal is clearly exhibited, with the oscillation frequency increasing as the magnetic field is increased in strength.

Figure 6.9 plots the calculated and experimentally measured modulated absorption signals as a function of pulse delay and external magnetic field, clearly exhibiting the oscillatory dependence of the modulated absorption signal on t_d in both theory and experiment. From these scans we extract an electron g-factor magnitude of ~ 0.4 , consistent both with the CW studies presented in Section 6.1 and the pump-probe studies of Section 4.6. A single modulated absorption scan as a function of pulse delay is plotted in Figure 6.10, indicating the orientation of the electron spin vector immediately before the probe pulse at selected delay points.

The sequence of operations $U_p(\pi/2)U_B(\phi)U_p(\pi/2)$ executed by the pulses and

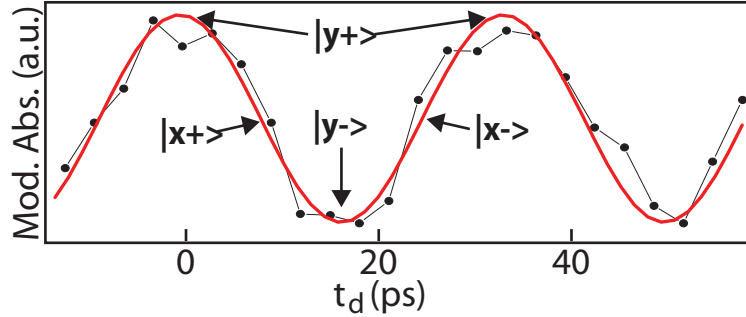


Figure 6.10: Modulated absorption scan and oscillatory fit (red curve) as a function of pulse delay for an external magnetic field of 5.5 T. The orientation of the electron spin vector immediately before the probe pulse is indicated at selected delay values.

magnetic field in two-pulse studies for short pulse delays can be used to construct different gate operations depending on the precession angle ϕ . For $\phi = 2\pi n$ ($|\Psi_y^e\rangle = |y+\rangle$) U_B reduces to the identity matrix, resulting in an X gate while for $\phi = \pi + 2\pi n$ ($|\Psi_y^e\rangle = |y-\rangle$) the entire sequence reduces to the identity matrix. The Hadamard gate may be constructed using precession angles of either $\frac{\pi}{2} + 2\pi n$ ($|\Psi_x^e\rangle = |x+\rangle$) or $\frac{3\pi}{2} + 2\pi n$ ($|\Psi_x^e\rangle = |x-\rangle$). In addition, rotations about the \hat{y} axis by an angle ϕ may be achieved by switching the helicity of the first or the second pulse.

6.5 Two-Pulse Studies: Geometric Phases and Spin Precession Modulation

Two-pulse studies with higher CW powers and longer pulse delay ranges enable the observation of the CW field operation between pulses. After the operation of the pump pulse, the CW field begins driving Rabi oscillations between the $|1\rangle$ and $|4\rangle$ states while the electron spin precesses about the magnetic field. The evolution of the system between the pump pulse and the first π rotation of the trion transition driven by the CW field is illustrated in Figure 6.11 for a precession frequency much greater than the trion Rabi frequency. During the early stages of the CW-driven trion Rabi oscillation, the electron spin precesses in the \hat{y} - \hat{z} plane. As more of the $|1\rangle$ population is driven to the $|4\rangle$ state, however, an increasingly large heavy-hole spin vector is generated along $+\hat{x}$ and the electron spin vector begins to trace out a cone

whose tip and base lie, respectively, at the origin and beneath the \hat{y} - \hat{z} plane. The height of this cone continues to grow while its base continues to shrink in diameter until all the $|1\rangle$ population is driven to the $|4\rangle$ state, at which point the diameter of the precession cone base becomes zero and the electron and heavy-hole spin vectors are oppositely aligned along the \hat{x} axis. Here, the electron spin does not precess since it is in a stationary state. Beyond this point, the CW field drives population back to the $|1\rangle$ state, repeating the process in reverse until the electron spin is once again precessing in the \hat{y} - \hat{z} plane.

As the CW field is resonant with the $|1\rangle$ to $|4\rangle$ transition, the net effect of the geometric phase imparted with each complete trion Rabi oscillation can be represented in terms of the unitary transformation

$$U_{cw} = \begin{bmatrix} -1 & 0 \\ 0 & 1 \end{bmatrix} \quad (6.1)$$

corresponding to a π rotation of the spin about the \hat{x} axis that manifests as a net π phase shift in the spin precession signal. In actuality, the phase shift in the spin precession signal occurs at the points where the $|1\rangle$ population is completely depleted by the CW field, but because of the trion population the effect of the geometric phase is only unitary for each complete trion Rabi oscillation. In modulated absorption studies as a function of pulse delay, then, we expect to see a spin precession signal modulated at the trion Rabi frequency, with π phase shifts in the spin precession signal occurring at times when the $|1\rangle$ population has been completely depleted by the CW field.

Calculated $|1\rangle$ populations immediately after the second pulse and experimentally measured modulated absorption signals as a function of pulse delay at different CW powers are shown in Figure 6.12. The modulation of the spin precession signal is clearly evident both in theory and in experiment, with the frequency of the modulation envelope increasing with increasing CW power as expected. The π phase shifts in the spin precession signal arising from the imparted geometric phases are also evident when comparing the 5 mW and 10 mW scans with the .2 mW scan. Near zero-delay (first green dashed line) the scans are all in phase. Around 200 ps (second green

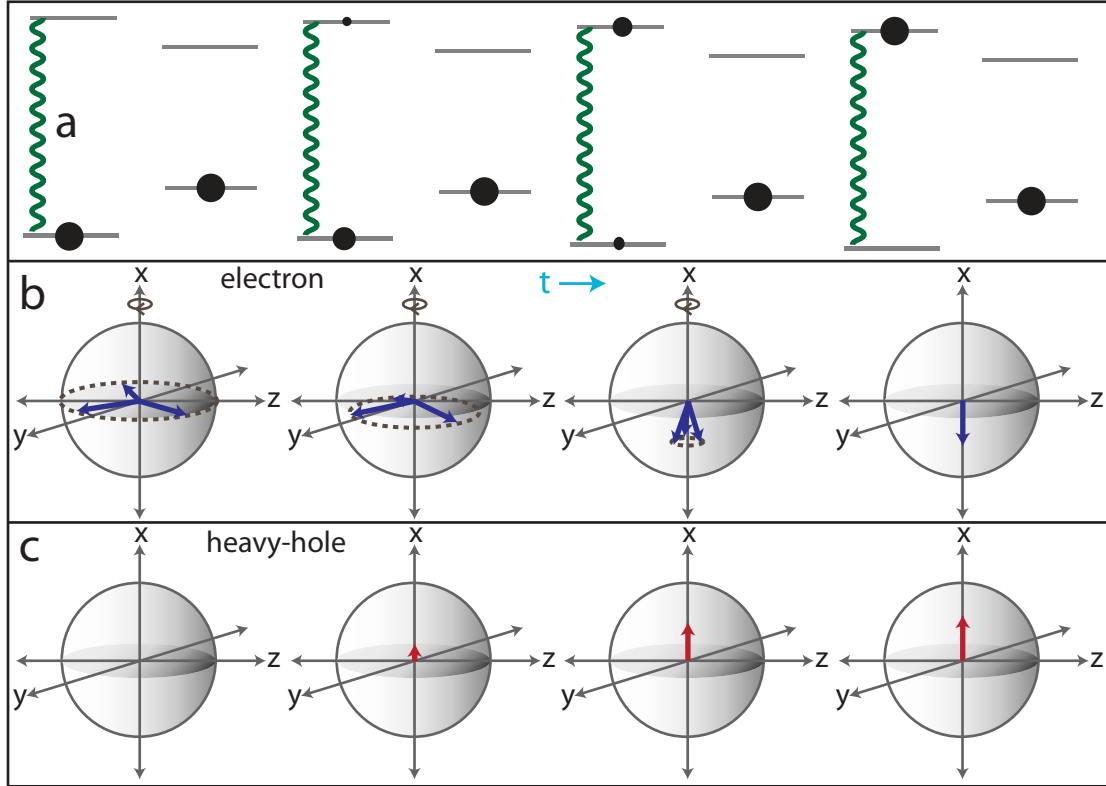


Figure 6.11: Diagrams illustrating the time evolution of (a) level occupations in the \hat{x} basis, (b) the electron spin vector and (c) the heavy-hole spin vector between the pump pulse and the first CW-driven π rotation of the $|1\rangle$ to $|4\rangle$ transition.

dashed line) the 5 mW and 10 mW scans have each passed a $|1\rangle$ depletion point, resulting in a π phase shift of those two precession signals with respect to the .2 mW precession signal, which has not approached a depletion point. Near 350 ps (third green dashed line), the 5 mW and 10 mW scans have passed through an even number of $|1\rangle$ depletion points, bringing their spin precession signals back in phase with the .2 mW spin precession signal, which has still not passed through any depletion points.

We note that for a trion Rabi oscillation period equal to an integer number of spin precession periods, the combination of pulses and geometric phases may be used to construct a number of optically driven single qubit gates. The red circles in Fig. 6.12 indicate cases where this condition is approximately met. At these points, the total operation sequence constitutes an optically driven Z or Y gate depending on whether the second $\pi/2$ pulse is $\hat{\sigma}_+$ or $\hat{\sigma}_-$ polarized.

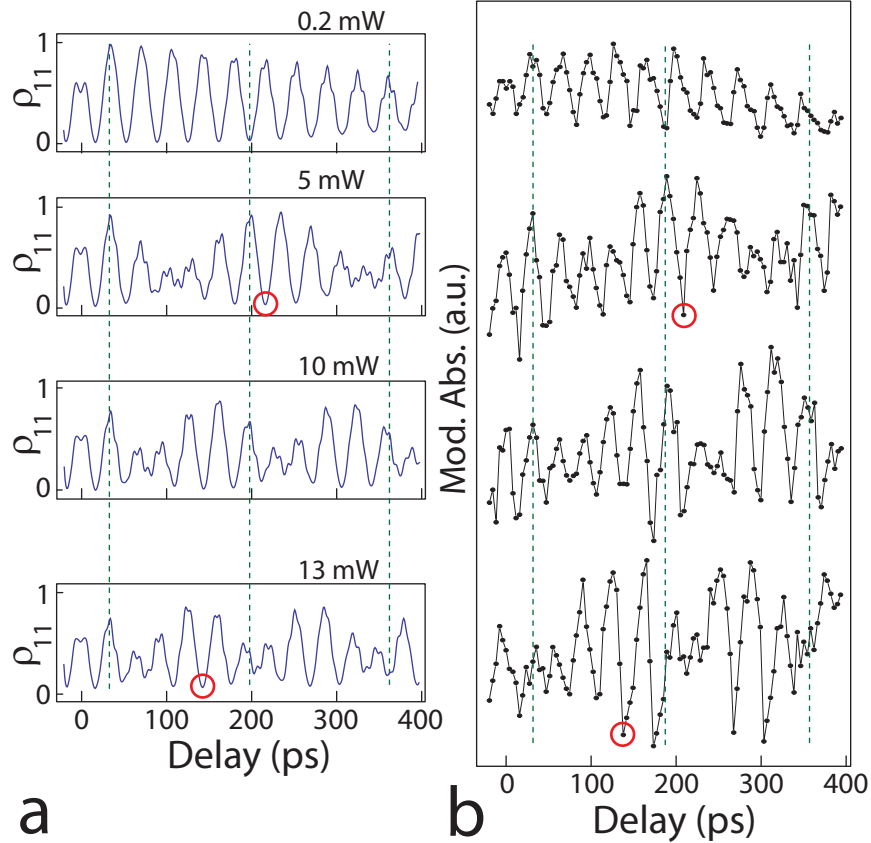


Figure 6.12: (a) Theoretically calculated values of ρ_{11} immediately after the probe pulse for different CW powers and (b) the corresponding modulated absorption scans at those powers. The green dashed lines serve as guides to the eye in comparing the precession signals at different CW powers. The red circles indicate conditions where the CW-driven trion Rabi period is approximately equal to an integer number of electron spin precession periods, enabling the construction of purely optical spin gates.

One peculiarity with the data of Figure 6.12 is that the spin precession signal until the first depletion point is weaker and less modulated than at later delays. The cause of this peculiarity is not clear and does not appear to be the result of systematic errors in the experimental method, e.g. delay stage misalignment or drift, etc. Though a reduced modulation of the first depletion point would occur as a result of detuning the CW field from the $|1\rangle$ to $|4\rangle$ transition, this seems an unlikely explanation as such a detuning would also change the imparted geometric phase, resulting in a reduced phase shift in the spin precession signal relative to lower power scans. Nevertheless, the overall agreement between theory and experiment in Figure 6.12 demonstrates

the ability to utilize the effect of geometric phases generated by cyclic excitations in the QD system to manipulate the electron spin.

6.6 Chapter Summary

In this Chapter we have discussed experiments demonstrating the coherent control of an initialized electron spin. Preparation of the electron spin in a pure state was accomplished by tuning a narrow-bandwidth CW field to the $|1\rangle$ to $|4\rangle$ transition in the dot, thereby optically pumping all spin population to the $|2\rangle$ state. Use of the same CW field to detect spin manipulations was also discussed, showing that this method of readout is sensitive to the $|1\rangle$ population generated by each pulse in a pulse train. This method of read-out was applied to one-pulse studies to verify the polarization dependence of the two-photon Raman excitations that rotate the spin about the optical axis, showing coherent control of the electron spin with detuned circularly polarized pulses. Pump-probe studies with two two-photon $\pi/2$ pulses were then presented, first demonstrating the ability to detect the effect of spin precession. The operation of the CW field on the electron spin between the pulses was then shown to manifest in part as a modulation of the spin precession signal. The geometric phases generated by cyclic evolutions of the system resulting from CW-driven trion Rabi oscillations were observed as π phase shifts in the electron spin precession signal, demonstrating the ability to control the electron spin via these geometric phases.

CHAPTER 7

Proposed Future Experiments

The previous Chapters have demonstrated the coherent optical spectroscopy of a single, negatively charged InAs QD and the coherent optical control of the QD confined electron spin. The ability to coherently probe and control the spin states of a single QD confined charge is a foundational prerequisite for executing quantum algorithms in scalable architectures based on the spin states of such charges. The impetus now is for the advancement of both technology and technique, i.e. effective and efficient methods of performing multi-qubit operations and entangling multiple spin qubits, though most of the onus currently lies with the advancement of semiconductor device fabrication to allow for these methods to be developed [215]. To this end, a number of approaches have strived towards the growth of laterally [216] and vertically [217] coupled dot structures. In addition, devices combining such structures with photonic crystal cavities [218] or microtoroidal resonators [219] for the development of quantum networks akin to those proposed in Reference [42] are also being developed and may soon be realized.

Until the development of such structures, there still remain a number of experimental studies in the singly charged QD system that are important from a quantum computing perspective. In this Chapter, two of these experimental studies are discussed: the density matrix tomography (DMT) of a single electron spin confined in a QD and the generation of geometric phases in a singly charged QD with optical pulses. The motivation for each proposed experiment is presented, as well as the experimental requirements and challenges.

7.1 Density Matrix Tomography (DMT) of a QD Confined Electron Spin

DMT is the experimental procedure by which the elements of a quantum system's density matrix are determined under a particular set of conditions. This procedure is important for quantum computing as it allows for the evaluation of quantum gate fidelities which, in conjunction with characterized measurement fidelities, would be used to determine the number of repeated computations or redundantly encoded qubits required to obtain a reliable measurement from a particular computing operation [3]. In this Section, we first discuss how the combination of a detuned circularly polarized pulse and spin precession may be used to characterize a given system's density matrix for optical tripwire readout. A possible scheme for read-out signal calibration is then presented, by which numerical values for the density matrix elements may be determined. Finally, an example procedure evaluating the operation of a Hadamard gate is discussed.

7.1.1 DMT Procedure: Theory

As in the previous two Chapters, we consider the case where a DC magnetic field is applied in the Voigt configuration. Using the standard labeling scheme, we seek the values of the density matrix elements for a general electron spin density matrix

$$\rho_{el} = \begin{bmatrix} \rho_{11} & \rho_{12} \\ \rho_{21} & \rho_{22} \end{bmatrix} \quad (7.1)$$

specified at some time $t = t_0$. To do this, we once again utilize the formalism of the spin Bloch sphere in $\{u, v, w\}$ space for the case of excitation with a detuned circularly polarized pulse (Section 5.1.2) with

$$\mathbf{B}(t = t_0) = \begin{bmatrix} B_u(t_0) = B_{u,0} \\ B_v(t_0) = B_{v,0} \\ B_w(t_0) = B_{w,0} \end{bmatrix} = \begin{bmatrix} 2\text{Re}[\rho_{12}] \\ -2\text{Im}[\rho_{12}] \\ \rho_{22} - \rho_{11} \end{bmatrix} \quad (7.2)$$

$$\mathbf{\Omega} = \begin{bmatrix} \Omega_u \\ \Omega_v \\ \Omega_w \end{bmatrix} = \begin{bmatrix} -\text{Re} [ie^{-i\phi}] \frac{\Omega_p^2}{2\delta_p} \text{sech}^2 \left(\frac{t-t_p}{\tau} \right) \\ 0 \\ \Delta_e \end{bmatrix} \quad (7.3)$$

$$d\mathbf{B}/dt = \mathbf{\Omega} \times \mathbf{B} \quad (7.4)$$

where $t_p > t_0$ is the arrival time of the pulse and we note that the tildes have been removed from the density matrix elements since the Schrödinger picture and FIP (Section 5.1.1) probability amplitudes for the electron spin states are equivalent. Equation 7.4 yields the system of equations

$$\dot{B}_u = -\Delta_e B_v \quad (7.5)$$

$$\dot{B}_v = \Delta_e B_u + \frac{\Omega_p^2}{2\delta_p} \text{sech}^2 \left(\frac{t-t_p}{\tau} \right) B_w \quad (7.6)$$

$$\dot{B}_w = -\frac{\Omega_p^2}{2\delta_p} \text{sech}^2 \left(\frac{t-t_p}{\tau} \right) B_v \quad (7.7)$$

which can be solved using the same approach employed in Sections 5.1.3 and 5.2, i.e. by treating the pulse and magnetic field operations separately (a valid approach as long as the pulse duration is much shorter than the spin precession period). Solutions to Equations 7.5-7.7 enable the expression of each type of operation in terms of a unitary rotation matrix, just as in Chapter 5:

$$\text{pulse: } R_p(\theta) = \begin{bmatrix} 1 & 0 & 0 \\ 0 & \cos(\theta) & \sin(\theta) \\ 0 & -\sin(\theta) & \cos(\theta) \end{bmatrix}, \quad \theta = \frac{\Omega_p^2 \tau}{\delta_p} \quad (7.8)$$

$$\text{B-field: } R_B(\vartheta) = \begin{bmatrix} \cos(\vartheta) & -\sin(\vartheta) & 0 \\ \sin(\vartheta) & \cos(\vartheta) & 0 \\ 0 & 0 & 1 \end{bmatrix}, \quad \vartheta = \Delta_e(t-t_0). \quad (7.9)$$

where the pulse and the magnetic field each execute, respectively, instantaneous rotations about \hat{u} and time-dependent rotations about \hat{w} of the spin Bloch vector. We note that the rotation matrices of Equations 7.8 and 7.9 alternatively could have been determined by phenomenologically re-expressing each $\{x, y, z\}$ space operation

in terms of the corresponding $\{u, v, w\}$ space operation. The brute force approach employed here was pursued for rigorously.

To determine the values of the density matrix elements, we utilize the fact that the spin Bloch vector precesses about the \hat{w} axis of the Bloch sphere and excite the system with the detuned circularly polarized pulse at different moments during the precession. This effectively rotates different components of the spin Bloch vector to lie along the \hat{w} axis, which serves as the measurement axis in experiments utilizing optical tripwire read-out as this method effectively measures the component of the spin Bloch vector projected along \hat{w} . For the same experimental configuration as in the previous Chapter, optical tripwire read-out provides a signal proportional to the population in the $|1\rangle$ state immediately after the pulse. We thus consider the form of the $|1\rangle$ population ρ'_{11} after the operation of both the magnetic field and the detuned circularly polarized pulse, in that order. In other words, we consider the transformation

$$\mathbf{B}' = R_p(\theta)R_B(\vartheta)\mathbf{B}(t = t_0) \quad (7.10)$$

$$\begin{bmatrix} B'_u \\ B'_v \\ B'_w \end{bmatrix} = \begin{bmatrix} B_{u,0} \cos(\vartheta) - B_{v,0} \sin(\vartheta) \\ B_{u,0} \cos(\theta) \sin(\vartheta) + B_{v,0} \cos(\theta) \cos(\vartheta) + B_{w,0} \sin(\theta) \\ -B_{u,0} \sin(\theta) \sin(\vartheta) - B_{v,0} \sin(\theta) \cos(\vartheta) + B_{w,0} \cos(\theta) \end{bmatrix} \quad (7.11)$$

and assume that all population remains in the spin ground states throughout the transformation. The $|1\rangle$ population after the pulse then has the form

$$\begin{aligned} \rho'_{11} &= \frac{1}{2}(1 - B'_w) \\ &= \frac{1}{2}[1 + B_{u,0} \sin(\theta) \sin(\vartheta) + B_{v,0} \sin(\theta) \cos(\vartheta) - B_{w,0} \cos(\theta)]. \end{aligned} \quad (7.12)$$

From Equation 7.12 we see that different components of the spin Bloch vector at $t = t_0$ can be isolated in the read-out signal by proper selection of the two-photon pulse area and the spin precession angle. Trivially, the diagonal density matrix elements may be determined without using either spin precession or an optical pulse, as for $\theta = 0$ and $\vartheta = 0$, $\rho'_{11} = \rho_{11}$. The off-diagonal matrix elements of ρ_{el} may be determined

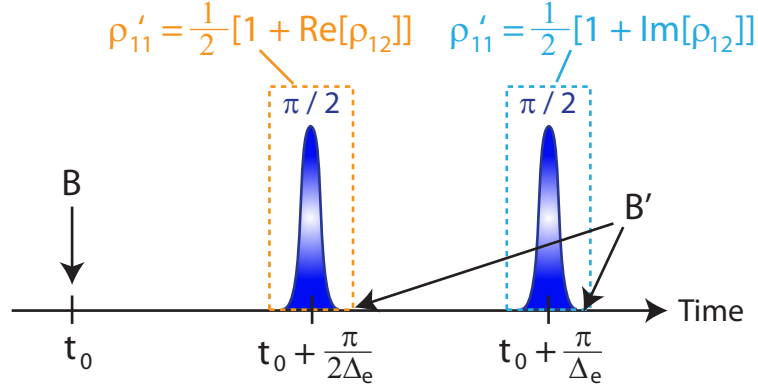


Figure 7.1: $|1\rangle$ population immediately after the operation of a $\theta = \pi/2$ pulse at times corresponding to a $\pi/2$ and a π precession of the electron spin.

with the use of a $\theta = \pi/2$ pulse, yielding a $|1\rangle$ population of the form

$$\rho'_{11} = \begin{cases} \frac{1}{2} [1 + 2\text{Re}[\rho_{12}]], & \vartheta = \pi/2 + 2n\pi \\ \frac{1}{2} [1 + 2\text{Im}[\rho_{12}]], & \vartheta = \pi + 2n\pi \end{cases} \quad (7.13)$$

Equation 7.13 shows how proper selection of the precession angle allows for the isolation of either the real or the imaginary part of ρ_{12} , as illustrated in Figure 7.1. The value of ρ_{21} is then determined simply by taking the complex conjugate of ρ_{12} . The general DMT procedure for a density matrix given at $t = t_0$ is then

1. Determine ρ_{11} through direct optical tripwire read-out.
2. Determine ρ_{22} either by utilizing population conservation or by performing optical tripwire read-out on state $|2\rangle$.
3. Determine the real part of ρ_{12} by reading out the result of a two-photon $\pi/2$ pulse applied at $\Delta_e(t - t_0) = \pi/2$ (orange dashed box in Figure 7.1).
4. Determine the imaginary part of ρ_{12} by reading out the result of a two-photon $\pi/2$ pulse applied at $\Delta_e(t - t_0) = \pi$ (light blue dashed box in Figure 7.1).
5. Determine ρ_{21} from the complex conjugate of ρ_{12} .

The experimental procedure above allows for the complete determination of the electron spin density matrix at any particular time t_0 with the use of $\pi/2$ pulses

applied at times $t = t_0 + \frac{\pi}{2\Delta_e}$ and $t_0 + \frac{\pi}{\Delta_e}$. With the procedure determined, we now discuss how experimentally measured optical tripwire signals may be calibrated to assign numerical values to the density matrix elements.

7.1.2 Experimental Calibration

To reliably extract numbers from DMT experiments, measured signals must be accurately calibrated. This generally involves correlating measured signal levels with specific spin operations. For the case of spin precession, such assignments may be made in a straightforward manner, as the two pulse studies presented in Section 6.4 allow simple determination of the precession angle as a function of time.

For the two-photon spin rotation performed by the detuned circularly polarized pulse, power dependent one-pulse studies with optical tripwire read-out (Section 6.3) may be used to determine the specific pulse power corresponding to a π rotation of the spin. To assign population values to a particular signal level, studies may then be performed with two π pulses separated in delay by a complete 2π spin precession to determine the actual amount of population rotated by each π pulse. The maximum signal level in such studies would provide a measure of the amount of population left undriven by each π pulse when compared to the maximum signal level in studies performed with a single π pulse. The situation is illustrated in Figure 7.2, depicting absorption measurements with one and two π pulses that yield maximum signals of α and β , respectively. The actual amount of population rotated by a π pulse, ρ_π , is given by the expression

$$\rho_\pi = 1 - \frac{\beta}{2\alpha} \quad (7.14)$$

and can be used to assign population values to particular signal levels. For instance, if a $\pi/2$ pulse (based on one-pulse studies) leads to a maximum modulated absorption signal κ , then the actual population rotated by the $\pi/2$ pulse is

$$\rho_{\pi/2} = \frac{\kappa}{\alpha} \rho_\pi \quad (7.15)$$

and so forth. Using this calibration scheme, optical tripwire measurements may be

assigned population values from which the density matrix elements may be determined.

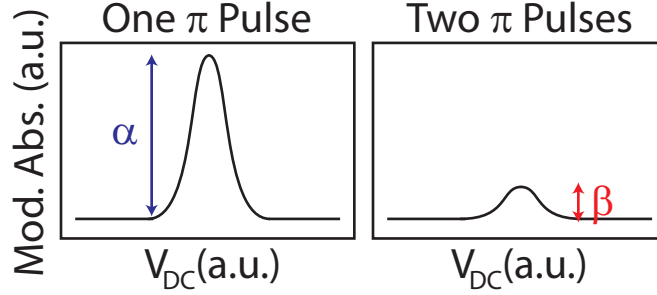


Figure 7.2: Example modulated absorption scans in experiments with one and two two-photon π pulses, with maximum signals α and β , respectively.

7.1.3 DMT Procedure for the Hadamard Gate

Here we provide a possible experimental procedure for performing DMT of the Hadamard gate

$$H = \frac{1}{\sqrt{2}} \begin{bmatrix} 1 & 1 \\ 1 & -1 \end{bmatrix} \quad (7.16)$$

which, from the fourth row of Table 5.1, corresponds to the sequence of rotations

$$R_{had} = R_p(\pi/2)R_B(\pi/2)R_p(\pi/2). \quad (7.17)$$

The density matrix resulting from the operation of the Hadamard gate will depend on the orientation of the electron spin immediately before the operation. For initial spin orientations along $\pm\hat{x}$, the resultant density matrix has the form

$$\rho_{el} = \begin{cases} \begin{bmatrix} 1/2 & 1/2 \\ 1/2 & 1/2 \end{bmatrix}, & |\Psi_x^e(t_0)\rangle = |x+\rangle \\ \begin{bmatrix} 1/2 & -1/2 \\ -1/2 & 1/2 \end{bmatrix}, & |\Psi_x^e(t_0)\rangle = |x-\rangle \end{cases}, \quad (7.18)$$

thus, to truly verify Hadamard gate operation, we perform density matrix tomography for each initial spin orientation. We first treat the case where the CW field initializes

all population to the $|2\rangle$ state. Optical tripwire read-out for the sequence given in Equation 7.17 leads to a signal ξ_1 , from which we extract

$$\rho_{11} = \frac{\xi_1}{\alpha} \rho_\pi, \quad \rho_{22} = 1 - \rho_{11} \quad (7.19)$$

using the same calibration constants provided previously. Signal values ξ_2 and ξ_3 are then obtained in performing steps 3 and 4 of the DMT procedure, yielding

$$\phi = \frac{\pi}{2} : \text{Re}[\rho_{12}] = \frac{1}{2} \left[2 \frac{\xi_2}{\alpha} \rho_\pi - 1 \right] \quad (7.20)$$

$$\phi = \pi : \text{Im}[\rho_{12}] = \frac{1}{2} \left[2 \frac{\xi_3}{\alpha} \rho_\pi - 1 \right]. \quad (7.21)$$

The total density matrix in this case may then be constructed as

$$\rho_{el} = \begin{bmatrix} \frac{\xi_1}{\alpha} \rho_\pi & \frac{1}{2} [2 \frac{\xi_2}{\alpha} \rho_\pi - 1] + \frac{i}{2} [2 \frac{\xi_3}{\alpha} \rho_\pi - 1] \\ \frac{1}{2} [2 \frac{\xi_2}{\alpha} \rho_\pi - 1] - \frac{i}{2} [2 \frac{\xi_3}{\alpha} \rho_\pi - 1] & 1 - \frac{\xi_1}{\alpha} \rho_\pi \end{bmatrix}. \quad (7.22)$$

In repeating this process for the case where the CW field initializes the electron spin to the $|1\rangle$ state, the optical tripwire in this case measures the $|2\rangle$ population, resulting in a minus sign between the bracketed terms of Equation 7.13. For the measured signals ζ_1 , ζ_2 and ζ_3 (ξ_1 , ξ_2 and ξ_3 analogues) the total density matrix is

$$\rho_{el} = \begin{bmatrix} 1 - \frac{\zeta_1}{\alpha} \rho_\pi & \frac{1}{2} [1 - 2 \frac{\zeta_2}{\alpha} \rho_\pi] + \frac{i}{2} [1 - 2 \frac{\zeta_3}{\alpha} \rho_\pi] \\ \frac{1}{2} [1 - 2 \frac{\zeta_2}{\alpha} \rho_\pi] - \frac{i}{2} [1 - 2 \frac{\zeta_3}{\alpha} \rho_\pi] & \frac{\zeta_1}{\alpha} \rho_\pi \end{bmatrix}. \quad (7.23)$$

The differences between the two constructed density matrices will reflect the critical sign difference between the elements in the second column of the Hadamard operation (Equation 7.16), thereby verifying its operation.

The general procedure discussed here may be applied to any single qubit gate or sequence of gates and would prove an indispensable technique for evaluating the fidelities of such operations. This procedure could be improved by gating the CW field using electro-optic modulators so that it only operates for initialization and read-out. Such modulation would eliminate any reduction of measured gate fidelities due to trion Rabi oscillations driven by the CW field during the course of operations. Further improvement would be realized with the use of optical cycling read-out [53, 213] to provide improved signal to noise.

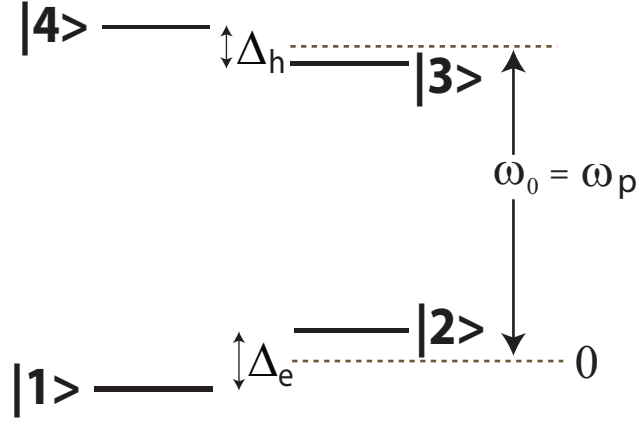


Figure 7.3: Energy level diagram showing the tuning of the \hat{x} polarized pulse used to generate the geometric phases for spin control.

7.2 Pulse-Generated Geometric Phases for Spin Rotation

The previous two Chapters demonstrated in both theory and experiment that the generation of geometric phases by optically driven cyclic evolutions in the QD can be used to rotate the electron spin about an axis orthogonal to the optical axis. The cyclic evolutions in this case were driven by the same CW field used to initialize the spin. This method of driving the cyclic evolutions is not optimal as the rotations occur continually and require high powers to obtain fast operation times. Ideally, the geometric phases used for spin rotation would be generated by separate pulses, enabling operations at particular times during the course of the computation. Here, we propose experiments with a linearly polarized optical pulse to perform the geometric phase induced spin rotation, following the proposed approach of Reference [133]. The unitary transformation matrix associated with the operation of such a pulse is first derived, followed by the discussion of a possible experimental procedure for the realization of these rotations.

7.2.1 Derivation of the Unitary Transformation Matrix

For experiments, we specifically consider excitation with an optical pulse polarized

along \hat{x} and incident along the optical axis of the form

$$\mathbf{E}_p(t) = \hat{x} \frac{1}{2} E_p \operatorname{sech} \left(\frac{t}{\tau} \right) [e^{-i\omega_p t} + c.c.]. \quad (7.24)$$

Since we are interested in determining the unitary transformation associated with the spin rotation, we solve for the probability amplitudes of the system using the same approach as in Chapter 5. In this case, the linearly polarized pulse leads to the nonzero dipole interaction matrix elements

$$V_{14} = -\frac{\hbar\Omega_p}{2} \operatorname{sech} \left(\frac{t}{\tau} \right) [e^{-i\omega_p t} + c.c.] = V_{41} = V_{23} = V_{32}. \quad (7.25)$$

Immediately, we note that for an optical pulse bandwidth comparable to the electron and heavy-hole Zeeman splittings, the driving of *both* transitions in the dot must be considered. We recall that the sign of the geometric phase imparted by a CW field depends on the sign of the detuning from the optically driven transition. Thus, the pulse is centered in frequency between the two transition energies, i.e. ω_p is set equal to ω_0 in Figure 7.3. In this case, the optical pulse imparts equal and opposite geometric phases to the probability amplitudes of the electron spin states as the pulse detunings from the \hat{x} polarized transitions have opposite signs. Under these conditions, the equations of motion in the interaction picture [$C_i(t) = \tilde{C}_i(t)e^{-i\omega_i t}$] are

$$\dot{\tilde{C}}_1(t) = \frac{i\Omega_p}{2} e^{-i\Delta t} \operatorname{sech}(\sigma t) \tilde{C}_4(t) \quad (7.26)$$

$$\dot{\tilde{C}}_2(t) = \frac{i\Omega_p}{2} e^{i\Delta t} \operatorname{sech}(\sigma t) \tilde{C}_3(t) \quad (7.27)$$

$$\dot{\tilde{C}}_3(t) = \frac{i\Omega_p}{2} e^{-i\Delta t} \operatorname{sech}(\sigma t) \tilde{C}_2(t) \quad (7.28)$$

$$\dot{\tilde{C}}_4(t) = \frac{i\Omega_p}{2} e^{i\Delta t} \operatorname{sech}(\sigma t) \tilde{C}_1(t) \quad (7.29)$$

with

$$\Delta = \frac{1}{2}(\Delta_e + \Delta_h), \quad \sigma = \frac{1}{\tau}. \quad (7.30)$$

Since we are treating the two optically driven transitions as independent during the operation of the pulse, all probability amplitudes may be determined simply by solving for the probability amplitudes of just one of the transitions, as the equations of

motion for the two transitions are equivalent. Here, we consider the $|1\rangle$ to $|4\rangle$ transition. Following the same approach as in References [220] and [132], we differentiate Equation 7.26 and use Equation 7.29 along with the substitution $f = \Omega_p \text{sech}(\sigma t)$ to obtain the differential equation

$$\ddot{\tilde{C}}_1(t) + \left[i\Delta - \frac{\dot{f}}{f} \right] \dot{\tilde{C}}_1(t) + f^2 \tilde{C}_1 = 0. \quad (7.31)$$

Performing the change of variable $x = \frac{1}{2} [\tanh(\sigma t) + 1]$ leads to the equation

$$x(1-x)\tilde{C}_1''(x) + \left[\frac{1}{2} \left(1 + \frac{i\Delta}{\sigma} \right) - x \right] \tilde{C}_1'(x) + \frac{\Omega_p^2}{\sigma^2} \tilde{C}_1(x) = 0 \quad (7.32)$$

which is in the standard form of the hypergeometric equation [221]. The general solution to Equation 7.32 may be written in terms of hypergeometric functions F as

$$\tilde{C}_1(x) = A_1 F(a, -a, c; x) + A_2 x^{c^*} F(a + c^*, -a + c^*, 1 + c^*; x) \quad (7.33)$$

where $a = \frac{\Omega_p}{\sigma}$, $c = \frac{1}{2} \left(1 + \frac{i\Delta}{\sigma} \right)$ and the A_i are constants determined by the initial conditions. Use of initial conditions results in the unitary transformation matrix associated with the $|1\rangle$ to $|4\rangle$ transition of the form

$$U_{|1\rangle \leftrightarrow |4\rangle} = \begin{bmatrix} F(a, -a, c; x) & \frac{2ia}{c^*} x^{c^*} F(c^* - a, c^* + a, c^* + 1; x) \\ \frac{2ia}{c} x^c F(c - a, c + a, c + 1; x) & F(a, -a, c^*; x) \end{bmatrix}, \quad (7.34)$$

and the corresponding matrix for the $|2\rangle$ to $|3\rangle$ transition of the form

$$U_{|2\rangle \leftrightarrow |3\rangle} = \begin{bmatrix} F(a, -a, c^*; x) & \frac{2ia}{c} x^c F(c - a, c + a, c + 1; x) \\ \frac{2ia}{c^*} x^{c^*} F(c^* - a, c^* + a, c^* + 1; x) & F(a, -a, c; x) \end{bmatrix}. \quad (7.35)$$

We are interested in pulses that leave no population in the trion states, a condition that may be met with $\Omega_p = n\sigma$ (n integer) for $t \rightarrow \infty$ ($x \rightarrow 1$). For $n = 1$, the unitary transformation matrix for the electron spin states then has the form

$$U_{n=1} = \begin{bmatrix} 1 - \frac{1}{c} & 0 \\ 0 & 1 - \frac{1}{c^*} \end{bmatrix} = \begin{bmatrix} e^{iv/2} & 0 \\ 0 & e^{-iv/2} \end{bmatrix}, \quad v = 4 \tan^{-1} \left(\frac{\sigma}{\Delta} \right) \quad (7.36)$$

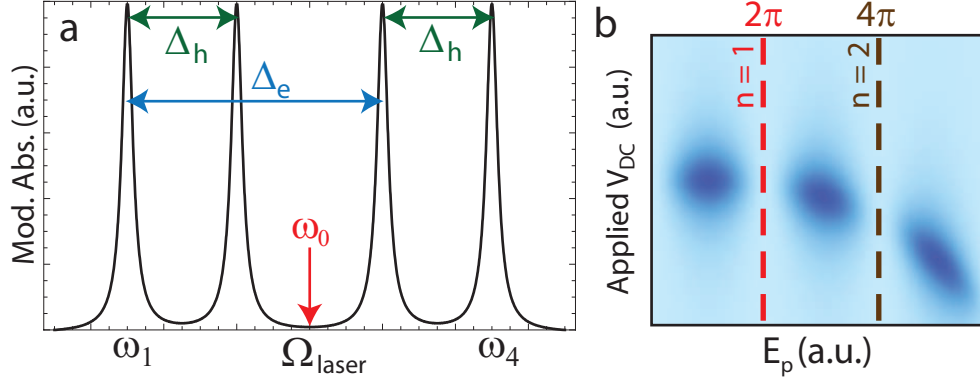


Figure 7.4: (a) Example modulated absorption scan (large modulation) as a function of CW field frequency showing the frequency corresponding to ω_0 . (b) Re-plot of one of the panels of Figure 6.7 corresponding to the theoretical optical tripwire signal in studies with a resonant linearly polarized pulse. Values of E_p corresponding to the $n = 1$ (red dashed line) and $n = 2$ (brown dashed line) conditions are indicated.

where we indeed see that the unitary transformation has the form of a rotation about the \hat{x} axis, the angle depending on the ratio between the pulse bandwidth and the sum of the electron and heavy-hole Zeeman splittings. Rotation angles between 0 to 2π may be achieved, with increasing rotation angles requiring either broader pulse bandwidths for a particular magnetic field strength or smaller magnetic fields for a fixed pulse bandwidth. In addition, it is worth noting that this rotation angle is for the $n = 1$ case and differs from the rotation angles obtained for other values of n . For instance, the $n = 2$ the unitary transformation matrix is

$$U_{n=2} = \begin{bmatrix} e^{i\nu/2} & 0 \\ 0 & e^{-i\nu/2} \end{bmatrix}, \quad \nu = 4 \tan^{-1} \left(\frac{4\Delta\sigma}{\Delta^2 - 3\sigma^2} \right), \quad (7.37)$$

which exhibits a more complicated dependence on the system parameters.

7.2.2 Experimental Procedure

Experimental demonstrations of pulse-generated geometric phases would benefit from the ability to control both the strength of the external magnetic field and the pulse width. The former capability is standard with most magnetocryostats while the latter generally requires the use of pulse shaping techniques. Assuming access to both,

the experimental procedure begins with a selection of a desired rotation angle. Based on this angle, a particular combination of magnetic field strength (given characterized electron and heavy-hole Zeeman splittings) and pulse width is then chosen where the latter may be verified with the autocorrelator or with the spectrometer and CCD.

With these two parameters determined, the trion absorption range at the chosen magnetic field strength is then characterized. Optical tripwire read-out as a function of CW field frequency is then performed in the center of the optical pumping region with a pulse that drives π rotations in all four trion transitions. Because of the action of the pulse, the measured signal will show four peaks as the laser frequency is scanned, enabling the determination of ω_0 [Figure 7.3(a)]. The \hat{x} polarized rotation pulse spectrum is then centered on ω_0 by overlapping the pulse and the CW field (set to ω_0) on the spectrometer CCD. To determine the rotation pulse Rabi frequency Ω_p , another optical tripwire experiment is performed, this time using the rotation pulse and keeping the CW field tuned to either the $|1\rangle$ to $|4\rangle$ transition or the $|2\rangle$ to $|3\rangle$ transition. Measurements are taken as a function of V_{DC} and rotation pulse amplitude [Figure 7.3(b)]. Amplitude values yielding a minimum absorption signal correspond to cases where $\Omega_p = n\sigma$ ($n = 0, 1, \dots$). The pulse power corresponding to the $n = 1$ minimum would be selected.

Once the pulse amplitude is properly set, the operation of the rotation pulse may be demonstrated by performing studies with optical tripwire read-out and two time-delayed two-photon $\pi/2$ pulses. Figure 7.5 shows theoretical calculations of the $|1\rangle$ state population immediately after the second $\pi/2$ pulse in studies without (top) and with (bottom) the \hat{x} polarized rotation pulse. These calculations are based on numerical solutions to the density matrix equations for ideal two-photon $\pi/2$ pulses and a CW field that is turned off between initialization and read-out. Results for a 1 mW rotation pulse approximately 15 ps in width show a $\sim \pi$ rotation of the spin about the \hat{x} axis. These calculations, though somewhat simplified, demonstrate the feasibility of performing fast spin rotations about \hat{x} via the geometric phases generated by linearly polarized optical pulses.

Pulse-driven spin rotations about \hat{x} would enable the construction of a purely

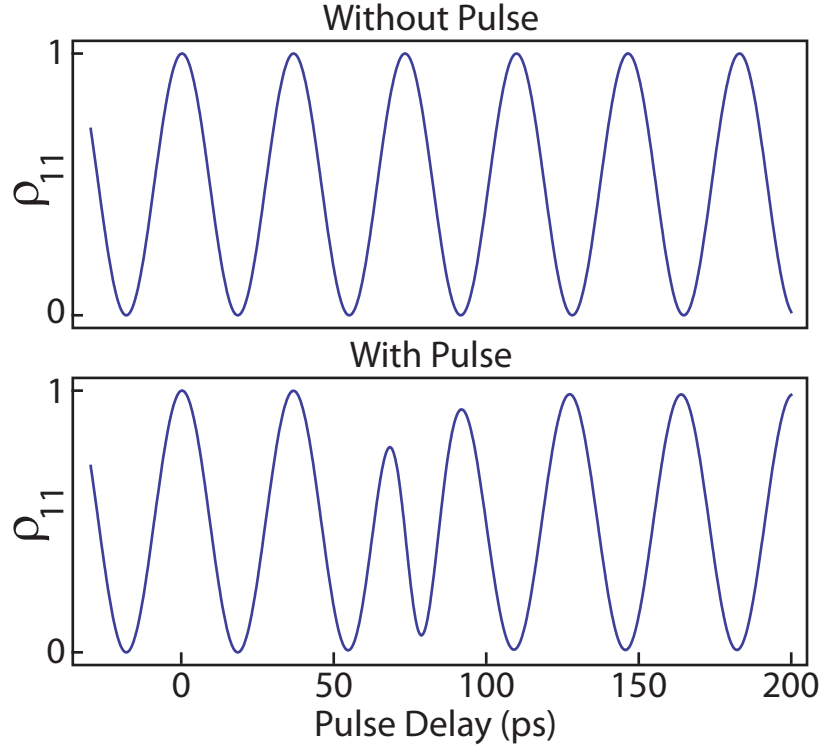


Figure 7.5: Theoretically calculated population in $|1\rangle$ immediately after the second $\pi/2$ pulse in two-pulse studies with a CW field that is turned off between initialization and read-out. Scans are shown both (top) without and (bottom) with a 1 mW \hat{x} polarized rotation pulse about 15 ps in width applied at 75 ps. The rotation pulse results in a $\sim \pi$ rotation of the spin about the \hat{x} axis.

optical set of universal spin operations when combined with the \hat{z} axis rotations driven by detuned circularly polarized pulses. This could potentially allow for spin qubit gates that are fast even in the absence of high external magnetic fields and are more easily tailored to individual spin qubits in multi-dot architectures. In addition, rotation pulses could be used instead of the magnetic field in the DMT procedure discussed in the previous section, providing a purely optical means of obtaining the electron spin density matrix elements.

7.3 Chapter Summary

Two experiments were proposed to build upon the experimental results presented in this thesis. First, an experimental procedure for DMT was discussed, demonstrating that the diagonal and off-diagonal elements of the density matrix for the electron

spin may be projected onto the measurement axis using a combination of spin precession and a two-photon $\pi/2$ pulse. A possible calibration method was also presented, enabling the extraction of populations measured by optical tripwire read-out to assign numerical values to the density matrix elements.

The use of a linearly polarized optical pulse to generate geometric phases for spin rotation was then discussed. The unitary transformation matrix associated with the operation of a linearly-polarized rotation pulse was first derived. An experimental procedure for the demonstration of pulse-driven \hat{x} rotations was then presented, as well as the process by which experimental parameters are selected. Theoretical calculations of the measured $|1\rangle$ population were presented for experiments with a rotation pulse and two time-delayed two-photon $\pi/2$ pulses, showing that with certain experimental capabilities the parameters required for pulse-driven \hat{x} rotations should be well within reach.

CHAPTER 8

Thesis Summary

Chapter 1 first presented a brief historical background of the field of quantum computation, highlighting the theoretical conjectures and discoveries by Feynman, Deutsch, Jozsa, DiVincenzo, Grover and others that served to ignite the vigorous and ongoing research effort towards the realization of a quantum computer. The fundamental requirements for a practical quantum computer, the so-called DiVincenzo criteria, were then discussed. These criteria concern the properties of the physical system under consideration both at the single qubit level and as a whole, as well as the means by which single- and multi-qubit operations are performed. A number of candidate physical systems for quantum computing were then discussed, including trapped ions, nuclear spins in molecules, electron and nuclear spins in diamond, electron and nuclear spins of phosphorous donors in silicon, superconducting circuits and quantum dots. Progress towards satisfying the DiVincenzo criteria for optical approaches to controlling QD confined spins was then discussed, highlighting the potential for ultrafast quantum gate operations.

The properties of the sample and the type of dot studied in experiments were presented in Chapter 2, starting with a general discussion of the different types of self-assembled QDs and their various applications. The growth procedure was discussed in detail, showing the arrangement of the sample layers as well as the aperture pattern on the aluminum shadow mask that enables single-dot studies. The energy levels of a single InAs QD charged with an electron were then presented with and without an external DC magnetic field applied perpendicular to the sample growth axis, along

with the energy level numbering scheme used to simplify mathematical expressions for the probability amplitudes and density matrix elements given throughout this thesis.

In Chapter 3, theoretical expressions for the lock-in detected interference measured by a photodetector between a picosecond pulse resonant with an optical transition in the QD and the field radiated by the pulse-generated polarization in the QD were derived. These expressions showed that the detected signal depends on the density matrix elements of the optically driven transition immediately prior to excitation as well as the pulse area, providing a means of observing transient phenomena in a single QD with the use of a preceding pump pulse. This concept was applied to pump-probe studies with and without the external DC magnetic field, revealing the transient phenomena that may be observed in each type of study. It was shown that in the absence of the magnetic field, trion excitation and decay may be observed while in studies with the magnetic field, electron and heavy-hole spin precession may be observed in addition to trion excitation and decay. In the latter case, the theory also revealed that values for the inhomogeneously broadened electron and heavy-hole spin coherence times, T_2^{e*} and T_2^{h*} , may in principle be determined from pump-probe studies.

Chapter 4 presented the experimental results from pulsed optical studies of a single InAs QD, first discussing the experimental setup and equipment used for all studies presented in this thesis. The characterization procedure for a singly charged QD was also discussed, detailing how PL spectroscopy and DC Stark-shift modulation absorption spectroscopy were used to determine the optical properties of the dot, viz the absorption range in energy and voltage. For studies with a single train of optical pulses resonant with the optical transitions in the dot at zero magnetic field, results showed the ability not only to read-out the QD with optical pulses but also to coherently control the optical transitions in the QD. Such coherent control was demonstrated by an oscillation in the lock-in detected signal as a function of pulse power, indicating a complete Rabi oscillation between the electron and trion states. This read-out signal was then used in pump-probe studies without a magnetic field

to observe trion excitation and decay and to verify the Rabi oscillations observed in one-pulse studies. The two complete Rabi oscillations observed in pump-probe studies also showed additional structures in the peaks of the oscillations that may indicate off-resonant driving of the trion state of a nearby dot. Delay scans taken with the magnetic field showed two-frequency oscillations as a function of pulse delay due to the precession of both electron and heavy-hole spins. These scans enabled the extraction of electron and heavy-hole g-factor magnitudes but prevented the reliable determination of their coherence times due to the limited range of pump-probe delays.

Having demonstrated the ability to coherently control and probe the optical transitions in a singly charged InAs QD, efforts then focused on optically controlling the spin states of the QD confined electron. Three mechanisms of spin control were described theoretically in terms of unitary transformation matrices in Chapter 5: two-photon Raman processes driven by a circularly polarized pulse red-detuned from the trion transition energy, spin precession about the external magnetic field and geometric phases generated by CW-driven Rabi oscillations in one of the trion transitions in the dot. Detuned circularly polarized pulses were shown to rotate the electron spin about the optical axis while both the magnetic field and geometric phases were shown to rotate the spin about the magnetic field axis. Possible spin gates that may be performed by each spin control process were then presented and used to show multiple ways in which the important Hadamard gate may be constructed.

Chapter 6 discussed the experimental approach to demonstrating the spin control mechanisms presented in Chapter 5. Preparation of the electron spin in a pure state by optical pumping was first discussed theoretically, showing that, in the presence of the magnetic field, a CW field tuned to one of the trion transitions depletes the population of the driven electron spin state if the spin lifetime is much longer than the trion lifetime. Experimental results verifying the ability to optically pump the electron spin were then discussed, where successful optical pumping was shown to result in a diminished CW modulated absorption signal. The sensitivity of the CW absorption signal to the time-averaged population of the driven electron spin state was then used to measure the amount of population that reenters that state post initialization

as the result of subsequent optical pulses. This method of read-out, referred to as optical tripwire read-out, was first employed in studies with a single pulse train, demonstrating a complete spin Rabi oscillation for detuned circularly polarized pulses and verifying that the two-photon Raman processes cannot be driven by a linearly polarized pulse. Optical tripwire read-out was then employed in two-pulse studies to observe spin precession and the effect of the geometric phases generated by the operation of the CW field between pulses. The CW-driven trion Rabi oscillations were found to modulate the spin precession signal at the trion Rabi frequency and to lead to π phase shifts in the precession signal each time the driven electron spin population was completely depleted by the CW field. These results verified that both the magnetic field and geometric phases rotate the spin about the magnetic field axis and may be used in conjunction with detuned circularly polarized pulses to perform a universal set of single qubit gates.

Two possible future experiments building upon the results of the previous Chapters were presented in Chapter 7: the density matrix tomography (DMT) of the QD confined electron spin and the use of linearly polarized pulses to generate the geometric phases for electron spin rotation. In DMT experiments, the use of spin precession and a detuned circularly polarized pulse was proposed to measure the different components of the spin Bloch vector in $\{u, v, w\}$ space by optical tripwire read-out. A calibration procedure enabling the extraction of density matrix elements from optical tripwire measurements was also suggested. As an example, the DMT procedure was applied to the case of a Hadamard gate operating on the electron spin, showing how its operation may be verified by performing DMT for two different initial states of the electron spin.

For experiments demonstrating pulse-generated geometric phases, the unitary transformation matrix for the electron spin states was derived for the case of an \hat{x} polarized pulse tuned to lie between the transition energies of the two \hat{x} polarized optical transitions in the dot. Theoretical results verified the ability to rotate the electron spin about the magnetic field axis with an \hat{x} polarized pulse. An experimental procedure was then discussed showing how the strength of the external magnetic field,

the pulse bandwidth, the pulse frequency and the pulse power may be determined for some desired spin rotation angle. Theoretical calculations based on solutions to the density matrix equations were used to show a π rotation of the spin about the magnetic field axis using a 1 mW pulse 15 ps in width, demonstrating the feasibility of implementing such rotations in the laboratory with sufficient control of the pulse width.

The work presented in this thesis represents considerable progress in characterizing and controlling single QD spins for quantum information applications. In architectures employing QD spins for quantum computing, each QD spin employed must be sufficiently characterized to enable the determination of operational parameters, e.g. the trion absorption range and the pulse powers required for particular spin rotation operations. As such, the experimental techniques presented here may be built upon to develop more efficient ways of characterizing individual QD spins, a necessity in multi QD architectures. Further, utilization of the optical spin control mechanisms demonstrated in Chapters 5 and 6 along with those proposed in Chapter 7 for the execution ultrafast universal single qubit gates would—in conjunction with the use of two-qubit gates—constitute a crucial step towards the execution of arbitrary gate operations on an arbitrary number of qubits. With ultrafast single qubit control on the horizon and efforts under way to develop the samples and techniques necessary for multi-qubit operations with QD spins, progress towards the development of a quantum computer with QD spins remains sure and steady.

APPENDICES

APPENDIX A

Calculation of the Selection Rules for a Singly Charged QD

As discussed in Chapter 2, the selection rules for the negatively charged QD can be derived by calculating the matrix elements of the quantity

$$\frac{\mathbf{r}}{r} = -C_{-1}^1 \hat{\epsilon}_{+1} + C_0^1 \hat{\epsilon}_0 - C_{+1}^1 \hat{\epsilon}_{-1} \quad (\text{A.1})$$

with

$$\hat{\epsilon}_{\pm 1} = \mp \frac{1}{2}(\hat{x} \pm i\hat{y}) = \mp \hat{\sigma}_{\pm}, \quad \hat{\epsilon}_0 = \hat{z} \quad (\text{A.2})$$

$$C_m^l = \left(\frac{4\pi}{2l+1} \right)^{\frac{1}{2}} Y_m^l. \quad (\text{A.3})$$

Given the form of Equation A.1, calculation of the matrix elements will require the evaluation of terms of the form $\langle l' s' j' m'_j | C_q^1 | l s j m_j \rangle$ where q is ± 1 or 0 . The first step in evaluating this type of expression is to use the Wigner-Eckart theorem [222]

$$\langle l' s' j' m'_j | C_q^1 | l s j m_j \rangle = (-1)^{j'-m'_j} \begin{pmatrix} j' & 1 & j \\ -m'_j & q & m_j \end{pmatrix} \langle l' s' j' | C^1 | l s j \rangle \quad (\text{A.4})$$

where the quantity in parentheses is the Wigner 3-j symbol. This can be further simplified by utilizing expressions for the scalar product of two tensors, setting the first tensor to the Racah tensor and the second to the identity tensor [222]. This enables expression of the bra-ket term in Equation A.4 as

$$\langle l' s' j' | C^1 | l s j \rangle = (-1)^{l'+s+j+1} \sqrt{(2j'+1)(2j+1)} \begin{Bmatrix} l' & l & 1 \\ j & j' & s \end{Bmatrix} \langle l' || C^1 || l \rangle \delta_{s',s} \quad (\text{A.5})$$

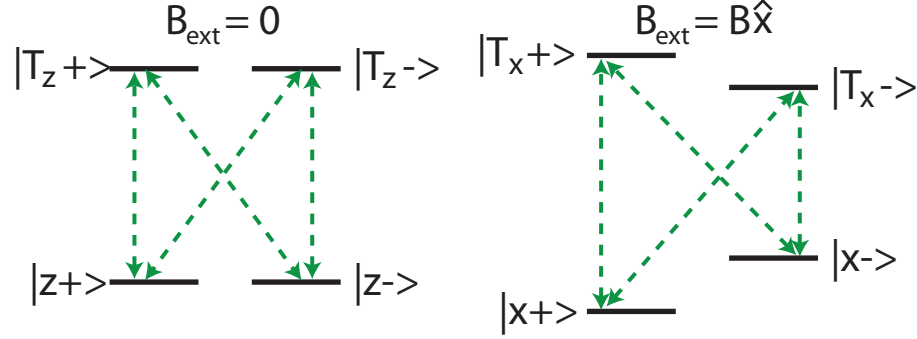


Figure A.1: Transitions for which the matrix elements of \mathbf{r}/r are calculated, indicated by the dashed green arrows, for the two magnetic field cases.

where the curly-bracketed quantity is the Wigner 6-j symbol. We now note that for transitions of interest the spin quantum number s remains constant so the Kronecker delta in Equation A.5 evaluates to 1 and $s' \rightarrow s$. Using the identity [222]

$$\langle l' || C^1 || l \rangle = (-1)^{l'} \sqrt{(2l' + 1)(2l + 1)} \begin{pmatrix} l' & 1 & l \\ 0 & 0 & 0 \end{pmatrix} \quad (\text{A.6})$$

allows us to write the final expression for the matrix element as

$$\begin{aligned} \langle l' s j' m'_j | C_q^1 | l s j m_j \rangle &= (-1)^{j' - m'_j + j + s + 1} \sqrt{(2j' + 1)(2j + 1)(2l' + 1)(2l + 1)} \times \\ &\quad \begin{pmatrix} j' & 1 & j \\ -m'_j & q & m_j \end{pmatrix} \begin{Bmatrix} l' & l & 1 \\ j & j' & s \end{Bmatrix} \begin{pmatrix} l' & 1 & l \\ 0 & 0 & 0 \end{pmatrix}. \end{aligned} \quad (\text{A.7})$$

Use of Equation A.7 in conjunction with Tables 2.1 and 2.2 allows straightforward determination of the selection rules for a singly charged InAs QD with and without an externally applied magnetic field. To illustrate the determination of a particular transition's polarization, we show the calculation for the $|z+\rangle \rightarrow |T_z+\rangle$ transition:

$$\begin{aligned} \langle T_z + | \frac{\mathbf{r}}{r} | z + \rangle &= \left\langle 1 \frac{1}{2} \frac{3}{2} \frac{3}{2} \right| - C_{-1}^1 \hat{\epsilon}_{+1} + C_0^1 \hat{\epsilon}_0 - C_{+1}^1 \hat{\epsilon}_{-1} \left| 1 \frac{1}{2} \frac{1}{2} \frac{1}{2} \right\rangle \\ &= - \underbrace{\left\langle 1 \frac{1}{2} \frac{3}{2} \frac{3}{2} \right| C_{-1}^1 \left| 1 \frac{1}{2} \frac{1}{2} \frac{1}{2} \right\rangle}_{\rightarrow 0} \hat{\epsilon}_{+1} + \underbrace{\left\langle 1 \frac{1}{2} \frac{3}{2} \frac{3}{2} \right| C_0^1 \left| 1 \frac{1}{2} \frac{1}{2} \frac{1}{2} \right\rangle}_{\rightarrow 0} \hat{\epsilon}_0 - \left\langle 1 \frac{1}{2} \frac{3}{2} \frac{3}{2} \right| C_{+1}^1 \left| 1 \frac{1}{2} \frac{1}{2} \frac{1}{2} \right\rangle \hat{\epsilon}_{-1} \\ &\Rightarrow \langle T_z + | \frac{\mathbf{r}}{r} | z + \rangle = - \left\langle 1 \frac{1}{2} \frac{3}{2} \frac{3}{2} \right| C_{+1}^1 \left| 1 \frac{1}{2} \frac{1}{2} \frac{1}{2} \right\rangle \hat{\epsilon}_{-1} = - \frac{1}{\sqrt{3}} \hat{\sigma}_{-}. \end{aligned}$$

From the result of the calculation we see that the matrix element for the $|z+\rangle$ to $|T_z+\rangle$ transition is polarized along $\hat{\sigma}_-$ (where we ignore the constant in front). In considering the form of the optical dipole interaction, $-\boldsymbol{\mu} \cdot \mathbf{E}$ where $\boldsymbol{\mu}$ is the transition dipole and \mathbf{E} is the electric field, only $\hat{\sigma}_+$ polarized light couples the transition, and, hence, the transition is considered $\hat{\sigma}_+$ polarized. Carrying out these calculations for all transitions yields the selection rules shown in Figure 2.4.

For convenience, the matrix representations for the dipole operator $\boldsymbol{\mu}$ are given below both with and without an external magnetic field. For $\mathbf{B}_{\text{ext}} = 0$,

$$\boldsymbol{\mu} = \begin{array}{c} \langle z+| \\ \langle z-| \\ \langle T_z-| \\ \langle T_z+| \end{array} \begin{array}{c} |z+\rangle \\ |z-\rangle \\ |T_z-\rangle \\ |T_z+\rangle \end{array} \begin{bmatrix} 0 & 0 & 0 & \mu\hat{\sigma}_+ \\ 0 & 0 & -\mu\hat{\sigma}_- & 0 \\ 0 & -\mu\hat{\sigma}_+ & 0 & 0 \\ \mu\hat{\sigma}_- & 0 & 0 & 0 \end{bmatrix} \quad (\text{A.8})$$

while for $\mathbf{B}_{\text{ext}} = B\hat{x}$

$$\boldsymbol{\mu} = \begin{array}{c} \langle x+| \\ \langle x-| \\ \langle T_x-| \\ \langle T_x+| \end{array} \begin{array}{c} |x+\rangle \\ |x-\rangle \\ |T_x-\rangle \\ |T_x+\rangle \end{array} \begin{bmatrix} 0 & 0 & -i\mu\hat{y} & -\mu\hat{x} \\ 0 & 0 & -\mu\hat{x} & -i\mu\hat{y} \\ i\mu\hat{y} & -\mu\hat{x} & 0 & 0 \\ -\mu\hat{x} & i\mu\hat{y} & 0 & 0 \end{bmatrix}. \quad (\text{A.9})$$

APPENDIX B

Transformation Relations Between the \hat{z} and \hat{x} Density Matrix Elements: Derivation

Here we derive the transformation relations between density matrix elements in the \hat{z} and \hat{x} bases. To do this, we diagonalize the matrix representation of the \hat{z} basis Hamiltonian for an external DC magnetic field $\mathbf{B}_{\text{ext}} = B\hat{x}$. The total Hamiltonian in this case is $H = H_0 + H_{\text{Zeeman}}$ where H_0 is the Hamiltonian in the absence of any external fields and H_{Zeeman} is the Zeeman interaction Hamiltonian with the operator representation

$$\hat{H}_{\text{Zeeman}} = g_e\mu_B B\hat{s}_e - g_h\mu_B B\hat{s}_h = \Delta_e\hat{s}_e - \Delta_h\hat{s}_h \quad (\text{B.1})$$

where $g_e(g_h)$ is the electron (heavy-hole) g-factor, μ_B is the Bohr magneton and $\hat{s}_e(\hat{s}_h)$ is the spin operator corresponding to the electron (heavy-hole). In matrix form, the total Hamiltonian,

$$H = \begin{array}{c} \langle z+| \\ \langle z-| \\ \langle T_z-| \\ \langle T_z+| \end{array} \frac{1}{\hbar} \begin{array}{c} |z+\rangle \\ |z-\rangle \\ |T_z-\rangle \\ |T_z+\rangle \end{array} \begin{bmatrix} 0 & \frac{\Delta_e}{2} & 0 & 0 \\ \frac{\Delta_e}{2} & 0 & 0 & 0 \\ 0 & 0 & \omega_0 & -\frac{\Delta_h}{2} \\ 0 & 0 & -\frac{\Delta_h}{2} & \omega_0 \end{bmatrix}, \quad (\text{B.2})$$

can be diagonalized by separately diagonalizing the 2×2 matrices representing the electron and trion states, i.e. by diagonalizing the matrices

$$H^e = \hbar \begin{bmatrix} 0 & \frac{\Delta_e}{2} \\ \frac{\Delta_e}{2} & 0 \end{bmatrix}, \quad H^h = \hbar \begin{bmatrix} \omega_0 & -\frac{\Delta_h}{2} \\ -\frac{\Delta_h}{2} & \omega_0 \end{bmatrix}. \quad (\text{B.3})$$

The diagonalization process yields the state transformation relations

$$|x-\rangle = \frac{e^{i\phi_1}}{2} [|z-\rangle - |z+\rangle], \quad |x+\rangle = \frac{e^{i\phi_1}}{2} [|z-\rangle + |z+\rangle] \quad (\text{B.4})$$

$$|T_x-\rangle = \frac{e^{i\phi_2}}{2} [|T_z-\rangle - |T_z+\rangle], \quad |T_x+\rangle = \frac{e^{i\phi_2}}{2} [|T_z-\rangle + |T_z+\rangle] \quad (\text{B.5})$$

where the ϕ_i are arbitrary phases accounting for the ambiguity in electron and trion wavefunction definitions. Using the labeling scheme of Tables 2.1 and 2.2 we obtain the set of transformation relations for \hat{x} basis density matrix elements in terms of \hat{z} basis density matrix elements given in the table below.

\hat{x} basis: $\rho_{ij} = i\rangle\langle j $, \hat{z} basis: $\bar{\rho}_{ij} = \bar{i}\rangle\langle\bar{j} $	
$\rho_{11} = \frac{1}{2} [\bar{\rho}_{11} + \bar{\rho}_{22} + \bar{\rho}_{12} + \bar{\rho}_{21}]$	$\rho_{13} = \frac{1}{2} e^{i(\phi_1 - \phi_2)} [-\bar{\rho}_{13} + \bar{\rho}_{14} - \bar{\rho}_{23} + \bar{\rho}_{24}]$
$\rho_{22} = \frac{1}{2} [\bar{\rho}_{11} + \bar{\rho}_{22} - \bar{\rho}_{12} - \bar{\rho}_{21}]$	$\rho_{31} = \frac{1}{2} e^{-i(\phi_1 - \phi_2)} [-\bar{\rho}_{31} + \bar{\rho}_{41} - \bar{\rho}_{32} + \bar{\rho}_{42}]$
$\rho_{33} = \frac{1}{2} [\bar{\rho}_{33} + \bar{\rho}_{44} - \bar{\rho}_{34} - \bar{\rho}_{43}]$	$\rho_{14} = \frac{1}{2} e^{i(\phi_1 - \phi_2)} [\bar{\rho}_{13} + \bar{\rho}_{14} + \bar{\rho}_{23} + \bar{\rho}_{24}]$
$\rho_{44} = \frac{1}{2} [\bar{\rho}_{33} + \bar{\rho}_{44} + \bar{\rho}_{34} + \bar{\rho}_{43}]$	$\rho_{41} = \frac{1}{2} e^{-i(\phi_1 - \phi_2)} [\bar{\rho}_{31} + \bar{\rho}_{41} + \bar{\rho}_{32} + \bar{\rho}_{42}]$
$\rho_{12} = \frac{1}{2} [\bar{\rho}_{11} - \bar{\rho}_{22} - \bar{\rho}_{12} + \bar{\rho}_{21}]$	$\rho_{23} = \frac{1}{2} e^{i(\phi_1 - \phi_2)} [-\bar{\rho}_{13} + \bar{\rho}_{14} + \bar{\rho}_{23} - \bar{\rho}_{24}]$
$\rho_{21} = \frac{1}{2} [\bar{\rho}_{11} - \bar{\rho}_{22} + \bar{\rho}_{12} - \bar{\rho}_{21}]$	$\rho_{32} = \frac{1}{2} e^{-i(\phi_1 - \phi_2)} [-\bar{\rho}_{31} + \bar{\rho}_{41} + \bar{\rho}_{32} - \bar{\rho}_{42}]$
$\rho_{34} = \frac{1}{2} [-\bar{\rho}_{33} + \bar{\rho}_{44} - \bar{\rho}_{34} + \bar{\rho}_{43}]$	$\rho_{24} = \frac{1}{2} e^{i(\phi_1 - \phi_2)} [\bar{\rho}_{13} + \bar{\rho}_{14} - \bar{\rho}_{23} - \bar{\rho}_{24}]$
$\rho_{43} = \frac{1}{2} [-\bar{\rho}_{33} + \bar{\rho}_{44} + \bar{\rho}_{34} - \bar{\rho}_{43}]$	$\rho_{42} = \frac{1}{2} e^{-i(\phi_1 - \phi_2)} [\bar{\rho}_{31} + \bar{\rho}_{41} - \bar{\rho}_{32} - \bar{\rho}_{42}]$

Table B.1: \hat{x} basis density matrix elements in terms of \hat{z} basis density matrix elements.

\hat{z} basis density matrix elements in terms of \hat{x} density matrix elements can be obtained by applying the substitutions $\bar{\square} \rightarrow \square$ and $\square \rightarrow \bar{\square}$ and taking the complex conjugate of the leading exponential terms.

APPENDIX C

Relationship Between the Electron Spin Bloch Sphere Coordinates in $\{u, v, w\}$ Space and $\{x, y, z\}$ Space

Here, we derive the relationship between the $\{u, v, w\}$ space and $\{x, y, z\}$ space Bloch sphere coordinates for the electron spin. To do this, we first derive relationships between the eigenkets of the Pauli spin matrices. These matrices are of the form

$$\sigma_z = \begin{bmatrix} 1 & 0 \\ 0 & -1 \end{bmatrix} \quad \sigma_x = \begin{bmatrix} 0 & 1 \\ 1 & 0 \end{bmatrix} \quad \sigma_y = \begin{bmatrix} 0 & -i \\ i & 0 \end{bmatrix} \quad (\text{C.1})$$

and we use the notation

$$|z+\rangle \rightarrow \begin{bmatrix} 1 \\ 0 \end{bmatrix}, \quad |z-\rangle \rightarrow \begin{bmatrix} 0 \\ 1 \end{bmatrix} \quad (\text{C.2})$$

to describe the \hat{z} basis spin projections, which are the eigenkets of the σ_z operator. We can write the eigenkets for the spin projections in the \hat{x} and \hat{y} bases in terms of the \hat{z} basis states by diagonalizing the σ_x and σ_y matrices. Doing this, we obtain

$$|x\pm\rangle = \frac{1}{\sqrt{2}} [|z+\rangle \mp |z-\rangle] \quad (\text{C.3})$$

$$|y\pm\rangle = \frac{1}{\sqrt{2}} [|z+\rangle \mp i|z-\rangle]. \quad (\text{C.4})$$

Next, we write the \hat{z} basis states in terms of the \hat{x} basis states to develop expressions

for the \hat{y} basis states in terms of \hat{x} basis states:

$$|z\pm\rangle = \pm \frac{1}{\sqrt{2}} [|x+\rangle \pm |x-\rangle] \quad (\text{C.5})$$

$$|y\pm\rangle = \frac{1}{\sqrt{2}} \left[\left(\frac{1}{\sqrt{2}} [|x+\rangle + |x-\rangle] \right) \mp i \left(-\frac{1}{\sqrt{2}} [|x+\rangle - |x-\rangle] \right) \right] \quad (\text{C.6})$$

$$= \frac{1}{2} [(1 \pm i)|x+\rangle + (1 \mp i)|x-\rangle] \quad (\text{C.7})$$

$$= \frac{1}{\sqrt{2}} [e^{\pm i\pi/4}|x+\rangle + e^{\mp i\pi/4}|x-\rangle] \quad (\text{C.8})$$

$$= \frac{e^{\pm i\pi/4}}{\sqrt{2}} [|x+\rangle + e^{\mp i\pi/2}|x-\rangle] \quad (\text{C.9})$$

$$|y\pm\rangle = \frac{e^{\pm i\pi/4}}{\sqrt{2}} [|x+\rangle \mp i|x-\rangle] \quad (\text{C.10})$$

With these definitions, we now consider the wavefunction of the electron spin for different orientations of the spin Bloch vector in the \hat{u} - \hat{v} plane. The definitions of the various system parameters (originally given in Section 5.1.2) are

$$\mathbf{B} = \begin{bmatrix} B_u \\ B_v \\ B_w \end{bmatrix} = \begin{bmatrix} 2\text{Re}[\tilde{\rho}_{12}(t)] \\ -2\text{Im}[\tilde{\rho}_{12}(t)] \\ \tilde{\rho}_{22}(t) - \tilde{\rho}_{11}(t) \end{bmatrix} = \begin{bmatrix} 2\text{Re}[\tilde{C}_1(t)\tilde{C}_2^*(t)] \\ -2\text{Im}[\tilde{C}_1(t)\tilde{C}_2^*(t)] \\ \tilde{C}_2(t)\tilde{C}_2^*(t) - \tilde{C}_1(t)\tilde{C}_1^*(t) \end{bmatrix} \quad (\text{C.11})$$

where the $\tilde{C}_i = C_i$ are the probability amplitudes of the electron wavefunction in the \hat{x} basis, i.e.

$$|\Psi_x^e(t)\rangle = C_1(t)|x+\rangle + C_2(t)|x-\rangle. \quad (\text{C.12})$$

From Equation C.11 we can immediately deduce the relationship between the \hat{w} and \hat{x} axes as $\hat{w} = -\hat{x}$, as spin projections along $\pm\hat{x}$ correspond to B_w values of ∓ 1 .

To determine the relationship between the remaining coordinates, we derive expressions for the electron spin wavefunction based on the values of ρ_{12} for orientations of the Bloch vector along $\pm\hat{u}$ and $\pm\hat{v}$. For these cases, we have

$$\mathbf{B} \parallel \pm \hat{u} : \quad \text{Re}[C_1 C_2^*] = \pm \frac{1}{2} \quad (\text{C.13})$$

$$\mathbf{B} \parallel \pm \hat{v} : \quad \text{Im}[C_1 C_2^*] = \mp \frac{1}{2}. \quad (\text{C.14})$$

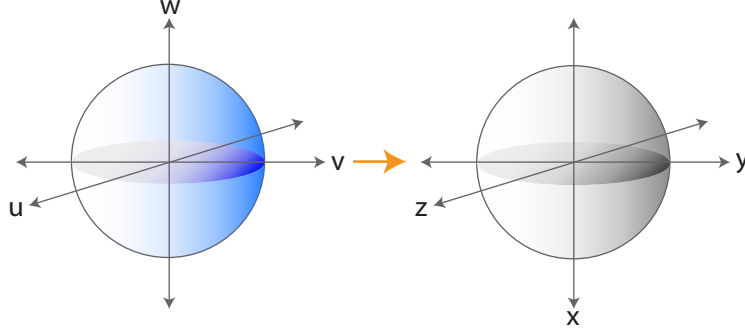


Figure C.1: Relationship between Bloch sphere coordinates in $\{u, v, w\}$ space and $\{x, y, z\}$ space.

We rewrite the probability amplitudes as

$$C_j = A_j e^{i\phi_j}, \quad j = \{1, 2\} \quad (\text{C.15})$$

where each A_j is a pure real positive number and ϕ_j is a phase. For the case of orientation along $\pm\hat{u}$ we have the following system of equations:

$$\pm\frac{1}{2} = A_1 A_2 \text{Re} [e^{i(\phi_1 - \phi_2)}] = A_1 A_2 \cos(\phi_1 - \phi_2) \quad (\text{C.16})$$

$$1 = |C_1|^2 + |C_2|^2 = A_1^2 + A_2^2. \quad (\text{C.17})$$

Solving, we find

$$\frac{1}{\sqrt{2}} = A_1 = A_2 \quad (\text{C.18})$$

$$\phi_1 - \phi_2 = \begin{cases} 2n\pi, & \text{for } +\hat{u} \\ (2n+1)\pi, & \text{for } -\hat{u} \end{cases}, \quad (\text{C.19})$$

yielding expressions for the electron wavefunction at these orientations of the form

$$|\Psi_{\mathbf{B}||\pm\hat{u}}^e\rangle = \frac{e^{i\phi_1}}{\sqrt{2}} [|x+\rangle \pm |x-\rangle]. \quad (\text{C.20})$$

Following the same procedure for orientations along $\pm\hat{v}$, we find

$$|\Psi_{\mathbf{B}||\pm\hat{v}}^e\rangle = \frac{e^{i\phi_1}}{\sqrt{2}} [|x+\rangle \mp i|x-\rangle]. \quad (\text{C.21})$$

Upon inspection, we notice that the electron spin wavefunction for spin Bloch vector orientations along $\pm\hat{u}$ and $\pm\hat{v}$ correspond to electron spin projections along

$\pm\hat{z}$ and $\pm\hat{y}$, respectively, in real space, i.e.

$$|\Psi_{\mathbf{B}||\pm\hat{u}}^e\rangle \propto |z\pm\rangle \quad (\text{C.22})$$

$$|\Psi_{\mathbf{B}||\pm\hat{v}}^e\rangle \propto |y\pm\rangle. \quad (\text{C.23})$$

Summarizing the relationship between Bloch sphere coordinates and real space coordinates, we have

$$\pm\hat{w} \rightarrow \mp\hat{x} \quad (\text{C.24})$$

$$\pm\hat{u} \rightarrow \pm\hat{z} \quad (\text{C.25})$$

$$\pm\hat{v} \rightarrow \pm\hat{y}, \quad (\text{C.26})$$

as illustrated in Figure C.1.

BIBLIOGRAPHY

BIBLIOGRAPHY

- [1] R. P. Feynman, “Simulating Physics with Computers”, *Int. J. Theor. Phys.* **21**, 467 (1982).
- [2] D. Deutsch, “Quantum Theory, the Church-Turing Principle and the Universal Quantum Computer”, *Proc. R. Soc. Lond. A* **400**, 97 (1985).
- [3] M. A. Nielsen, I. L. Chuang, *Quantum Computation and Quantum Information*, Cambridge University Press, Cambridge, United Kingdom, first edition (2000).
- [4] D. Deutsch, “Quantum Computational Networks”, *Proc. R. Soc. Lond. A* **425**, 73 (1989).
- [5] D. Deutsch, R. Jozsa, “Rapid Solution of Problems by Quantum Computation”, *Proc. R. Soc. Lond. A* **439**, 553 (1992).
- [6] S. P. Jordan, “Quantum Computation Beyond the Circuit Model”, *arxiv:0809.2307v1* (2008).
- [7] P. W. Shor, “Algorithms for quantum computation: discrete logarithms and factoring”, *Foundations of Computer Science, 1994 Proceedings., 35th Annual Symposium on* (1994).
- [8] A. Ekert, R. Jozsa, “Quantum computing and Shor’s algorithm”, *Rev. Mod. Phys.* **68**, 733 (1996).
- [9] P. W. Shor, “Polynomial-Time Algorithms for Prime Factorization and Discrete Logarithms on a Quantum Computer”, *SIAM J. Comput.* **26**, 1484 (1997).
- [10] L. K. Grover, “A fast quantum mechanical algorithm for database search”, .
- [11] L. K. Grover, “Quantum Mechanics Helps in Searching for a Needle in a Haystack”, *Phys. Rev. Lett.* **79**, 325 (1997).
- [12] D. S. Abrams, S. Lloyd, “Simulation of Many-Body Fermi Systems on a Universal Quantum Computer”, *Phys. Rev. Lett.* **79**, 2586 (1997).
- [13] S. Lloyd, “Universal Quantum Simulators”, *Science* **273**, 1073 (1996).
- [14] D. A. Lidar, O. Biham, “Simulating Ising spin glasses on a quantum computer”, *Phys. Rev. E* **56**, 3661 (1997).
- [15] M. V. den Nest, W. Dür, R. Raussendorf, H. J. Briegel, “Quantum algorithms for spin models and simulable gate sets for quantum computation”, *arxiv:0805.1214v1* (2008).

- [16] I. Arad, Z. Landau, “Quantum computation and the evaluation of tensor networks.”, *arxiv:0805.0040v2* (2008).
- [17] A. W. Harrow, A. Hassidim, S. Lloyd, “Quantum algorithm for solving linear systems of equations”, *arxiv:0811.3171v2* (2009).
- [18] D. Loss, D. P. D. Vincenzo, “Quantum computation with quantum dots”, *Phys. Rev. A* **57**, 120 (1998).
- [19] A. Imamoglu, D. D. Awschalom, G. Burkard, D. P. DiVincenzo, D. Loss, M. Sherwin, A. Small, “Quantum information processing using quantum dot spins and cavity QED”, *Phys. Rev. Lett.* **83**, 4204 (1999).
- [20] D. P. DiVincenzo, “The physical implementation of quantum computation”, *Fortschr. Phys.* **48**, 771 (2000).
- [21] D. Deutsch, A. Ekert, “Quantum computation”, *Physics World* **March**, 47 (1998).
- [22] D. P. DiVincenzo, “Quantum Computing: Origins and Directions”, *RLE 60th Anniversary Colloquia Series-Beyond the Limits* (2007).
- [23] C. H. Bennett, “Logical Reversibility of Computation”, *IBM J. Res. Dev.* **6**, 525 (1973).
- [24] R. P. Feynman, “Quantum Mechanical Computers”, *Foundations of Physics* **16**, 507 (1986).
- [25] R. L. Rivest, A. Shamir, L. Adleman, “A method for obtaining digital signatures and public-key cryptosystems”, *Communications of the ACM* **21**, 120 (1978).
- [26] V. S. Miller, “Use of Elliptic Curves in Cryptography”, *CRYPTO '85* (1985).
- [27] N. Koblitz, “Elliptic Curve Cryptosystems”, *Mathematics of Computation* **48**, 203 (1987).
- [28] S. Wiesner, “Conjugate Coding”, *ACM SIGACT News* **15**, 78 (1983).
- [29] C. H. Bennett, G. Brassard, “Quantum Cryptography: Public Key Distribution and Coin Tossing”, *Proceedings of the IEEE International Conference on Computers, Systems, and Signal Processing* .
- [30] A. K. Ekert, “Quantum Cryptography Based on Bell’s Theorem”, *Phys. Rev. Lett.* **67**, 661 (1991).
- [31] C. H. Bennett, “Quantum Cryptography Using Any Two Nonorthogonal States”, *Phys. Rev. Lett.* **68**, 3121 (1992).
- [32] C. H. Bennett, G. Brassard, N. D. Mermin, “Quantum Cryptography without Bell’s Theorem”, *Phys. Rev. Lett.* **68**, 557 (1992).

- [33] N. Gisin, G. Ribordy, W. Tittle, H. Zbinden, “Quantum cryptography”, *Rev. Mod. Phys.* **74**, 145 (2002).
- [34] A. Poppe, A. Fedrizzi, R. Ursin, H. R. Böhm, T. Lorünser, O. Maurhardt, M. Peev, M. Suda, C. Kurtsiefer, H. Weinfurter, T. Jennewein, A. Zeilinger, “Practical quantum key distribution with polarization entangled photons”, *Optics Express* **12**, 3865 (2004).
- [35] N. A. Gershenfeld, I. L. Chuang, “Bulk Spin-Resonance Quantum Computation”, *Science* **275**, 350 (1997).
- [36] L. M. K. Vandersypen, M. Steffen, “Implementation of a three-quantum-bit search algorithm”, *Appl. Phys. Lett.* **76**, 646 (2000).
- [37] A. M. Childs, I. L. Chuang, D. W. Leung, “Realization of quantum process tomography in NMR”, *Phys. Rev. A* **64**, 012314 (2001).
- [38] L. M. K. Vandersypen, M. Steffen, G. Breyta, C. S. Yannoni, M. H. Sherwood, I. L. Chuang, “Experimental realization of Shor’s quantum factoring algorithm using nuclear magnetic resonance”, **404**, 883 (2001).
- [39] A. Barenco, C. H. Bennett, R. Cleve, D. P. DiVincenzo, N. Margolus, P. Shor, T. Sleator, J. A. Smolin, H. Weinfurter, “Elementary gates for quantum computation”, *Phys. Rev. A* **52**, 3457 (1995).
- [40] Q. A. Turchette, C. J. Hood, W. Lange, H. Mabuchi, H. J. Kimble, “Measurement of Conditional Phase Shifts for Quantum Logic”, *Phys. Rev. Lett.* **75**, 4710 (1995).
- [41] K. S. Choi, H. Deng, J. Laurat, H. J. Kimble, “Mapping photonic entanglement into and out of a quantum memory”, *Nature* **452**, 67 (2008).
- [42] H. J. Kimble, “The quantum internet”, *Nature* **453**, 1023 (2008).
- [43] C. Monroe, D. M. Meekhof, B. E. King, S. R. Jefferts, W. M. Itano, D. J. Wineland, “Resolved-Sideband Raman Cooling of a Bound Atom to the 3D Zero-Point Energy”, *Phys. Rev. Lett.* **75**, 4011 (1995).
- [44] W. Paul, H. Steinwedel, “A New Mass Spectrometer without a Magnetic Field (Translated from German)”, *Zeitschrift Naturforschung Teil A* **8**, 448 (1953).
- [45] J. I. Cirac, P. Zoller, “Quantum Computations with Cold Trapped Ions”, *Phys. Rev. Lett.* **74**, 4091 (1994).
- [46] D. Kielpinski, C. Monroe, D. J. Wineland, “Architecture for a large-scale ion-trap quantum computer”, *Nature* **417**, 709 (2002).
- [47] R. Blatt, D. Wineland, “Entangled states of trapped atomic ions”, *Nature* **453**, 1008 (2008).

- [48] P. T. H. Fisk, M. J. Sellars, M. A. Lawn, C. Coles, A. G. Mann, D. G. Blair, “Very High Q Microwave Spectroscopy on Trapped $^{171}\text{Yb}^+$ Ions: Application as a Frequency Standard”, .
- [49] H. Nagerl, D. Leibfried, H. Rohde, G. Thalhammer, J. Eschner, F. Schmidt-Kaler, R. Blatt, “Laser addressing of individual ions in a linear ion trap”, *Phys. Rev. A* (1999).
- [50] B. B. Blinov, D. Leibfried, C. Monroe, D. J. Wineland, “Quantum Computing with Trapped Ion Hyperfine Qubits”, *Quantum Information Processing* **3**, 45 (2004).
- [51] B. E. King, C. S. Wood, C. J. Myatt, Q. A. Turchette, D. Leibfried, W. M. Itano, C. Monroe, D. J. Wineland, “Cooling the Collective Motion of Trapped Ions to Initialize a Quantum Register”, *Phys. Rev. Lett.* **81**, 1525 (1998).
- [52] C. Roos, T. Zeiger, H. Rohde, H. C. Nagerl, J. Eschner, D. Leibfried, F. Schmidt-Kaler, R. Blatt, “Quantum State Engineering on an Optical Transition and Decoherence in a Paul Trap”, *Phys. Rev. Lett.* **83**, 4713 (1999).
- [53] C. Monroe, D. M. Meekhof, B. E. King, W. M. Itano, D. J. Wineland, “Demonstration of a Fundamental Quantum Logic Gate”, *Phys. Rev. Lett.* **75**, 4714 (1995).
- [54] S. Gulde, M. Riebe, G. P. T. Lancaster, C. Becher, J. Eschner, H. Haffner, F. Schmidt-Kaler, I. L. Chuang, R. Blatt, “Implementation of the Deutsch-Jozsa algorithm on an ion-trap quantum computer”, *Nature* **421**, 48 (2003).
- [55] M. A. Rowe, D. Kielpinski, V. Meyer, C. A. Sackett, W. M. Itano, C. Monroe, D. J. Wineland, “Experimental violation of a Bell’s inequality with efficient detection”, *Nature* **409**, 791 (2001).
- [56] R. J. Hughes, D. F. V. James, E. H. Knill, R. Laflamme, A. G. Petschek, “Decoherence bounds on quantum computation with trapped ions”, *Phys. Rev. Lett.* **77**, 3240 (1996).
- [57] D. R. Leibbrandt, J. Labaziewicz, R. J. Clark, I. L. Chuang, R. Epstein, C. Ospelkaus, J. Wesenberg, J. Bollinger, D. Leibfried, D. Wineland, D. Stick, J. Sterk, C. Monroe, C.-S. Pai, Y. Low, R. Frahm, R. E. Slusher, “Demonstration of a Scalable, Multiplexed Ion Trap for Quantum Information Processing”, *arxiv:0904.2599v1* (2009).
- [58] G.-D. Lin, S.-L. Zhu, R. Islam, K. Kim, M.-S. Chang, S. Korenbilt, C. Monroe, L.-M. Duan, “Large Scale Quantum Computation in an Anharmonic Linear Ion Trap”, *arxiv:0901.0579v2* (2009).
- [59] T. E. Chupp, E. R. Oteiza, J. M. Richardson, T. R. White, “Precision frequency measurements with polarized ^3He , ^{21}Ne , and ^{129}Xe atoms”, *Phys. Rev. A* **38**, 3998 (1988).

- [60] P. T. Callaghan, *Principles of Nuclear Magnetic Resonance Microscopy*, Oxford University Press Inc., New York, first edition (1994).
- [61] J. A. Jones, M. Mosca, “Implementation of a quantum algorithm on a nuclear magnetic resonance quantum computer”, *Journal of Chemical Physics* **109** (1998).
- [62] N. Linden, H. Barjat, R. Freeman, “An implementation of the Deutsch-Jozsa algorithm on a three-qubit NMR quantum computer”, *Chemical Physics Letters* **296** (1998).
- [63] A. Gruber, A. Drabenstedt, C. Tietz, L. Fleury, J. Wrachtrup, C. von Borczyskowski, “Scanning Confocal Optical Microscopy and Magnetic Resonance on Single Defect Centers”, *Science* **276**, 2012 (1997).
- [64] T. Gaebel, M. Domhan, I. Popa, C. Wittmann, P. Neumann, F. Jelezko, J. R. Rabeau, N. Stavrias, A. D. Greentree, S. Prawer, J. Meijer, J. Twamley, P. R. Hemmer, J. Wrachtrup, “Room-temperature coherent coupling of single spins in diamond”, *Nat. Phys.* **2**, 408 (2006).
- [65] F. Jelezko, T. Gaebel, I. Popa, M. Domhan, A. Gruber, J. Wrachtrup, “Observation of Coherent Oscillation of a Single Nuclear Spin and Realization of a Two-Qubit Condition Quantum Gate”, *Phys. Rev. Lett.* **93**, 130501 (2004).
- [66] P. Neumann, N. Mizuochi, F. Rempp, P. Hemmer, H. Watanbe, S. Yamasaki, V. Jacques, T. Gaebel, F. Jelezko, J. Wrachtrup, “Multipartite Entanglement Among Single Spins in Diamond”, *Science* **320**, 1326 (2008).
- [67] F. Jelezko, T. Gaebel, I. Popa, A. Gruber, J. Wrachtrup, “Observation of Coherent Oscillations in a Single Electron Spin”, *Phys. Rev. Lett.* **92**, 076401 (2004).
- [68] L. Childress, M. V. G. Dutt, J. M. Taylor, A. S. Zibrov, F. Jelezko, J. Wrachtrup, P. R. Hemmer, M. D. Lukin, “Coherent Dynamics of Coupled Electron and Nuclear Spin Qubits in Diamond”, *Science* **314**, 281 (2006).
- [69] S. D. Barrett, P. Kok, “Efficient high-fidelity quantum computation using matter qubits and linear optics”, *Phys. Rev. A* **71**, 060310 (2005).
- [70] B. E. Kane, “A silicon-based nuclear spin quantum computer”, *Nature* **393**, 133 (1998).
- [71] A. M. Tyryshkin, J. J. L. Morton, S. C. Benjamin, A. Ardavan, G. A. D. Briggs, J. W. Ager, S. A. Lyon, “Coherence of spin qubits in silicon”, *J. Phys.: Condens. Matter* **18** (2006).
- [72] G. Feher, “Electron Spin Resonance Experiments on Donors in Silicon. I. Electronic Structure of Donors by the Electron Nuclear Double Resonance Technique”, *Phys. Rev.* **114**, 1219 (1958).

- [73] A. M. Tyryshkin, J. J. L. Morton, A. Ardavan, S. A. Lyon, “Davies electron-nuclear double resonance revisited: Enhanced sensitivity and nuclear spin relaxation”, *J. Chem. Phys.* **124**, 234508 (2006).
- [74] J. L. O’Brien, S. R. Schofield, M. Y. Simmons, R. G. Clark, A. S. Dzurak, N. J. Curson, B. E. Kane, N. S. McAlpine, M. E. Hawley, G. W. Brown, “Towards the fabrication of phosphorus qubits for a silicon quantum computer”, *Phys. Rev. B* **64**, 161401 (2001).
- [75] T. Schenkel, A. Persaud, S. J. Park, J. Nilsson, J. Bokor, J. A. Liddle, R. Keller, D. H. Schneider, D. W. Cheng, D. E. Humphries, “Solid state quantum computer development in silicon with single ion implantation”, *Jour. App. Phys.* **94**, 7017 (2003).
- [76] B. Koiller, “Hybrid electron control”, *Nat. Phys.* **4**, 590 (2008).
- [77] G. P. Lansbergen, R. Rahman, C. J. Wellard, I. Woo, J. Caro, N. Collaert, S. Biesemans, G. Klimeck, L. C. L. Hollenberg, S. Rogge, “Gate-induced quantum-confinement transition of a single dopant atom in a silicon FinFET”, *Nat. Phys.* **4**, 656 (2008).
- [78] J. J. L. Morton, A. M. Tyryshkin, R. M. Brown, S. Shankar, B. W. Lovett, A. Ardavan, T. Schenkel, E. E. Haller, J. W. Ager, S. A. Lyon, “Solid-state quantum memory using the ^{31}P nuclear spin”, *Nature* **455**, 1085 (2008).
- [79] B. D. Josephson, “The discovery of tunnelling supercurrents”, *Rev. Mod. Phys.* **46**, 251 (1974).
- [80] R. F. Voss, R. A. Webb, “Macroscopic Quantum Tunneling in $1\text{-}\mu\text{m}$ Nb Josephson Junctions”, *Phys. Rev. Lett.* **47**, 265 (1981).
- [81] J. Clarke, F. K. Wilhelm, “Superconducting quantum bits”, *Nature* **453**, 1031 (2008).
- [82] A. Shnirman, G. Schön, Z. hermon, “Quantum Manipulations of Small Josephson Junctions”, *Phys. Rev. Lett.* **79**, 2371 (1997).
- [83] R. McDermott, R. W. Simmonds, M. Steffen, K. B. Cooper, K. Cicak, K. D. Osborn, S. Oh, D. P. Pappas, J. M. Martinis, “Simultaneous state measurement of coupled Josephson phase qubits”, *Science* **307**, 1299 (2005).
- [84] J. A. Schreier, A. A. Houck, J. Koch, D. I. Schuster, B. R. Johnson, J. M. Chow, J. M. Gambetta, J. Majer, L. Frunzio, M. H. Devoret, S. M. Girvin, “Suppressing charge noise decoherence in superconducting charge qubits”, *Phys. Rev. B* **77** (2008).
- [85] L. DiCarlo, J. M. Chow, J. M. Gambetta, L. S. Bishop, B. R. Johnson, D. I. Schuster, J. Majer, A. Blais, L. Frunzio, S. M. girvin, R. J. Schoelkopf, “Demonstration of two-qubit algorithms with a superconducting quantum processor”, *Nature in press* (2009).

- [86] J. M. Martinis, S. Nam, J. Aumentado, “Rabi Oscillations in a Large Josephson-Junction Qubit”, *Phys. Rev. Lett.* **89**, 117901 (2002).
- [87] E. Lucero, M. Hofheinz, M. Ansmann, R. C. Bialczak, N. Katz, M. Neeley, A. D. O’Connell, H. Wang, A. N. Cleland, J. M. Martinis, “High-Fidelity Gates in a Single Josephson Qubit”, *Phys. Rev. Lett.* **100**, 247001 (2008).
- [88] T. Yamamoto, Y. A. Pashkin, O. Astafiev, Y. Nakamura, J. S. Tsai, “Demonstration of conditional gate operations using superconducting charge qubits”, *Nature* **425**, 941 (2003).
- [89] J. H. Plantenberg, P. C. de Groot, C. J. P. M. Harmans, J. E. Mooij, “Demonstration of controlled-NOT quantum gates on a pair of superconducting quantum bits”, *Nature* **447**, 836 (2007).
- [90] M. Steffen, M. Ansmann, R. C. Bialczak, N. Katz, E. Lucero, R. McDermott, M. Neeley, E. M. Weig, A. N. Cleland, J. M. Martinis, “Measurement of the Entanglement of Two Superconducting Qubits via State Tomography”, *Science* **313**, 1423 (2006).
- [91] J. Majer, J. M. Chow, J. M. Gambetta, J. Koch, B. R. Johnson, J. A. Schreier, L. Frunzio, D. I. Schuster, A. A. Houck, A. Wallraff, A. Blais, M. H. Devoret, S. M. Girvin, R. J. Schoelkopf, “Coupling superconducting qubits via a cavity bus”, *Nature* **449**, 443 (2007).
- [92] D. Leonard, M. Krishnamurthy, C. M. Reaves, S. P. Denbaars, P. M. Petroff, “Direct formation of quantum-sized dots from uniform coherent islands of InGaAs on GaAs surfaces”, *Appl. Phys. Lett.* **63**, 3203 (1993).
- [93] A. Zrenner, L. V. Butov, M. Hagn, G. Abstreiter, G. Böhm, G. Weimann, “Quantum dots formed by interface fluctuations in AlAs/GaAs coupled quantum well structures”, *Phys. Rev. Lett.* **72**, 3382 (1994).
- [94] D. Gammon, E. S. Snow, B. V. Shanabrook, D. S. Katzer, D. Park, “Homogeneous Linewidths in the Optical Spectrum of a Single Gallium Arsenide Quantum Dot”, *Science* **273**, 87 (1996).
- [95] D. Gammon, D. G. Steel, “Optical Studies of Single Quantum Dots”, *Physics World* **October**, 36 (2002).
- [96] M. Brust, M. Walker, D. Bethell, D. J. Schiffrin, R. Whyman, “Synthesis of Thiol-derivatised Gold Nanoparticles in a Two-phase Liquid-Liquid System”, *J. Chem. Soc., Chem. Commun.* (1994).
- [97] C. P. Collier, R. J. Saykally, J. J. Shiang, S. E. Henrichs, J. R. Heath, “Reversible Tuning of Silver Quantum Dot Monolayers Through the Metal-Insulator Transition”, *Science* **277**, 1978 (1997).

- [98] V. Lindberg, B. Hellsing, “Metallic quantum dots”, *J. Phys.: Condens. Matter* **17** (2005).
- [99] M. R. Buitelaar, A. Bachtold, T. Nussbaumer, M. Iqbal, C. Schönenberger, “Multiwall Carbon Nanotubes as Quantum Dots”, *Phys. Rev. Lett.* **88**, 156801 (2002).
- [100] N. Mason, M. J. Biercuk, C. M. Marcus, “Local Gate Control of a Carbon Nanotube Double Quantum Dot”, *Science* **303**, 655 (2004).
- [101] S. Tarucha, D. G. Austing, T. Honda, R. J. van der Hage, L. P. Kouwenhoven, “Shell Filling and Spin Effects in a Few Electron Quantum Dot”, *Phys. Rev. Lett.* **77**, 3613 (1996).
- [102] M. Ciorga, A. S. Sachrajda, P. Hawrylak, C. Gould, P. Zawadzki, S. Jullian, Y. Feng, Z. Wasilewski, “Addition spectrum of a lateral dot from Coulomb and spin-blockade spectroscopy”, *Phys. Rev. B* **61** (2000).
- [103] J. M. Elzerman, R. Hanson, J. S. Greidanus, L. H. W. van Beveren, S. D. Franceschi, L. M. K. Vandersypen, S. Tarucha, L. P. Kouwenhoven, “Few-electron quantum dot circuit with integrated charge read out”, *PRB* **67** (2003).
- [104] R. Hanson, L. P. Kouwenhoven, J. R. Petta, S. Tarucha, L. M. K. Vandersypen, “Spins in few electron quantum dots”, *Rev. Mod. Phys.* **79**, 1217 (2007).
- [105] C. Piermarocchi, P. Chen, L. J. Sham, D. G. Steel, “Optical RKKY Interaction between Charged Semiconductor Quantum Dots”, *Phys. Rev. Lett.* **89**, 167402 (2002).
- [106] S. K. Saikin, C. Emary, D. G. Steel, L. J. Sham, “Adiabatic optical entanglement between electron spins in separate quantum dots”, .
- [107] X. Li, Y. Wu, D. Steel, D. Gammon, T. H. Stievater, D. S. Katzer, D. Park, C. Piermarocchi, L. J. Sham, “An All-Optical Quantum Gate in a Semiconductor Quantum Dot”, *Science* **301**, 809 (2003).
- [108] S. J. Boyle, A. J. Ramsay, F. Bello, H. Y. Liu, M. Hopkinson, A. M. Fox, M. S. Skolnick, “Two-qubit conditional quantum-logic operation in a single self-assembled quantum dot”, *Phys. Rev. B* **78**, 075301 (2008).
- [109] R. Hanson, B. Witkamp, L. Vandersypen, L. H. W. van everen, J. M. Elzerman, L. P. Kouwenhoven, “Zeeman Energy and Spin Relaxation in a One-Electron Quantum Dot”, *Phys. Rev. Lett.* **91**, 196802 (2003).
- [110] J. M. Elzerman, R. Hanson, L. H. W. van Beveren, B. Witkamp, L. M. K. Vandersypen, L. P. Kouwenhoven, “Single-shot read-out of an individual electron spin in a quantum dot”, *Nature* **430**, 431 (2004).

- [111] R. Hanson, L. H. W. van Beveren, I. T. Vink, J. M. Elzerman, W. J. M. Naber, F. H. L. Koppens, L. P. Kouwenhoven, L. M. K. Vandersypen, “Single-shot read-out of electron spin states in a quantum dot using spin-dependent tunnel rates”, *Phys. Rev. Lett.* **94**, 196802 (2005).
- [112] J. R. Petta, A. C. Johnson, J. M. Taylor, E. A. Laird, A. Yacoby, M. D. Lukin, C. M. Marcus, M. P. Hanson, A. C. Gossard, “Coherent Manipulation of Coupled Electron Spins in Semiconductor Quantum Dots”, *Science* **309**, 2180 (2005).
- [113] K. C. Nowack, F. H. L. Koppens, Y. V. Nazarov, L. M. K. Vandersypen, “Coherent Control of a Single Electron Spin with Electric Fields”, *Science* **318**, 1430 (2007).
- [114] F. H. L. Koppens, C. Buizert, K. J. Tielrooij, I. T. Vink, K. C. Nowack, T. Meunier, L. P. Kouwenhoven, L. M. K. Vandersypen, “Driven coherent oscillations of a single electron spin in a quantum dot”, *Nature* **442**, 766 (2006).
- [115] M. Kroutvar, Y. Ducommun, D. Heiss, M. Bichler, D. Schuh, G. Abstreiter, J. J. Finley, “Optically programmable electron spin memory using semiconductor quantum dots”, *Nature* **432**, 81 (2004).
- [116] A. Greilich, D. R. Yakovlev, A. Shabaev, A. L. Efros, I. A. Yugova, R. Oulton, V. Stavarache, D. Reuter, A. Wieck, M. Bayer, “Mode Locking of Electron Spin Coherences in Singly Charged Quantum Dots”, *Science* **313**, 341 (2006).
- [117] A. Greilich, A. Shabaev, D. R. Yakovlev, A. L. Efros, I. A. Yugova, D. Reuter, A. D. Wieck, M. Bayer, “Nuclei-Induced Frequency Focusing of Electron Spin Coherence”, *Science* **317**, 1896 (2007).
- [118] A. V. Khaetskii, D. Loss, L. Glazman, “Electron Spin Decoherence in Quantum Dots due to Interaction with Nuclei”, *Phys. Rev. Lett.* **88**, 186802 (2002).
- [119] M. H. Mikkelsen, J. Berezovsky, N. G. Stoltz, L. A. Coldren, D. D. Awschalom, “Optically detected coherent spin dynamics of a single electron in a quantum dot”, *Nature Physics* **3**, 770 (2007).
- [120] X. Xu, B. Sun, P. R. Berman, D. G. Steel, A. S. Bracker, D. Gammon, L. J. Sham, “Coherent population trapping of an electron spin in a single negatively charged quantum dot”, *Nat. Phys.* **4**, 692 (2008).
- [121] X. Xu, W. Yao, B. Sun, D. G. Steel, A. S. Bracker, D. Gammon, L. J. Sham, “Optically controlled locking of the nuclear field via coherent dark-state spectroscopy”, *Nature* **459**, 1105 (2009).
- [122] D. V. Bulaev, D. Loss, “Spin relaxation and decoherence of holes in quantum dots”, *Phys. Rev. Lett.* **95**, 076805 (2005).

- [123] D. Heiss, S. Schaeck, H. Huebl, M. Bichler, G. Abstreiter, J. J. Finley, D. V. Bulaev, D. Loss, “Observation of extremely slow hole spin relaxation in self-assembled quantum dots”, *Phys. Rev. B* **76** (2007).
- [124] G. Burkard, “Quantum information: Positively spin coherent”, *Nature Materials* **7**, 100 (2008).
- [125] D. Brunner, B. D. Gerardot, , P. A. Dalgarno, G. Wüst, K. Karrai, N. G. Stoltz, P. M. Petroff, R. J. Warborton, “A Coherent Single-Hole Spin in a Semiconductor”, *Science* **325**, 70 (2009).
- [126] M. Atatüre, J. Dreiser, A. Badolato, A. Högele, K. Karrai, A. Imamoglu, “Quantum-Dot Spin-State Preparation with Near-Unity Fidelity”, *Science* **310**, 551 (2006).
- [127] C. Emary, X. Xu, D. G. Steel, S. Saikin, L. J. Sham, “Fast Initialization of the Spin State of an Electron in a Quantum Dot in the Voigt Configuration”, *Phys. Rev. Lett.* **98**, 047401 (2007).
- [128] X. Xu, Y. Wu, B. Sun, Q. Huang, J. Cheng, D. Steel, A. Bracker, D. Gammon, C. Emary, L. Sham, “Fast spin state initialization in a singly charged InAs-GaAs quantum dot by optical cooling”, *Phys. Rev. Lett.* **99**, 097401 (2007).
- [129] B. D. Gerardot, D. Brunner, P. A. Dalgarno, P. Öhberg, S. Seidl, M. Kroner, K. Karrai, N. G. Stoltz, P. M. Petroff, R. J. Warburton, “Optical pumping of a single hole spin in a quantum dot”, *Nature* **451**, 441 (2008).
- [130] J. Berezovsky, M. H. Mikkelsen, N. G. Stoltz, L. A. Coldren, D. D. Awschalom, “Picosecond Coherent Optical Manipulation of a Single Electron Spin in a Quantum Dot”, *Science* **320**, 349 (2008).
- [131] D. Press, T. D. Ladd, B. Zhang, Y. Yamamoto, “Complete quantum control of a single quantum dot spin using ultrafast optical pulses”, **456**, 218 (2008).
- [132] S. E. Economou, L. J. Sham, Y. Wu, D. G. Steel, “Proposal for optical U(1) rotations of electron spin trapped in a quantum dot”, *Phys. Rev. B* **74**, 205415 (2006).
- [133] S. E. Economou, T. L. Reinecke, *Phys. Rev. Lett.* **99**, 217401 (2007).
- [134] J. Vuckovic, Y. Yamamoto, “Photonic crystal microcavities for cavity quantum electrodynamics with a single quantum dot”, *Appl. Phys. Lett.* **82**, 2374 (2003).
- [135] D. Englund, I. Fushman, A. Faraon, J. Vuckovic, “Quantum dots in photonic crystals: From quantum information processing to single photon nonlinear optics”, *Photonics Nanostruct. Fundam. Appl.* **7**, 56 (2008).
- [136] E. M. Kessler, M. Grochol, C. Piermarocchi, “Light-mass Bragg cavity polaritons in planar quantum dot lattices”, *Phys. Rev. B* **77**, 085306 (2008).

- [137] M. Grochol, C. Piermarocchi, “Multispin errors in the optical control of a spin quantum lattice”, *Phys. Rev. B* **78**, 165324 (2008).
- [138] D. Leonard, K. Pond, P. M. Petroff, “Critical layer thickness for self-assembled InAs islands on GaAs”, *Phys. Rev. B* **50**, 11687 (1994).
- [139] Y. Wu, X. Li, L. M. Duan, D. G. Steel, D. Gammon, “Density Matrix Tomography through Sequential Coherent Optical Rotations of an Exciton Qubit in a Single Quantum Dot”, *Phys. Rev. Lett.* **96**, 087402 (2006).
- [140] N. Carlsson, W. Seifert, A. Petersson, P. Castrillo, M. E. Pistol, L. Samuelson, “Study of the two-dimensional–three-dimensional growth mode transition in metalorganic vapor phase epitaxy of GaInP/InP quantum-sized structures”, *Appl. Phys. Lett.* **65**, 3093 (1994).
- [141] M. K. Zundel, P. Specht, K. Eberl, N. Y. Jin-Phillip, F. Phillipp, “Structural and optical properties of vertically aligned InP quantum dots”, *Appl. Phys. Lett.* **71**, 2972 (1997).
- [142] S. Fafard, K. Hinzer, S. Raymond, M. Dion, J. McCaffrey, Y. Feng, S. Charbonneau, “Red-emitting semiconductor quantum dot lasers”, *Science* **274**, 1350 (1996).
- [143] E. R. Glaser, B. R. Bennett, B. V. Shanabrook, R. Magno, “Photoluminescence studies of self-assembled InSb, GaSb and AlSb quantum dot heterostructures”, *Appl. Phys. Lett.* **68**, 3614 (1996).
- [144] F. Hatami, W. T. Masselink, L. Schrottke, J. W. Tomm, V. Talalaev, C. Kristukat, A. R. Goni, “InP quantum dots embedded in GaP: Optical properties and carrier dynamics”, *Phys. Rev. B* **67**, 085306 (2003).
- [145] M. Nirmal, D. J. Norris, M. Kuno, M. G. Bawendi, A. L. Efros, M. Rosen, “Observation of the “Dark Exciton” in CdSe Quantum Dots”, *Phys. Rev. Lett.* **75**, 3728 (1995).
- [146] S. H. Xin, P. D. Wang, A. Yin, C. Kim, M. Dobrowolska, J. L. Merz, “Formation of self-assembling CdSe quantum dots on ZnSe by molecular beam epitaxy”, *Appl. Phys. Lett.* **69**, 3884 (1996).
- [147] G. Karczewski, S. Mackowski, M. Kutrowski, T. Wojtowicz, J. Kossut, “Photoluminescence study of CdTe/ZnTe self-assembled quantum dots”, *Appl. Phys. Lett.* **74**, 3011 (1999).
- [148] X. G. Peng, M. C. Schlamp, A. V. Kadavanich, A. P. Alivisatos, “Epitaxial growth of highly luminescent CdSe/GdS core/shell nanocrystals with photostability and electronic accessibility”, *J. Am. Chem. Soc.* **119**, 7019 (1997).
- [149] X. G. Peng, L. Manna, W. Yang, J. Wickham, E. Scher, A. Kadavanich, A. P. Alivisatos, “Shape control of CdSe nanocrystals”, *Nature* **404**, 59 (2000).

- [150] S. Besson, T. Gacoin, C. Ricolleau, C. Jacquiod, J.-P. Boilot, “3D Quantum Dot Lattice Inside Mesoporous Silica Films”, *Nano Letters* **2**, 409 (2002).
- [151] D. J. Eaglesham, M. Cerullo, “Dislocation-free Stranski-Krastanow growth of Ge on Si (100)”, *Phys. Rev. Lett.* **64**, 1943 (1994).
- [152] K. Wang, J. Liu, G. Jin, “Self-assembled Ge quantum dots on Si and their applications”, *J. Crystal Growth* **237** (2002).
- [153] K. L. Wang, D. Cha, J. Liu, C. Chen, “Ge/Si Self-Assembled Quantum Dots and Their Optoelectronic Device Applications”, *Proceedings of the IEEE* **9**, 1866 (2007).
- [154] G. Springholz, V. Holy, M. Pinczolits, G. Bauer, “Self-Organized Growth of Three-Dimensional Quantum-Dot Crystals with fcc-Like Stacking and a Tunable Lattice Constant”, *Science* **282**, 734 (1998).
- [155] H. Lee, J. A. Johnson, M. Y. He, J. S. Speck, P. M. Petroff, “Strain-engineered self-assembled semiconductor quantum dot lattices”, *Appl. Phys. Lett.* **78**, 105 (2001).
- [156] K. Kamath, P. Bhattacharya, T. Sosnowski, T. Norris, J. Phillips, “Room temperature operation of $\text{In}_{0.4}\text{Ga}_{0.6}\text{As}/\text{GaAs}$ self-organized quantum dot lasers”, *Electronic Lett.* **32**, 1374 (1996).
- [157] H. Saito, K. Nishi, I. Ogura, S. Sugou, Y. Sugimoto, “Room-temperature lasing operation of a quantum-dot vertical-cavity surface-emitting laser”, *Appl. Phys. Lett.* **69**, 3140 (1996).
- [158] D. L. Huffaker, G. Park, Z. Zou, O. B. Shchekin, D. G. Deppe, “1.3 μm room-temperature GaAs-based quantum-dot laser”, *Appl. Phys. Lett.* **73**, 2564 (1998).
- [159] P. Bhattacharya, S. Krishna, J. Phillips, P. J. McCann, K. Namjou, “Carrier dynamics in self-organized quantum dots and their application to long-wavelength sources and detectors”, *J. Crystal Growth* **84**, 2513 (2000).
- [160] X. D. Huang, A. Stintz, H. Li, L. F. Lester, J. Cheng, K. J. Malloy, “Passive mode-locking in 1.3 μm two-section InAs quantum dot lasers”, *Appl. Phys. Lett.* **78**, 2825 (2000).
- [161] K. W. Berryman, S. A. Lyon, M. Segev, “Mid-infrared photoconductivity in InAs quantum dots”, *Appl. Phys. Lett.* **70**, 1861 (1997).
- [162] J. Phillips, K. Kamath, P. Bhattacharya, “Far-infrared photoconductivity in self-organized InAs quantum dots”, *Appl. Phys. Lett.* **72**, 2020 (1998).
- [163] D. Pan, E. Towe, S. Kennerly, “Normal-incidence intersubband (In, Ga)As/GaAs quantum dot infrared photodetectors”, *Appl. Phys. Lett.* **73**, 1937 (1998).

- [164] S. J. Xu, S. J. Chua, T. Mei, X. C. Wang, X. H. Zhang, G. Karunasiri, “Characteristics of InGaAs quantum dot infrared photodetectors”, *Appl. Phys. Lett.* **73**, 3153 (1998).
- [165] S. Kim, H. Mohseni, M. Erdtmann, E. Michel, C. Jelen, M. Razeghi, “Growth and characterization of InGaAs/InGaP quantum dots for midinfrared photoconductive detector”, *Appl. Phys. Lett.* **73**, 963 (1998).
- [166] S.-W. Lee, K. Hirakawa, Y. Shimada, “Bound-to-continuum intersubband photoconductivity of self-assembled InAs quantum dots in modulation-doped heterostructures”, *Appl. Phys. Lett.* **75**, 1428 (1999).
- [167] H. Liu, J.-Y. Duboz, R. Dudek, Z. Wasilewski, S. Fafard, P. Finnie, “Quantum dot infrared photodetectors”, *physica. E* **17**, 631 (2003).
- [168] E. Waks, J. Vuckovic, “Dipole Induced Transparency in Drop-Filter Cavity-Waveguide Systems”, *Phys. Rev. Lett.* **96**, 153601 (2006).
- [169] P. van Loock, T. Ladd, K. Sanaka, F. Yamaguchi, K. Nemoto, W. Munro, Y. Yamamoto, “Hybrid Quantum Repeater Using Bright Coherent Light”, *Phys. Rev. Lett.* **96**, 240501 (2006).
- [170] K. Aoki, D. Guimard, M. Nishioka, M. Nomura, S. Iwamoto, Y. Arakawa, “Coupling of quantum-dot light emission with a three-dimensional photonic crystal nanocavity”, *Nature Photonics* **2**, 688 (2008).
- [171] P. Michler, A. Kiraz, C. Becher, W. V. Schoenfeld, P. M. Petroff, L. Zhang, E. Hu, A. Imamoglu, “A quantum dot single-photon turnstile device”, *Science* **290**, 2282 (2000).
- [172] C. Santori, M. Pelton, G. Solomon, Y. Dale, E. Yamamoto, “Triggered single photons from a quantum dot”, *Phys. Rev. Lett.* **86**, 1502 (2001).
- [173] C. Becher, A. Kiraz, P. Michler, A. Imamoglu, W. V. Schoenfeld, P. M. Petroff, L. Zhang, E. Hu, “Triggered single photons from a quantum dot”, *Phys. Rev. B* **63**, 121312(R) (2001).
- [174] Z. Yuan, B. E. Kardynal, R. M. Stevenson, A. J. Shields, C. J. Lobo, K. Cooper, N. S. Beattie, D. A. Ritchie, M. Pepper, “Electrically Driven Single-Photon Source”, *Science* **295**, 102 (2002).
- [175] X. Xu, D. A. Williams, J. R. A. Cleaver, “Electrically pumped single-photon sources in lateral p-i-n junctions”, *Appl. Phys. Lett.* **85**, 3238 (2004).
- [176] D. L. Huffaker, L. A. Graham, D. G. Deppe, “Ultrarrow electroluminescence spectrum from the ground state of an ensemble of self-organized quantum dots”, *Appl. Phys. Lett.* **72**, 214 (1998).

- [177] M. H. Baier, C. Constantin, E. Pelucchi, E. Kapon, “Electroluminescence from a single pyramidal quantum dot in a light-emitting diode”, *Appl. Phys. Lett.* **84**, 1967 (2004).
- [178] C. Monat, B. Alloing, C. Zinoni, L. H. Li, A. Fiore, “Nanostructured Current-Confining Single Quantum Dot Light-Emitting Diode at 1300nm”, *Nano Letters* **6**, 1464 (2006).
- [179] E. Biolatti, T. Calarco, I. D’Amico, P. Zanardi, F. Rossi, P. Zoller, “Spin-based optical quantum computation via Pauli blocking in semiconductor quantum dots”, *Europhysics Lett* **62**, 175 (2003).
- [180] T. Calarco, A. Datta, P. Fedichev, E. Pazy, P. Zoller, “Spin-based all-optical quantum computation with quantum dots: Understanding and suppressing decoherence”, *Phys. Rev. A* **68**, 012310 (2003).
- [181] I. Riech, J. G. Mendoza-Alvarez, M. L. Gomez-Herrera, J. L. Herrera-Perez, “Effect of Te doping of InGaAsSb layers on the interface quality of InGaAsSb/GaSb heterojunctions”, *Semicond. Sci. Technol.* **18**, 763 (2003).
- [182] D. Gammon, *personal communication* (2008).
- [183] Z. R. Wasilewski, S. Fafard, J. P. McCaffrey, “Size and shape engineering of vertically stacked self-assembled quantum dots”, *J. Cryst. Growth* **201-202**, 1131 (1999).
- [184] H. Sasakura, S. Kayamora, S. Adachi, S. Muto, “Effect of indium-flush method on the control of photoluminescence energy of highly uniform self-assembled InAs quantum dots by slow molecular beam epitaxy growth”, *J. Appl. Phys.* **102**, 013515 (2007).
- [185] H. Drexler, D. Leonard, W. Hansen, J. P. Kotthaus, P. M. Petroff, “Spectroscopy of Quantum Levels in Charge-Tunable InGaAs Quantum dots”, *Phys. Rev. Lett.* **73**, 2252 (1994).
- [186] J. Singh, *Electronic and Optoelectronic Properties of Semiconductor Structures*, Cambridge University Press, Cambridge, first edition (2003).
- [187] Y. Zhang, “Motion of electrons in semiconductors under inhomogeneous strain with application to laterally confined quantum wells”, *Phys. Rev. B* **49**, 14352 (1994).
- [188] J.-Y. Marzin, G. Bastard, “Calculation of the Energy Levels in InAs/GaAs Quantum Dots”, *Solid State Communications* **92**, 437 (1994).
- [189] M. A. Cusack, P. R. Briddon, M. Jaros, “Electronic structure of InAs/GaAs self-assembled quantum dots”, *Phys. Rev. B* **54**, 2300 (1996).

- [190] M. A. Cusack, P. R. Briddon, M. Jaros, “Absorption spectra and optical transitions in InAs/GaAs self-assembled quantum dots”, *Phys. Rev. B* **56**, 4047 (1997).
- [191] X. Xu, *Coherent optical spectroscopy of a single semiconductor quantum dot*, Ph.D. thesis, The University of Michigan, The Harrison M. Randall Laboratory of Physics, Ann Arbor MI 48109-1120 (2008).
- [192] S. Raymond, S. Fafard, P. J. Poole, A. Wojs, P. Hawrylak, S. Charbonneau, “State filling and time-resolved photoluminescence of excited states in $\text{In}_x\text{Ga}_{1-x}\text{As}/\text{GaAs}$ self-assembled quantum dots”, *Phys. Rev. B* **54**, 11548 (1996).
- [193] D. Gammon, E. S. Snow, B. V. Shanabrook, D. S. Katzer, D. Park, “Fine Structure Splitting in the Optical Spectra of Single GaAs Quantum Dots”, *Phys. Rev. Lett.* **76**, 3005 (1996).
- [194] J. R. Guest, T. H. Stievater, X. Li, J. Cheng, D. G. Steel, D. Gammon, D. S. Katzer, D. Park, C. Ell, A. Thränhardt, G. Khitrova, H. M. Gibbs, “Measurement of optical absorption by a single quantum dot exciton”, *Phys. Rev. Lett.* **65**, 241310 (2002).
- [195] A. Zrenner, E. Beham, S. Stuffer, F. Findeis, M. Bichler, G. Abstreiter, “Coherent properties of a two-level system based on a quantum-dot photodiode”, *Nature* **418**, 612 (2002).
- [196] A. J. Ramsay, S. J. Boyle, R. S. Kolodka, J. B. B. Oliveira, J. Skiba-Szymanska, H. Y. Liu, M. Hopkinson, A. M. Fox, M. S. Skolnick, “Fast Optical Preparation, Control and Readout of a Single Quantum Dot Spin”, *Phys. Rev. Lett.* **100**, 197401 (2008).
- [197] M. O. Scully, M. S. Zubairy, *Quantum Optics*, Cambridge University Press, Cambridge, United Kingdom, first edition (1997).
- [198] E. E. Vdovin, A. Levin, A. Patane, L. Eaves, P. C. Main, Y. N. Khanin, Y. V. Dubrovskii, M. Henini, G. Hill, “Imaging the Electron Wave Function in Self-Assembled Quantum Dots”, *Science* **290**, 122 (2000).
- [199] P. Borri, W. Langbein, S. Schneider, U. Woggon, R. L. Sellin, D. Ouyang, D. Bimberg, “Ultralong Dephasing Time in InGaAs Quantum Dots”, *Phys. Rev. Lett.* **87**, 157401 (2001).
- [200] J. D. Jackson, *Classical Electrodynamics*, John Wiley & Sons, Inc., Hoboken, third edition (1999).
- [201] P. L. Kelley, “Self-Focusing of Optical Beams”, *Phys. Rev. Lett.* **15**, 1005 (1965).

- [202] M. V. G. Dutt, J. Cheng, B. Li, X. Xu, X. Li, P. R. Berman, D. G. Steel, A. S. Bracker, D. Gammon, S. E. Economou, R.-B. Liu, L. J. Sham, “Stimulated and Spontaneous Optical Generation of Electron Spin Coherence in Charged GaAs Quantum Dots”, *Phys. Rev. Lett.* **94**, 227403 (2005).
- [203] M. V. G. Dutt, J. Cheng, Y. Wu, X. Xu, D. G. Steel, A. S. Bracker, D. Gammon, S. E. Economou, R.-B. Liu, L. J. Sham, “Ultrafast optical control of electron spin coherence in charged GaAs quantum dots”, *Phys. Rev. B* **74**, 125306 (2006).
- [204] T. H. Stievater, X. Li, D. G. Steel, D. Gammon, D. S. Katzer, D. Park, C. Piermarocchi, L. J. Sham, “Rabi Oscillations of Excitons in Single Quantum Dots”, *Phys. Rev. Lett.* **87**, 133603 (2001).
- [205] X. Li, Y. Wu, D. Steel, D. Gammon, T. H. Stievater, D. S. Katzer, D. Park, C. Piermarocchi, L. J. Sham, “Raman coherence beats from the entangled state involving polarized excitons in single quantum dots”, *Phys. Rev. B* **70**, 195330 (2004).
- [206] B. Alen, F. Bickel, K. Karrai, R. J. Warburton, P. M. Petroff, “Stark-shift modulation absorption spectroscopy of single quantum dots”, *Appl. Phys. Lett.* **83**, 2235 (2003).
- [207] K. Karrai, R. J. Warburton, “Optical transmission and reflection spectroscopy of single quantum dots”, *Superlattices and Microstructures* **33**, 311 (2003).
- [208] A. N. Vamivakas, M. Atatüre, J. Dreiser, S. T. Yilmaz, A. Badolato, A. K. Swan, B. B. Goldberg, A. Imamoglu, M. S. Unlu, “Strong Extinction of a Far-Field Laser Beam by a Single Quantum Dot”, *Nano Letters* **7**, 2892 (2007).
- [209] D. P. DiVincenzo, “Two-bit gates are universal for quantum computation”, *Phys. Rev. A* **51**, 1015 (1996).
- [210] C. Emary, L. J. Sham, “Optically controlled single-qubit rotations in self-assembled InAs quantum dots”, *J. Phys.: Condens. Matter* **19**, 056203 (2007).
- [211] P. R. Berman, *Lecture Notes for Physics 542: Quantum Optics*, University of Michigan (March, 2007).
- [212] Y. Aharonov, J. Anandan, “Phase Change during a Cyclic Quantum Evolution”, *Phys. Rev. Lett.* **58**, 1593 (1987).
- [213] D. Kim, S. E. Economou, S. C. Badescu, M. Scheibner, A. S. Bracker, M. Bashkansky, T. L. Reinecke, D. Gammon, “Optical Spin Initialization and Nondestructive Measurement in a Quantum Dot Molecule”, *Phys. Rev. Lett.* **101**, 236804 (2008).
- [214] J. M. Villas-Boas, S. E. Ulloa, A. O. Govorov, “Decoherence of Rabi Oscillations in a Single Quantum Dot”, *Phys. Rev. Lett.* **94**, 057404 (2005).

- [215] J. V. Barth, G. Costantini, K. Kern, “Engineering atomic and molecular nanostructures at surfaces”, *Nature* **437**, 671 (2005).
- [216] R. Songmuang, S. Kiravittaya, O. G. Schmidt, “Formation of lateral quantum dot molecules around self-assembled nanoholes”, *Appl. Phys. Lett.* **82**, 2892 (2003).
- [217] Q. Xie, A. Madhukar, P. Chen, N. P. Kobayshi, “Vertically self-organized InAs quantum box islands on GaAs (100)”, *Phys. Rev. Lett.* **75**, 2542 (1995).
- [218] Y. Akahane, T. Asano, B.-S. Song, S. Noda, “High-Q photonic nanocavity in a two-dimensional photonic crystal”, *Nature* **425**, 944 (2003).
- [219] D. K. Armani, T. J. Kippenberg, S. M. Spillane, K. J. Vahala, “Ultra-high-Q toroid microcavity on a chip”, *Nature* **421**, 925 (2003).
- [220] A. Bambini, P. R. Berman, “Analytic solutions to the two-state problem for a class of coupling potentials”, *Phys. Rev. A* **23**, 2496 (1981).
- [221] G. B. Arfken, H. J. Weber, *Mathematical Methods for Physicists*, Academic Press, San Diego, fifth edition (2001).
- [222] A. de Shalit, I. Talmi, *Nuclear Shell Theory*, Academic Press Inc., New York, first edition (1963).